# Liquid-TiO2 Interfaces: Imaging with Frequency-Modulation Atomic Force Microscopy

Xue, Shengkai

(Degree)
博士（理学）

(Date of Degree)
2020-03-25

(Date of Publication)
2021-03-01

(Resource Type)
doctoral thesis

(Report Number)
甲第7707号

(URL)
https://hdl.handle.net/20.500.14094/D1007707

Doctoral Dissertation

# Liquid-$TiO_2$ Interfaces: Imaging with Frequency-Modulation Atomic Force Microscopy
# (周波数変調原子間力顕微鏡(FM-AFM)を用いた酸化チタン表面の液中観察)

January 2020

Graduate School of Science, Kobe University

XUE SHENGKAI

# Table of contents

# Chapter 1

# General Introduction

## 1.1 BACK GROUND

### 1.1.1 Liquid-solid interface

The solids, solutions and gases around us are in contact with each other. The Different phases meets together is the ‘interface’. The solid surface contacted with liquid, where there is a liquid-solid interface.

The liquid-solid interface is a particularly important place of chemical reaction. For example, catalytic reaction in liquid is reaction on the solid surface. Controlling the interface of liquid-solid can control the progress of the reaction. Corrosion is also a solid-liquid interface reaction [1]. Corrosion can be prevented by reducing this reaction rate. Hydrophilic and hydrophobic treatment of the surface is also a study of liquid-solid interface. This is a hot topic in materials science. Furthermore, biological cell membranes are solid-liquid interfaces that serve as entrances and exits for the exchange of substances and energy between the inside and outside of cells [2].

Liquid and solids consist of atoms or molecules. To understand and control the reactions at the liquid-solid interface, the atomic knowledge of the liquid-solid interface is necessary. Titanium oxide ($TiO_2$) surface is a topic that lots of people has paid attention to it in the past 40 years. Water-$TiO_2$ interface also has been concerned. However, the research of water-$TiO_2$ interface with atomic level is scarce. In this paper, the author focused on the water-$TiO_2$ interface with frequency-modulation atomic force microscopy. That is a new method which is enables to directly observe the solid-liquid interface at atomic level.

## 1.1.2 Titanium oxide

Titanium oxide has the wide range of application in our daily life. Titanium oxide is used in catalyst, white pigment, gas sensor, optical coating, electric devices and so on. The catalyst is one main driving force for surface investigations on $TiO_2$. In the field of traditional catalysts, many growth studies of metals on $TiO_2$ were presented [3-4]. Au-$TiO_2$ catalysts can oxidize CO at low temperature [3]. AuPd-$TiO_2$ catalysts has been used in amination of 1-hexanol [4]. There experiments can be analyzed as individual cases or as a model for the metal-oxide surface. It is a good way to have better understanding and improvement of catalytic reactions.

In the past years, $TiO_2$ research is focused on the photoelectric and photochemical properties. Fujishima and Honda [5] found $TiO_2$ could decompose water into $H_2$ and $O_2$ by light irradiation. Unfortunately, after 40 years of development, the quantum efficiency within visible light of $TiO_2$ is still not very high and not practical [6]. However, $TiO_2$ absorbed with dye molecules was good way to improve efficiency of solar cells [7]. It is another way for $TiO_2$ applications.

The most widespread application in photochemical properties is decomposition of organic molecules. This has been widely used in our daily life such as wall coating with self-cleaning function, purification of wastewater [9]. The mechanism is that $TiO_2$ is semiconductor. When it irradiates with light, the electron-hole pair can separate and substance charge carriers on the surface. Those charge carriers can react with water and oxygen which is absorbed on the $TiO_2$ surface, resulting radical species be produced. The radical species decompose organic molecules on the $TiO_2$ surface into $CO_2$ and $H_2O$.

$TiO_2$ has been widely used in white pigments since $20^{th}$ century. Because it is safe and non-toxic, $TiO_2$ replaced traditional white lead as white pigments. In addition to this, $TiO_2$ also used in cosmetic products and pharmaceuticals [9].

Semiconducting metal oxides can change their conductivity when the gas absorbed on the surface. Due to this characteristic, $TiO_2$ is also used for gas sensors. Ruiz et al. [10] presented a Cr-doped $TiO_2$ which is a p-type semiconductor to detect $NO_2$ gas in air. Karunagaran et al. [11] prepared a low thickness $TiO_2$ film by DC magnetron sputtering to sense ammonia.

### 1.1.3 Bulk structure of titanium oxide

$TiO_2$ crystal has three major different structures: rutile, anatase, brookite. Rutile is the stalest structure of $TiO_2$ crystal. The unit cell of Rutile shows in Figure 1. In this structure, one titanium atom combined with six oxygen atoms. An octahedron structure is generated by oxygen atoms. Two adjacent $TiO_6$ octahedra along the c-axis share a ridge and connect in chain. A model of anatase is shown in Figure 2. It is also one titanium atom combined with six oxygen atoms. $TiO_6$ octahedra are mutually connected by two pairs of opposite edges. Octahedrons surround each of the four spiral axes to form a spiral chain parallel to the c-axis. Brookite is orthorhombic system different from the rutile and anatase which are tetragonal crystal system. A model of brookite shows in Figure 3. Each $TiO_6$ octahedron has three corners and shares with the surround three $TiO_6$ octahedrons. Ti atom slightly deviates from the center of the octahedron forming a distorted octahedron.

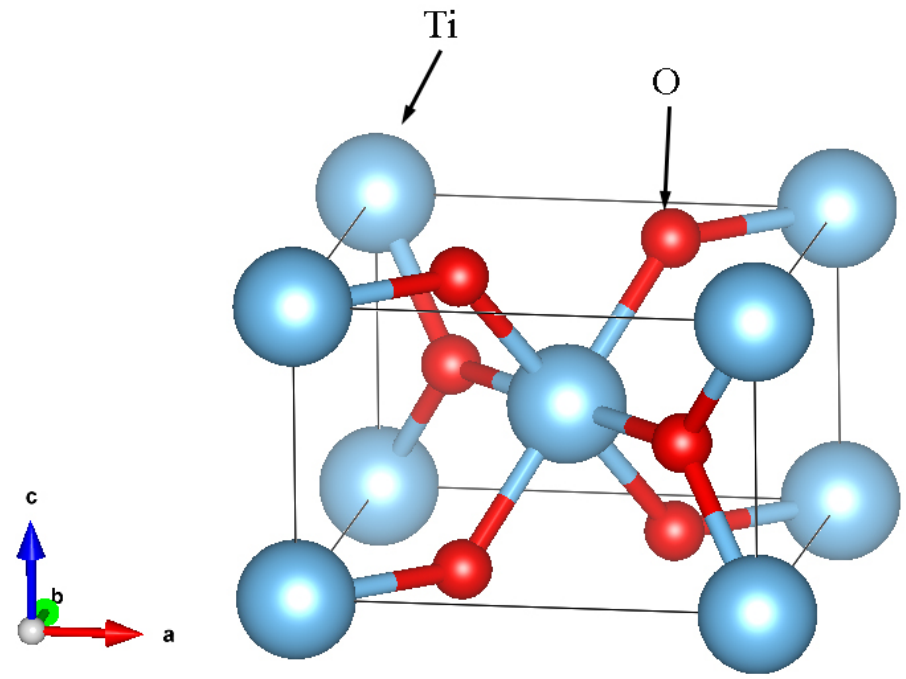


Fig. 1. The model of Rutile.

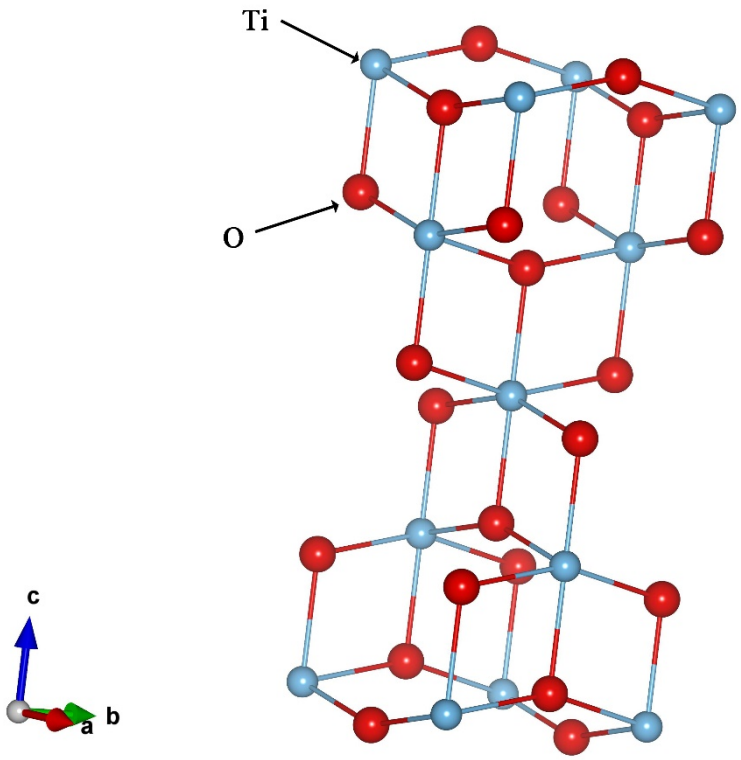


Fig 2. The model of anatase.

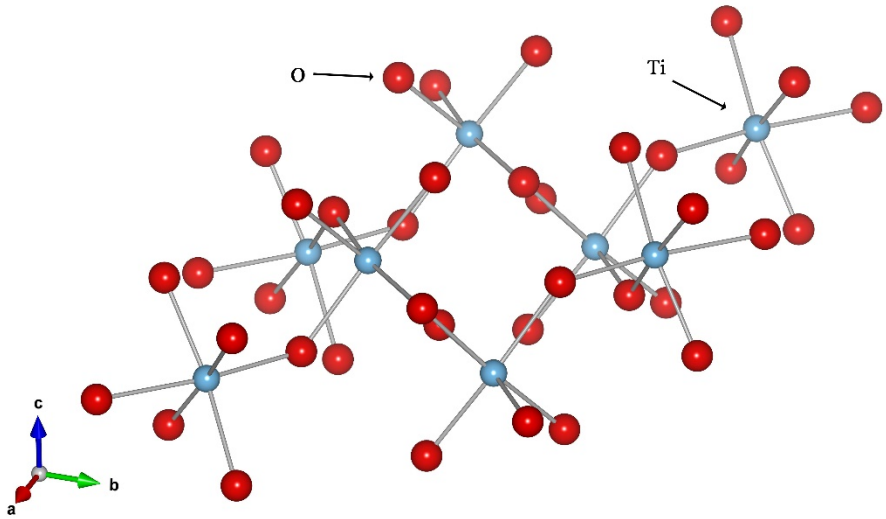


Fig. 3. The model of brookite.

Ramamoorthy et al. [12] calculated the total energy of $TiO_2$ by using a self-consistent ab initio method. The results showed (110) surface has the lowest surface energy. They also constructed a 3D Wulff plot from the result of calculation (Figure4.)

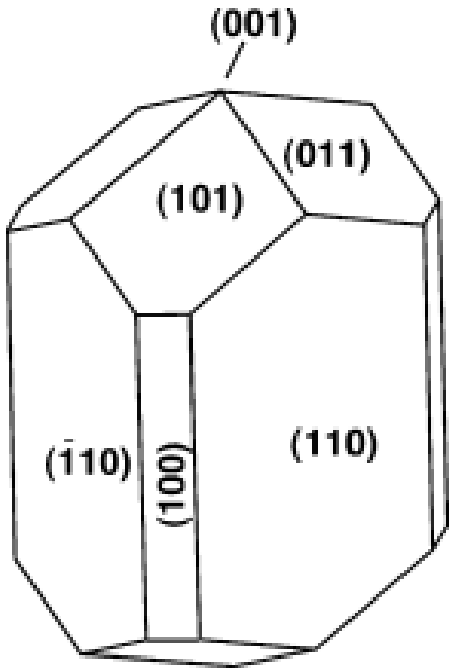


Fig. 4. The wulff plot of $TiO_2$ crystal [12].

## 1.1.4 Rutile (110) surface

The (110) surface is the most stable surface in rutile crystal. Research on this is also helpful for other oxide materials. Lots of research focus on this surface as an example of oxide material surface.

The model of rutile (110) surface is shown in Figure 5. On the surface, five-fold coordinated and six-fold coordinated $Ti^{4+}$ cations are located on a surface plane perpendicular to the [110] direction together with three-fold coordinated $O^{2-}$ anions. Two-fold coordinated oxygen anions located at the position above the surface by bridging two six-fold coordinated Ti cations. On the rutile (110) surface, there are two type of Ti cations and O anions. The two-fold coordinated O anions just bound with two Ti cations, that miss one bond the Ti cation. Because the bridging oxygen is coordinative undersaturation, these bridging oxygens could be removed easily by annealing [13]. The five-fold coordinated Ti cations can combine with some molecules because of their coordinative undersaturation [14-15].

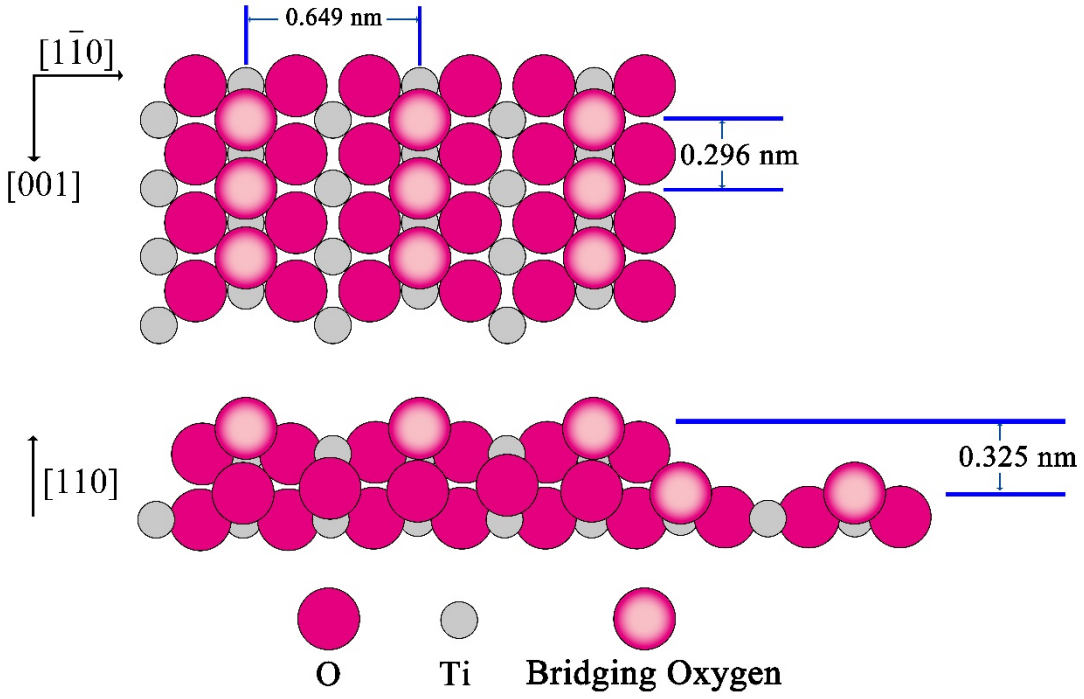


Fig. 5. A model of rutile (110) surface.

### 1.1.4.1 Rutile (110) surface in UHV

Studying atomic-scale structure on $TiO_2$ surface is a extremely useful tools for affecting of surface reactivity. For getting the atomic-scale structure, the scanning probe microscopy is a useful method. In ultra-high vacuum (UHV), scanning tunneling microscope and atomic force microscopy are applicable.

STM bases on the detection of the magnitude of the tunneling current between the probe and the surface. Single-atom-level fluctuations on the surface can be observed by STM. Onishi et al. [16] observed $TiO_2$ (110)-(1×1) surface which was cleaned with cycles of $Ar^+$ sputtering and UHV annealing. They observed bright dots were parallel to the [001] direction (Figure 6). The bright dots were explained as 5-fold coordinated Ti cations. The reason is that image was recorded with a positive bias. Onishi et al. [17] also presented another paper confirmed this point of view. They observed formate ions on the bright rows. These formate ions are expected to adsorbed to five-fold coordinated Ti cations.

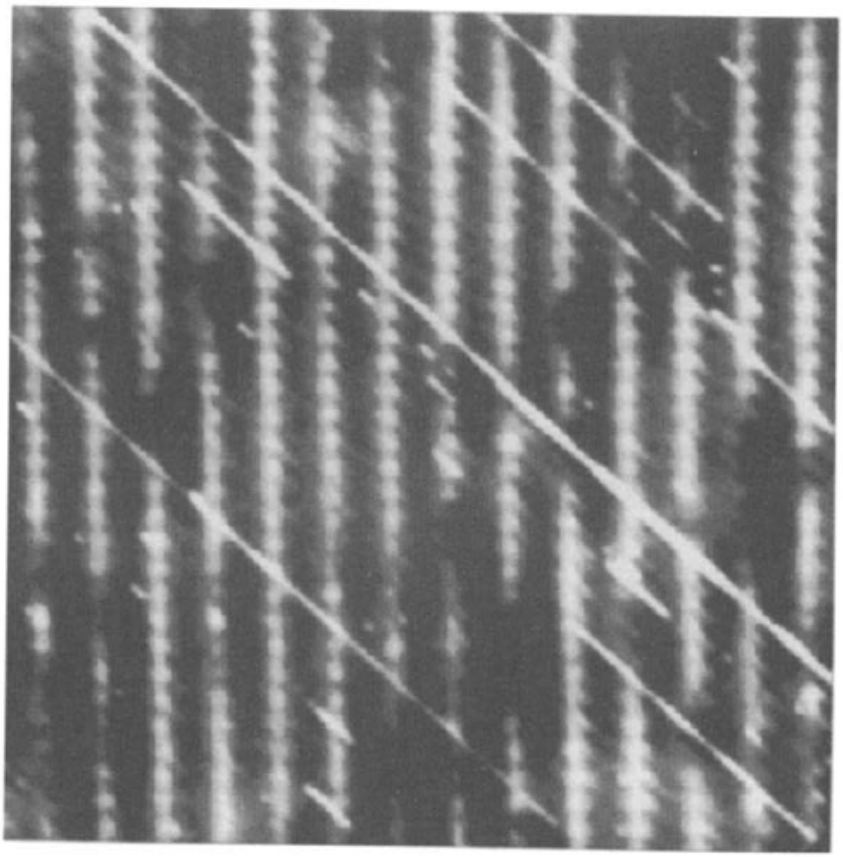

Fig. 6. Topographic image of $TiO_2$(110)-(1×1) surface annealed at 880 K for 30 s. Sample bias : +1.0 nA. Size: 10×10 nm [16].

Figure 7 shows an image of $TiO_2$(110)-(1×1) surface by frequency modulation atomic force microscopy(FM-AFM) obtained by Fukui et al. [18]. The FM-AFM image also showed bright rows paralleled to the [001] direction. FM-AFM detects the atoms by force between the probe and the surface. In AFM images, the main factor that dominates contrast should be physical geometry. These bright rows are consistent with the bridging oxygen on the $TiO_2$(110)-(1×1) surface. These black spots are consistent with oxygen vacancies.

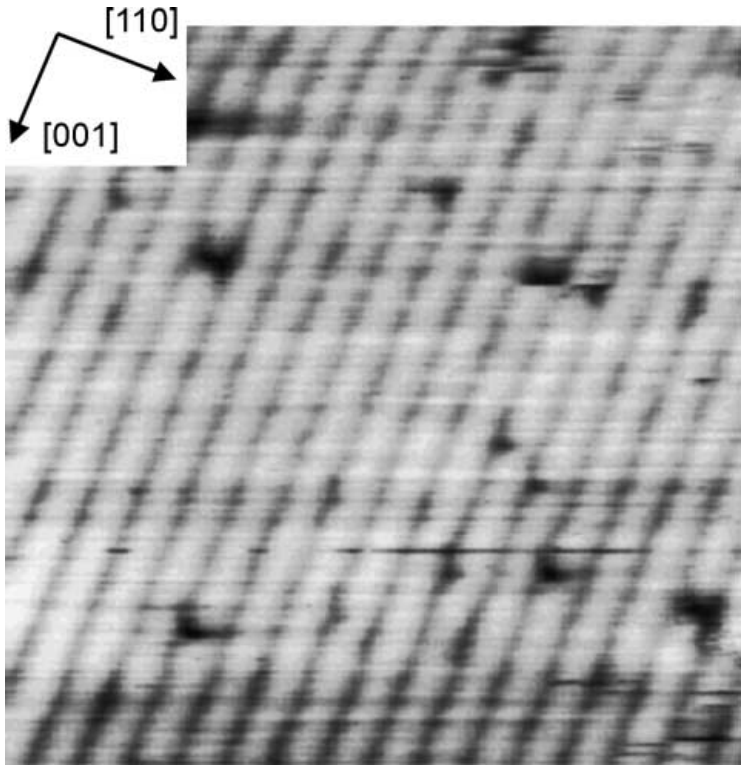


Fig. 7. The FM-AFM image of $TiO_2$(110)-(1×1) surface [18].

### 1.1.4.2 Rutile (110) surface in liquid

Many applications of $TiO_2$ occur in liquids. The most typical application is splitting water by illumination. The rutile (110) structure in liquid became more and more important for studying the reaction on the surface. From 20 years ago, FM-AFM became a new method to studying the surface structure in liquid [19].

Hiasa et al. [20], they are the first to try to parse the rutile (110) surface structure in the liquid. The FM-AFM images shows in Figure 8. They observed the annealed (in air) rutile (110) surface in KCl aqueous solution. An intrinsic step of $TiO_2$(110) could be observed on the middle of image. But on the terrace, no atomic structure could be observed. The bright part on the surface gradually spread over the entire surface within 3 min. They speculated that the substance covering the rutile (110) surface was potassium chloride precipitates.

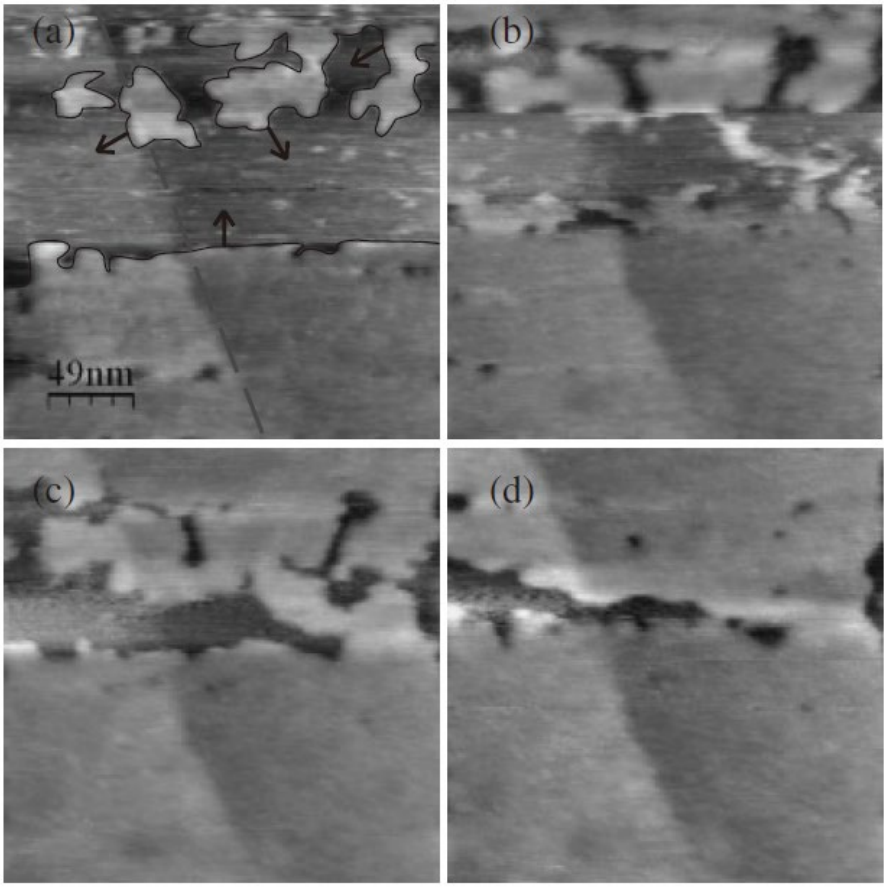


Fig. 8. FM-AFM image of rutile (110) surface in KCl solution. Four images shown in (a) to (d) were observed in intervals of 3 min [20].

In the same year, Sasahara and Tomitori also presented a research about the surface structure of rutile (110) in liquid [21]. They observed a rutile (110) surface which was annealed and sputtered in UHV in pure water by FM-AFM. The FM-AFM image shows in Figure 9. Strings along the [001] direction can be observed. The sting-to-sting distance was ~2 nm. A part of image, dimmed rows showed a 0.6 nm distance by the white arrows. They explained the stings are the water molecular absorbed on the five-fold coordinated Ti cations and the dimmed rows were bridging oxygen on the rutile (110) surface. However, along the [001] direction, the dimmed rows had no periodicity.

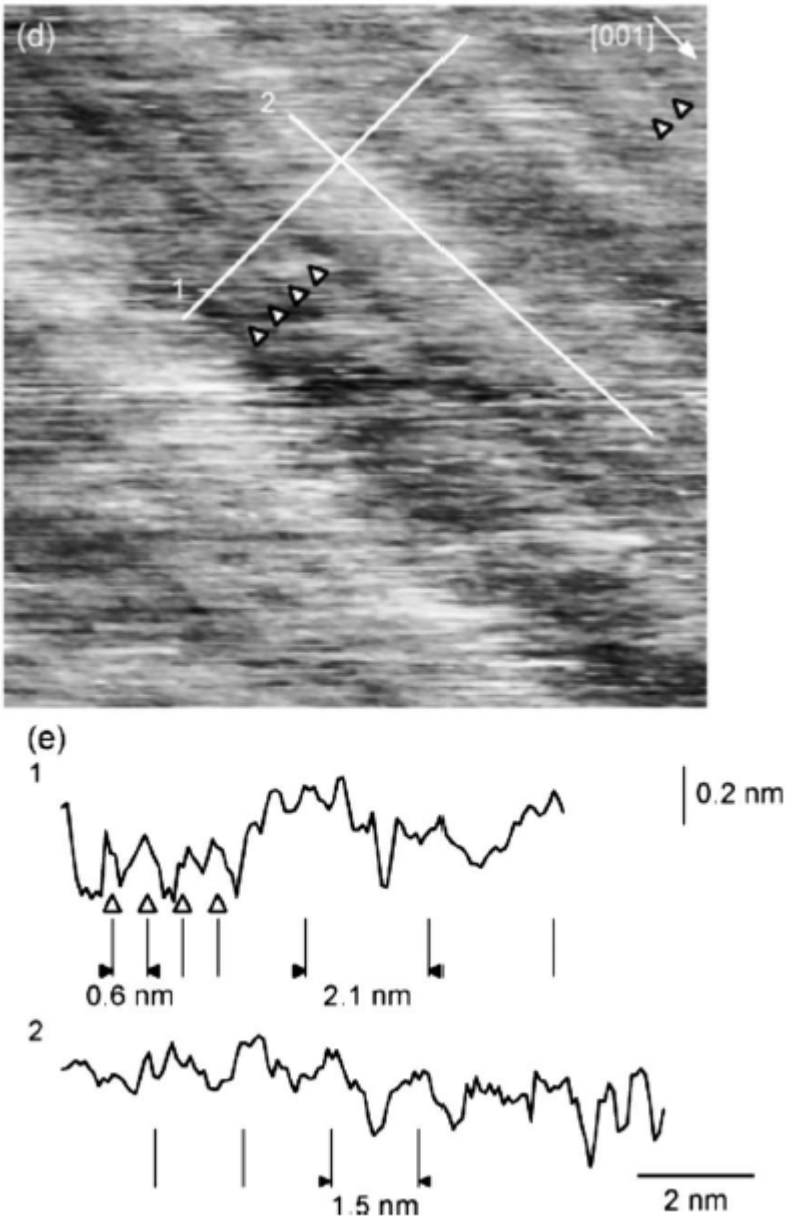


Fig. 9. The FM-AFM image of rutile(110) surface in water [21].

In recent years, the application of STM has expanded from UHV to liquid environment. Serrano et al. [22], they employ STM to observe rutile (110) surface in pure water. The $TiO_2$ crystal was sputtered and annealed in UHV, then filled with high-purity water. They observed a (2×1) structure on the (110) surface. Along the $[1\bar{1}0]$ direction, the distance between two bright rows is 0.7 nm that matches the ×1 periodicity. Along the [001] direction, the distance between two bright rows is 0.6 nm that matches the ×2 periodicity. They explained the (2 × 1) structure is hydrogen-bonded water dimers trapped on the five-fold coordinated Ti cations at the bottom of the trenches by molecular dynamics simulations.

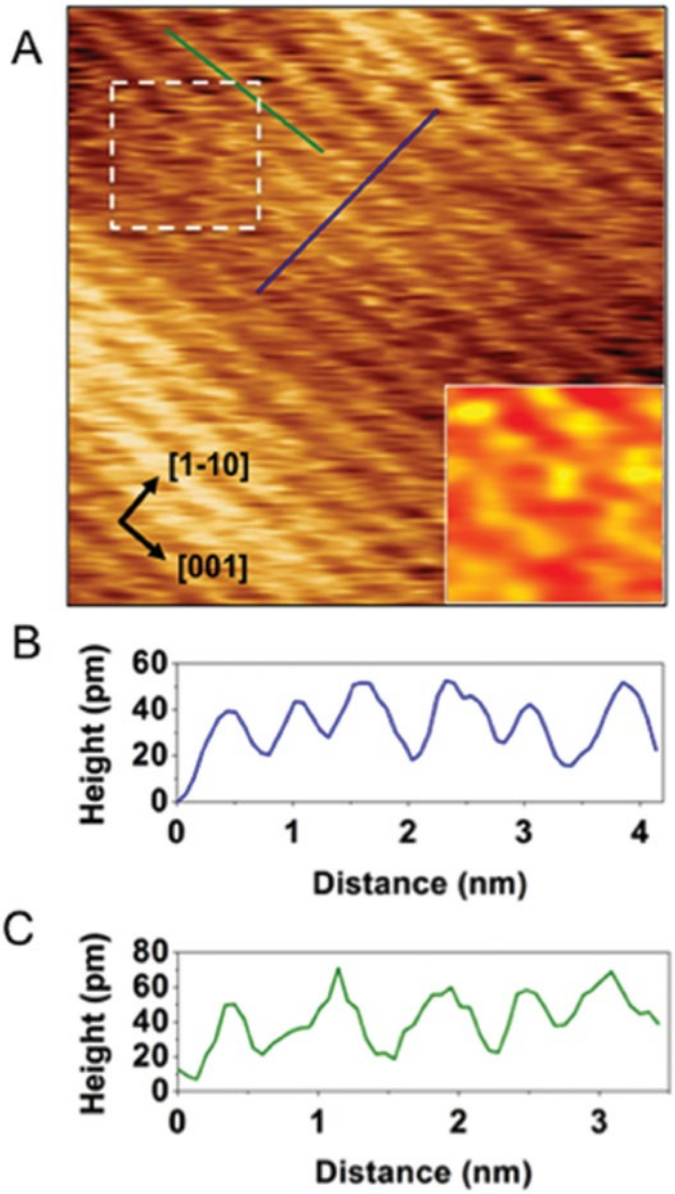


Fig. 10. STM image of rutile (110) surface in pure water [22].

## 1.1.5 Liquid-$TiO_2$ interface

The SPM articles introduced earlier are all focused on the $TiO_2$ side of liquid-$TiO_2$ interface. The liquid side of liquid-$TiO_2$ interface was not observed directly by SPM. The X-ray crystal diffraction (SXRD) and sum-frequency-generation (SFG) spectroscopy are two common methods for researching on the liquid side of liquid-$TiO_2$ interface [23-25].

Zhang et al. [23], measured the rutile (110)-aqueous solution interface structure in deionized water and 1mol $Rb^+$ at pH12 by the X-ray crystal truncation rod method. The results (Figure 11) showed a mixture of water molecules and hydroxyl groups occupying the five-fold coordinated Ti cations in deionized water. Above the mixture layer, an additional hydration layer could be observed. At pH12, only hydroxyl groups occupied the five-fold coordinated Ti cations. Between the hydroxyl groups and bridging oxygen, $Rb^+$ specifically adsorbed at it. No $Rb^+$ part also an additional hydration layer can be observed.

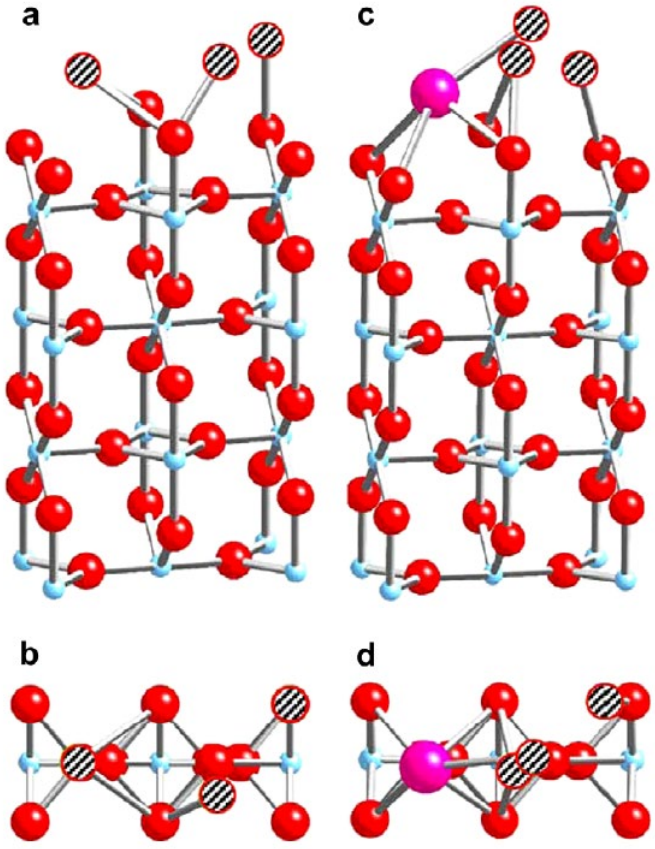


Fig. 11. A ball-and stick model of the Rutile(110)-aqueous solution interfaces. (a) perspective and (b) top view of the interface in deionized water. (c) perspective and (d)

top view of the interface in RbCl solution. Cyan, red, pink, hatched circles represent Ti, O, $Rb^+$, and $H_2O$ [23].

Kataoka et al. [24] presented the water structure at the aqueous-$TiO_2$ interface from pH 2 to 12 by SFG. At isoelectric point (pH = 5.5), the intensity of SFG showed the lowest value. That means the least degree of water organization near the isoelectric. pH was adjusted by NaOH or HCl. At acid or alkaline, intensity of SFG determined by the magnitude of the electric field emanating from the solution-$TiO_2$ interface.

But Schelgel et al. [25] pointed out the intensity of SFG was affected by the water from $TiO_2$. They excluded this effect by using $D_2O$ instead of $H_2O$. The results stand in contrast to the previous research presented by Kataoka et al. [24]. They also presented the lowest intensity of SFG near the isoelectric point. However, at pD2 and pD11, formed with a different angle of incidence of the visible beam, the spectral shape changes dramatically. Protons in water molecules reverse direction with isoelectric point as the dividing point. The results show in Figure 12.

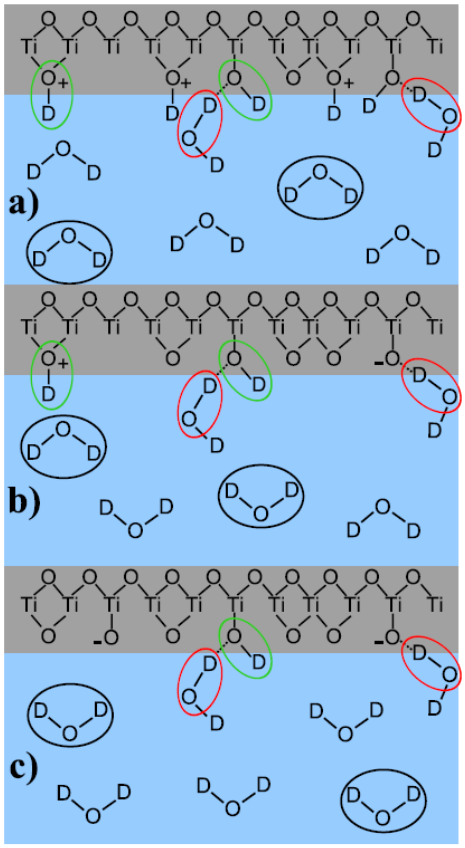


Fig. 12. Water orientation in dependence of pD, for the acidic(a), the neutral(b), and the basic(c) case [25].

## 1.2 CONTRIBUTIONS OF THE AUTHOR

The liquid-$TiO_2$ interface is good model for researching on liquid-solid interface. In this paper, author focused on the liquid-$TiO_2$ interface. In previous research, almost of them focused on one side of liquid-$TiO_2$ interface: the liquid side or $TiO_2$ side. The author employed FM-AFM to observe the $TiO_2$ crystal in liquid for achieving simultaneous observation of the liquid side and $TiO_2$ side.

In chapter 2, the $TiO_2$(110) surface was observed in aqueous solution at different pH value by FM-AFM. At the different pH value, the surface structure changed because $H^+$ and $OH^-$ absorbed on the surface. The water structure at the liquid-$TiO_2$ interface was changed at different pH value since interaction with surface structure.

In chapter 3, Nb 1% doped $TiO_2$(110) surface was observed in aqueous solution and air by AFM. Elemental doping is common method for improving the activity of photocatalyst. To understand the impact of doping, the author focused on the surface structure and liquid structure at the liquid-doped $TiO_2$ interface.

In chapter 4, 1-hexanol-$TiO_2$ interface was observed by FM-AFM. Applications of $TiO_2$ is not only in water, but also in organic solvents. The structure of 1-hexanol on the $TiO_2$(110) surface could help us to understand the reaction in the organic solvents.

In chapter 5, the $TiO_2$(110) surface with Ru complexs was observed in aqueous solution by FM-AFM. Ru complexs could improve its activity by combined with $TiO_2$. The distribution of Ru complexs on the $TiO_2$ surface is important for understanding the reaction on the $TiO_2$ surface with Ru complexs.

## 1.3 METHOD

### 1.3.1 FM-AFM

In 1981, H. Rohrer and G. Binning invented scanning tunneling microscope (STM) and observed the atomic resolution Si surface by STM [26]. STM had received a lot of attention as an epoch-making device which can observe atomic-level surface. However, STM observes the surface shape of the sample by the tunneling current between the probe and the surface of the sample. The sample that STM can observed must has conductivity.

In 1986, C. F. Quate, G. Binning and Ch. Gerber designed atomic force microscope (AFM) based on STM [27]. AFM observes the sample by the force between the probe and the sample surface, thereby overcoming the problem that the sample which can be observed by STM must have the conductivity. AFM can observe insulators for better versatility.

#### 1.3.1.1 Atomic force detection

When two non-ionized atoms are opposed to each other, a force acts between two atoms depending on the interatomic distance. (Figure 13). When the distance between the two atoms is long, an attractive force such as can der Waals force, electrostatic force, magnetic force would act. When the two atoms are sufficiently close to form a chemical bond between them, chemical bonding force is generated. As the two atoms come closer, a steep repulsive Pauli force would act. The cantilever forms a small bend because the interaction between the probe and the sample. By detect this bend, the force between the probe and the sample is detected (Figure 14).

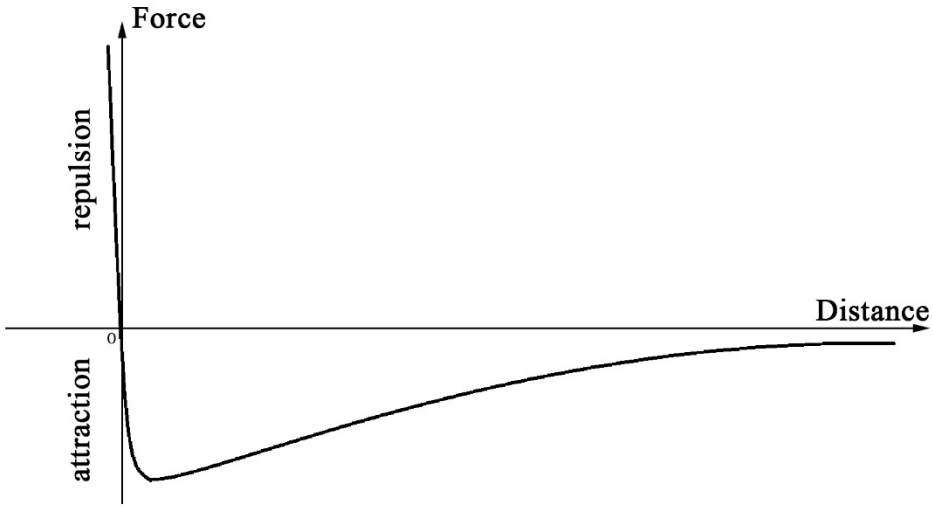


Fig 13. The force between the probe and the sample surface.

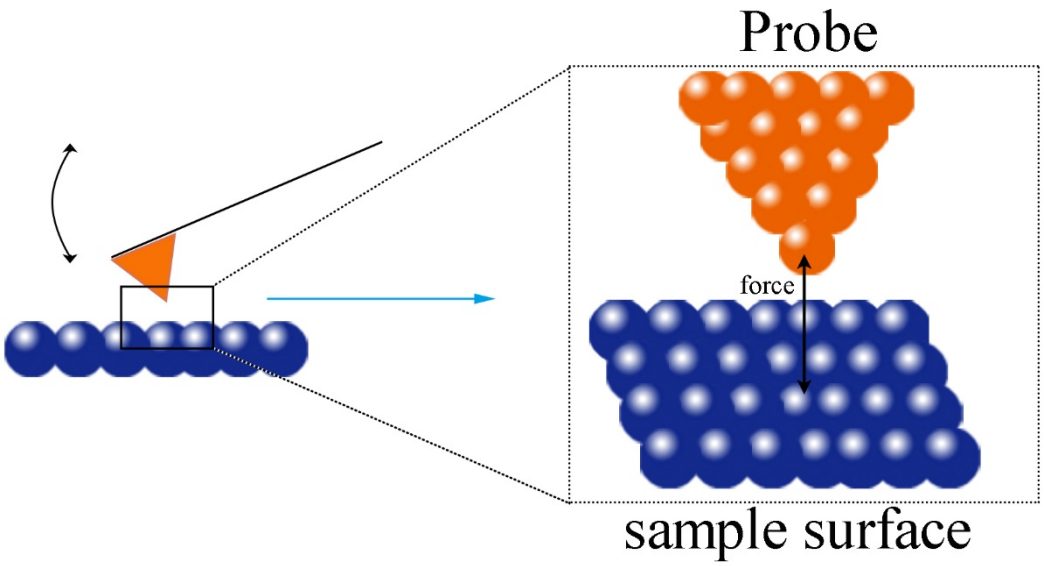


Fig. 14. Bending of the cantilever by force.

#### 1.3.1.2 The mode of AFM

The measurement modes of the AFM are classified in to contact mode and dynamic mode according to method of detecting the force between the probe and sample.

##### 1.3.1.2.1 Contact Mode

The contact mode is the simplest mode that scanning is performed by the probe and the sample contact with each other. The probe receives a repulsive force form the sample surface. The bend of cantilever is detected by the reflection of the laser beam when receiving the repulsion. The sample surface is scanned by cantilever which is keeping the repulsion constant by a feedback circuit. That determines the shape of surface. The cantilever has the smaller spring constant, the bend is bigger with the same repulsive force between the probe and the sample surface. The sensitivity of AFM can be higher.

However, even if an atomic size image is observed by the contact mode, it is not a true atomic resolution image but only a periodic structure of the atomic size. The reason is that a plurality of atoms at the top of cantilever and a plurality of atoms on the surface interact with each other, making it impossible to detect force between single atoms. An image reflecting such a periodic structure is called a lattice image.

In the contact mode, the repulsive force acting between the probe and the sample surface is large. It may damage the sample surface. In particular, it must be careful to use this mode on a soft sample such as sell.

### 1.3.1.2.2 Dynamic Mode

In order to improve the shortcomings of the contact mode, the development of the dynamic mode is in progress. In the dynamic mode, the cantilever is vibrated near the natural frequency. The force applied to the probe is measured using the fact that the amplitude or frequency changes due to the force acting between the probe and the sample surface. In the dynamic mode, the contact time between the probe and the sample surface can be greatly reduced. The force applied to the sample surface can be reduced, so that the damage applied to the sample surface can be reduced. This makes dynamic mode more suitable for soft or fragile samples.

There are two typical modes in dynamic mode. One is Amplitude Modulation (AM) mode and the other one is Frequency Modulation (FM) mode. Figure 15 shows the model of two detection methods in dynamic mode. In AM mode, the cantilever vibrates at a constant frequency ($f_1$). The resonance frequency ($f_0$) of cantilever decreases due to the force between the probe and the sample surface. To detect an amount whose amplitude changes ($\Delta A$) due to the decrease in resonance frequency can reflect magnitude of the force between probe and the sample surface. In FM mode, a change from the resonance frequency ($f_0$) to $f_0'$ is directly detected.

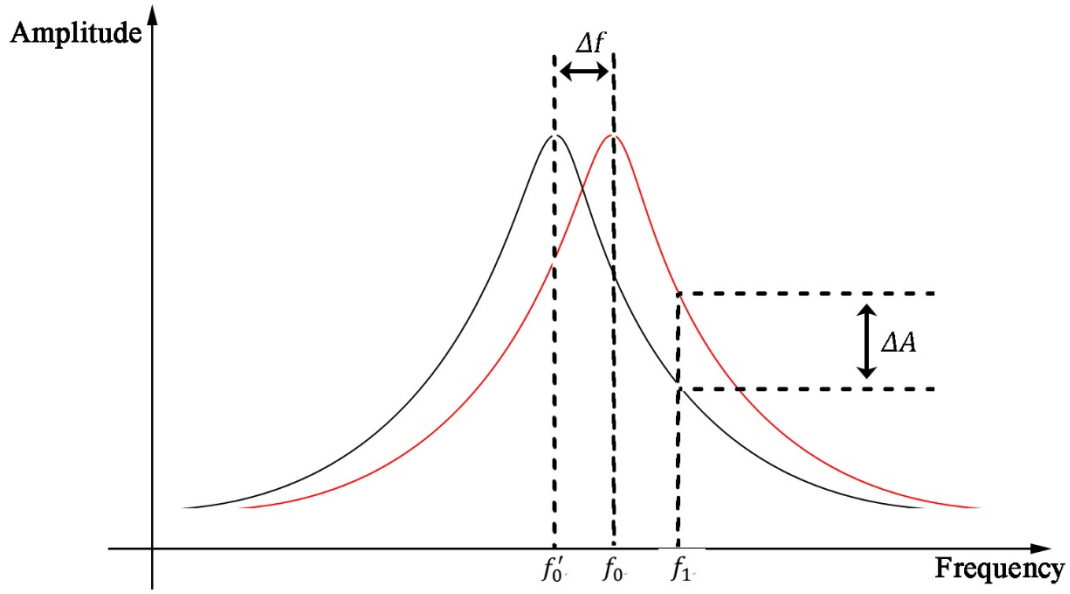


Fig. 15. Schematic diagram of dynamic mode detection.

### 1.3.1.2 Principles of FM-AFM

In this study, the author mainly employed the FM mode. Figure 16 shows a schematic diagram of the device configuration. In FM mode, the cantilever is oscillated at a resonance frequency with a constant amplitude by a positive feedback loop from amplitude control circuit and phase circuit. When the cantilever comes closer to the sample surface, vibration energy of the cantilever is lost due to a non-conservative force acting between the probe and the sample surface. To compensate for this loss, an automatic gain control (AGC) is used. By switching ON/OFF of this function, it is possible to switch between amplitude keeping mode and excitation method with constant amplitude signal. The reflected light position of the laser beam emitted from the laser diode (LD) to the back of cantilever is detected by a four-division photodiode (PD), the deflection of the cantilever is detected. The frequency shift is detected by using a phase locked loop (PLL) circuit. The detected frequency shift is input to a feedback circuit, the feedback circuit controls the Z piezo of the scanner to keep the frequency shift at a set value. In this way, the shape of the sample surface is scanned while the frequency shift is kept constant.

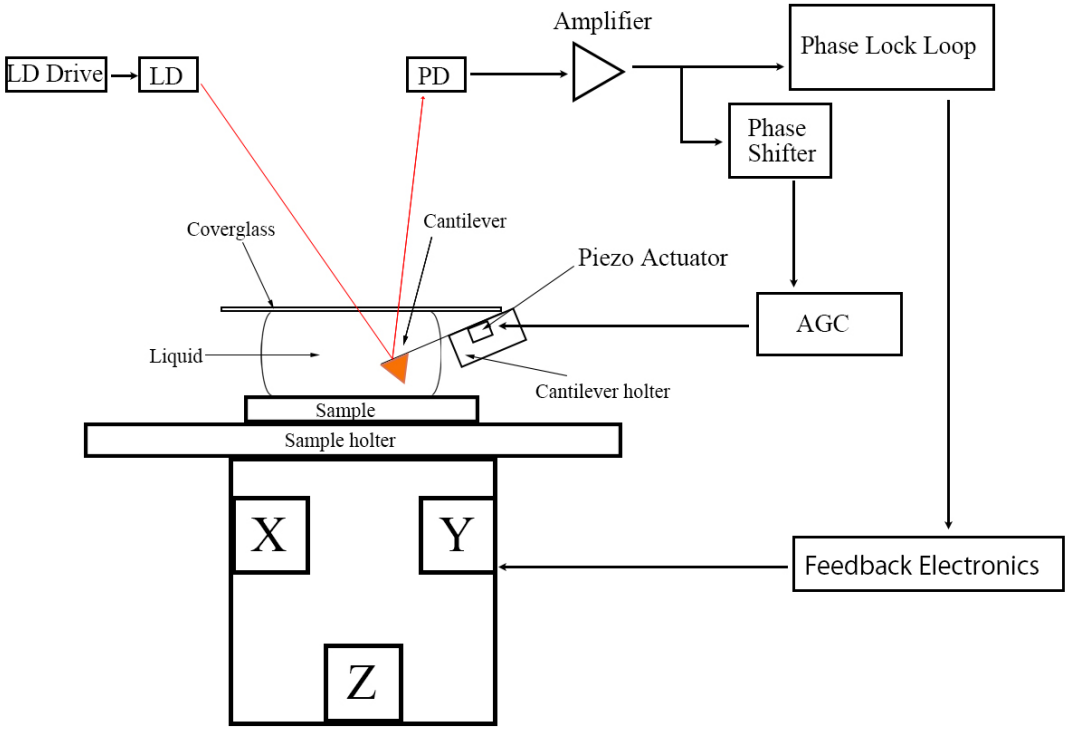


Fig. 16. The model of FM-AFM.

### 1.3.1.3 Relationship between force and frequency shift

The frequency shift of cantilever is proportional to the force gradient. When the cantilever oscillation amplitude is sufficiently small, the frequency shift(*Δf*) is given by [28] in Z range.

$$\Delta f(z) \approx \frac{f_0}{2k}\frac{\partial F_{ts}(z)}{\partial z} \quad (1.1)$$

*k*: the spring constant of cantilever

$F_{ts}$: the force between the probe and the sample surface

$f_0$: resonance frequency

When the cantilever oscillation amplitude is arbitrary, the frequency shift (*Δf*) is given by [29] in Z range.

$$\Delta f(z) \approx \frac{f_0}{2k}\int_{-A}^{A}\frac{\partial F_{ts}(z-z')}{\partial z}\sqrt{A^2 - z'^2}\,dz' \quad (1.2)$$

*A*: the amplitude of cantilever

*z*: vibration center position of cantilever

The obtained frequency shift can be converted to force using following equation (1.3) [30].

$$F_{ts}(z) = 2k\int_{z}^{\infty}\left(1 + \frac{a^{1/2}}{8\sqrt{\pi(h-z)}}\right)\Omega(t) - \frac{a^{3/2}}{\sqrt{2(t-z)}}\frac{d\Omega(t)}{dt}dt \quad (1.3)$$

$\Omega(z) = \Delta f(z)/f_0$

a: an arbitrary oscillation amplitude

#### 1.3.1.4 FM-AFM in liquid

In solution environment, compared to vacuum and air, the quality factory of resonance (Q) is significantly reduced due to the viscous resistance of liquid. This decrease of Q value cases the fluctuation in the cantilever oscillation frequency in FM-AFM and makes it difficult to detect the force acting between the probe and the sample surface.

The noise situation improves when amplitude is increasing. However, the force between the probe and the sample only works when the probe is sufficiently close to the sample. When amplitude is increased, the time which the force acts is reduced. The sensitivity of detecting the force also is deteriorated. Therefore, it is an effective way of detecting a weak force is reducing the amplitude of cantilever, since time which the force acts between the probe and the sample surface is longer. The principle is illustrated in Figure 17. A large amplitude probe vibration is indicated by a blue line, and a small amplitude probe vibration is indicated by a red line. When the probe amplitude is smaller than the distance which the force can act between the probe and the sample surface, the effective interaction time would be the entire period.

In the solution, the surface is often charged due to ionization, dissociation of surface functional groups and adsorption of dissolved ions. In order to neutralize the charge on the surface, ions in the solution gather near the surface to form electric double layer. Similarly, an electric double layer is formed at the interface between the probe and the solution. The force generated between the sample and the probe when two electric double layers approach together. The force between two electric double layers can affect the AFM detecting the weak force between two atoms. Since the thickness of the electric double layer decreases in inverse proportion to the square root of the ion concentration in the solution., 0.1M KCl solution was used in present study to reduce the electric double layer.

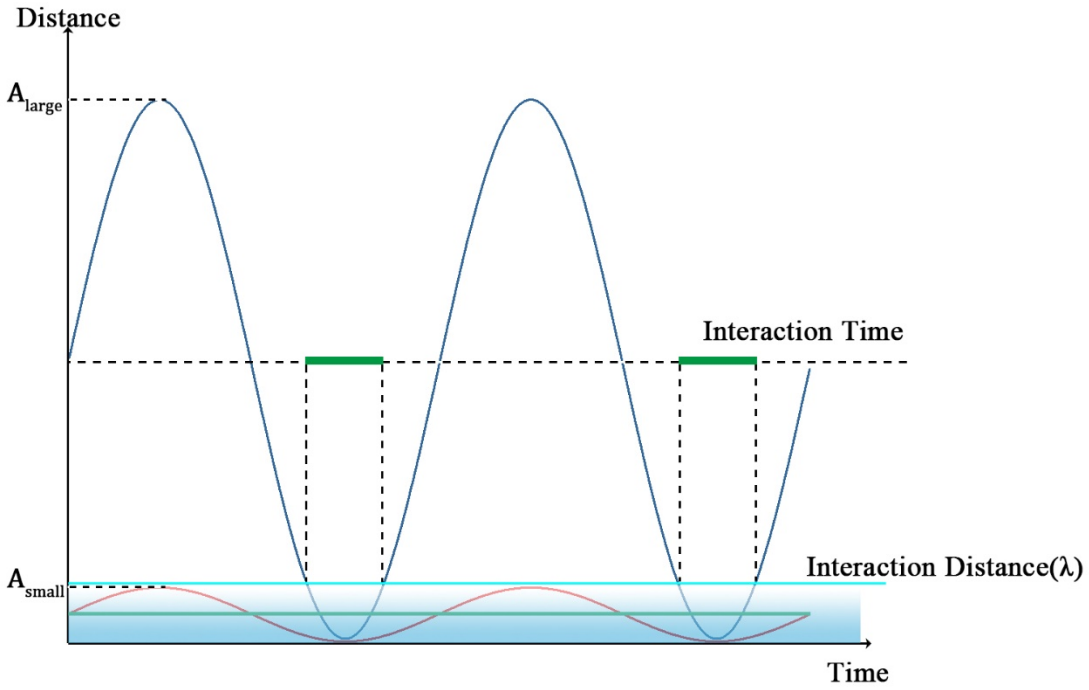


Fig. 17. The time of tip-sample interaction.

### 1.3.2 X-ray photoelectron spectroscopy, XPS

XPS is a surface-sensitive technique that can indicate electronic state, chemical status of elements and elemental composition.

XPS installation diagram is shown in Figure 18. When a sample surface is irradiated with X-ray in UHV, inner-shell electrons absorb energy and photoelectrons are emitted by the photoelectric effect. The kinetic energy of the photoelectron is measured, and the electron binding energy in the atom is calculated using equation (1.4) [31].

$$E_b = hv - E_k - \emptyset \quad (1.4)$$

$E_k$ : kinetic energy
hv: energy of incident X-ray
$E_b$ : electron binding energy
$\emptyset$: work function of spectroscope

XPS indicates the composition of the sample surface based on the photoelectron intensity. The equation (1.5) is used to calculate the composition of the sample surface from intensity of the photoelectron.

$$\frac{N_i}{\sum N_i} = \frac{I_i/S_i}{\sum I_i/S_i} \quad (1.5)$$

Ni: concentration of i atom
Ii : photoelectron intensity of i atom
Si : relative sensitivity factor of i atom

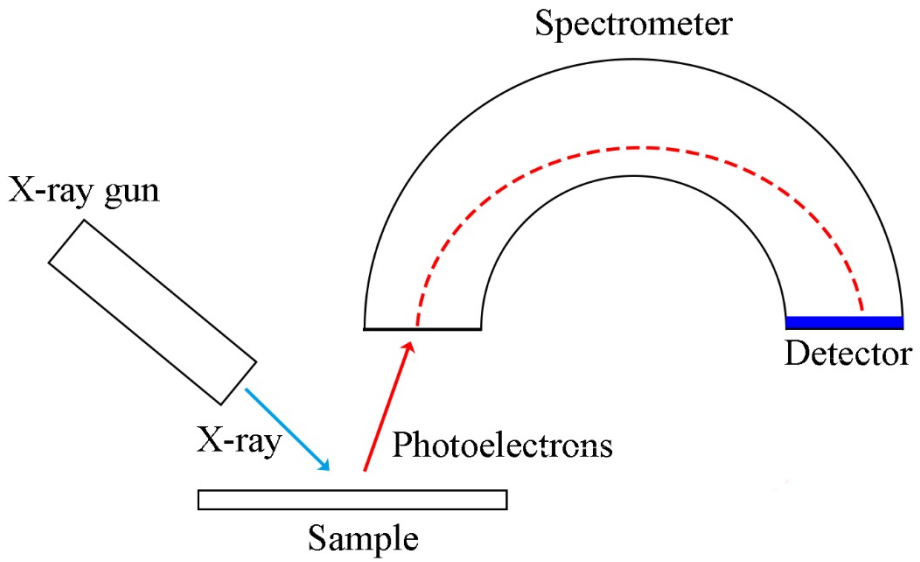


Fig. 18. The model of X-ray photoelectron spectroscopy.

### 1.3.3 Scanning Electron Microscope, SEM

Scanning electron microscope (SEM) is a type of microscope which is widely used in the world. SEM use a focused beam of electron to scan the sample surface for providing an image. The Figure 19 are shown a model of SEM.

In the electron gun, an electron beam is generated from an electron source and accelerated. The accelerated electron beam is focused on the sample as an electron spot. The detector detects the signal electrons generated from the electron beam irradiation point of the sample, and the SEM image shows the amount of the signal electrons as the brightness of each point.

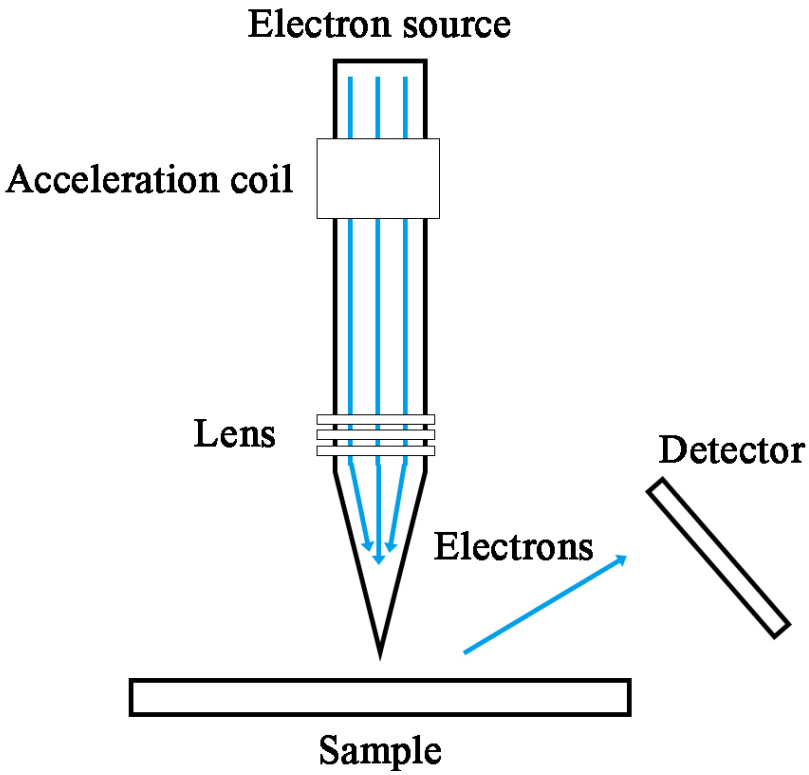


Fig. 19. A model of scanning electron microscope.

## 1.4 REFERENCE


1. Cimatu K, Baldelli S. Chemical Imaging of Corrosion: Sum Frequency Generation Imaging Microscopy of Cyanide on Gold at the Solid− Liquid Interface. *Journal of the American Chemical Society*, 2008, 130, 8030-8037.

2. Tero R, Suda Y, Kato R, Kato R, Tanoue H, Takikawa H. Plasma irradiation of artificial cell membrane system at solid–liquid interface. *Applied Physics Express*, 2014, 7, 077001.

3. Date M, Haruta M. Moisture effect on CO oxidation over Au/$TiO_2$ catalyst. Journal of Catalysis, 2001, 201, 221-224.

4. Ball M R, Wesley T S, Rivera-Dones K R, Huber G W, Dumesic J A. Amination of 1-hexanol on bimetallic AuPd/$TiO_2$ catalysts. *Green Chemistry*, 2018, 20, 4695-4709.

5. Fujishima A, Honda K. Electrochemical photolysis of water at a semiconductor electrode. *Nature*, 1972, 238, 37-38.

6. Ge H, Xu F, Cheng B, Yu J, Ho W. S-scheme heterojunction $TiO_2$/CdS nanocomposite nanofiber as $H_2$-production photocatalyst. *ChemCatChem*, 2019.

7. O'regan B, Grätzel M. A low-cost, high-efficiency solar cell based on dye-sensitized colloidal $TiO_2$ films. *Nature*, 1991, 353, 737.

8. Mills A, Davies R H, Worsley D. Water purification by semiconductor photocatalysis. *Chemical Society Reviews*, 1993, 22, 417-425.

9. Brahmachari G, Das S. A simple and straightforward method for one-pot synthesis of 2, 4, 5-triarylimidazoles using titanium dioxide as an eco-friendly and recyclable catalyst under solvent-free conditions. *NISCAIR-CSIR,*2013, 0376-4699.

10. Ruiz A M, Sakai G, Cornet A, Shimanoe K, Morante J R, Yamazoe N. Cr-doped $TiO_2$ gas sensor for exhaust $NO_2$ monitoring. *Sensors and Actuators B: Chemical*,

2003, 93, 509-518.

11. Karunagaran B, Uthirakumar P, Chung S J, Velumani S, Suh E.-K. $TiO_2$ thin film gas sensor for monitoring ammonia. *Materials Characterization*, 2007, 58, 680-684.

12. Ramamoorthy M, Vanderbilt D, King-Smith R D. First-principles calculations of the energetics of stoichiometric $TiO_2$ surfaces. *Physical Review B*, 1994, 49, 16721.

13. Diebold U, Lehman J, Mahmoud T, Kuhna M, Leonardelli G, Hebenstreit W, Schmid M, Varga P. Intrinsic defects on a $TiO_2$(110) (1× 1) surface and their reaction with oxygen: a scanning tunneling microscopy study. *Surface science*, 1998, 411, 137-153.

14. Chen D A, Bartelt M C, Hwang R Q, McCarty K.F. Self-limiting growth of copper islands on $TiO_2$ (110)-(1× 1). *Surface Science*, 2000, 450: 78-97.

15. Sasahara A, Pang C L, Onishi H. STM observation of a ruthenium dye adsorbed on a $TiO_2$ (110) surface. *The Journal of Physical Chemistry B*, 2006, 110: 4751-4755.

16. Onishi H, Iwasawa Y. Reconstruction of $TiO_2$(110) surface: STM study with atomic-scale resolution. *Surface Science*, 1994, 313, L783-L789.

17. Onishi H, Iwasawa Y. STM-imaging of formate intermediates adsorbed on a $TiO_2$ (110) surface. *Chemical Physics Letters*, 1994, 226, 111-114.

18. Fukui K, Onishi H, Iwasawa Y. Atom-resolved image of the $TiO_2$ (110) surface by noncontact atomic force microscopy, *Physical Review Letters*, 1997, 79, 4202.

19. Fukuma T, Kobayashi K, Matsushige K, Yamada H. True atomic resolution in liquid by frequency-modulation atomic force microscopy. *Applied Physics Letters*, 2005, 87, 034101.

20. Hiasa T, Kimura K, Onishi H, Ohta M, Watanabe K, Kokawa R, Oyabu N, Kobayashi K, Yamada H. Solution–$TiO_2$ interface probed by frequency-modulation atomic force microscopy. *Japanese Journal of Applied Physics*, 2009, 48, 08JB19.

21. Sasahara A, Tomitori M. Frequency modulation atomic force microscope

observation of $TiO_2$ (110) surfaces in water. *Journal of Vacuum Science & Technology B, Nanotechnology and Microelectronics: Materials, Processing, Measurement, and Phenomena*, 2010, 28, C4C5-C4C10.

22. Serrano G, Bonanni B, Di Giovannantonio M, Kosmala T, Schmid M, Diebold U, Carlo A D, Cheng J, VandeVondele J, Wandelt K, Geletti C. Molecular ordering at the interface between liquid water and rutile $TiO_2$(110). *Advanced Materials Interfaces*, 2015, 2, 1500246.
23. Zhang Z, Fenter P, Sturchio N C, Bedzyk M J, Machesky M L, Wesolowski D.J. Structure of rutile $TiO_2$(110) in water and 1 molal Rb+ at pH 12: Inter-relationship among surface charge, interfacial hydration structure, and substrate structural displacements. *Surface Science*, 2007, 601, 1129-1143.
24. Kataoka S, Gurau M C, Albertorio F, Holden M A, Lim S, Yang R D, Cremer P S. Investigation of water structure at the $TiO_2$/aqueous interface. *Langmuir*, 2004, 20, 1662-1666.
25. chlegel S J, Hosseinpour S, Gebhard M, Devi A, Bonn M, Backus E H.G. How water flips at charged titanium dioxide: an SFG-study on the water–$TiO_2$ interface. *Physical Chemistry Chemical Physics*, 2019, 21, 8956-8964.
26. Binnig G, Rohrer H, Gerber C, Weibei E. 7× 7 reconstruction on Si (111) resolved in real space. *Physical Review Letters*, 1983, 50, 120.
27. Binnig G, Gerber C, Stoll E, Albrecht T R, Quate C F. Atomic resolution with atomic force microscope. *Europhysics Letters,* 1987, 3, 1281.
28. Albrecht T R, Grütter P, Horne D, Rugar D. Frequency modulation detection using high-Q cantilevers for enhanced force microscope sensitivity. *Journal of Applied Physics*, 1991, 69, 668-673.
29. Gießibl F J. A direct method to calculate tip–sample forces from frequency shifts in frequency-modulation atomic force microscopy. *Applied Physics Letters*, 2001, 78, 123-125.

30. Sader J E, Jarvis S P. Accurate formulas for interaction force and energy in frequency modulation force spectroscopy. *Applied Physics Letters*, 2004, 84, 1801-1803.

31. Crist B V, Crisst D B V. Handbook of monochromatic XPS spectra. *New York: Wiley*, 2000.

# Chapter 2

# Water–$TiO_2$(110) interfaces at different pH: atom-scale imaging with frequency-modulation atomic force microscopy

## 2.1 INTRODUCTION

Titanium dioxide ($TiO_2$) was widely used in various industrial products including pigments [1], cosmetics [2], gas sensors [3], and photocatalysts [4], and has been studied in details for many years in view of its significant properties. In a previous research, the surface of $TiO_2$(110) provided a great deal of nanoscale information under ultrahigh vacuum (UHV) condition [5]. Since rutile $TiO_2$(110) surface has the lowest energy termination of rutile and shows single height steps and the terraces with noncontracted (1×1) structure, it acts as a model system for understanding the nature of surface reactions at atomic and molecular scale in UHV condition. A model of $TiO_2$(110) – (1×1) surface is shown in Fig.1. The topmost O atoms are bound to two 6-fold Ti atoms along the [001] direction. The 5-fold Ti atoms exposed between bridge O atom rows. Annealed (110) surface consists of atomically flat terraces with a 0.32 nm height step confirmed by STM study in UHV [5].

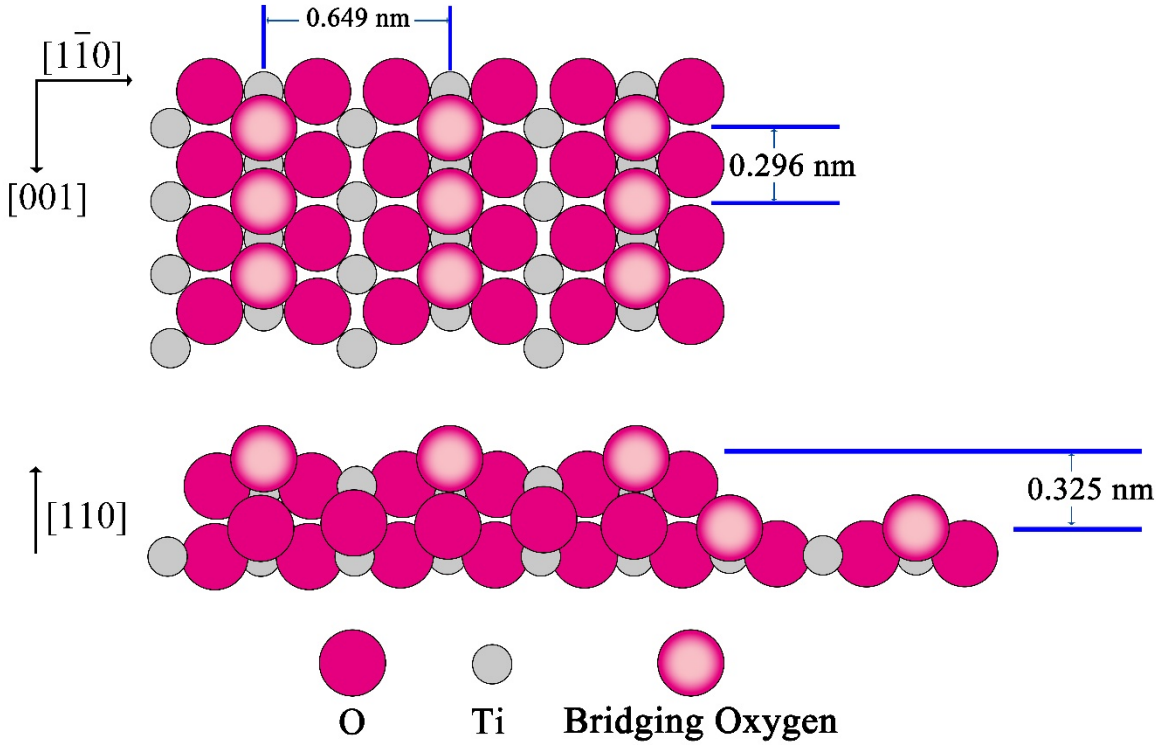


Fig. 1. A model of the $TiO_2$(110) –(1×1) surface.

In most cases, $TiO_2$ shows its actions in aqueous solutions. For example, the chemical reaction of photocatalysts takes place at the solid-liquid interface. Therefore, in-situ analysis in aqueous solutions would further enhance our understanding of the useful properties of $TiO_2$. However, experimental methods to determine the molecular-scale structure of $TiO_2$ were limited at the solid interface. Classic methods such as electron and ion beam cannot be utilized on solid-liquid interface. Other methods like x-ray diffraction (XRD) [6] and sum-frequency generation (SFG) [7] can only obtain the averaged structure, but cannot provide any detailed structural information on surface structure, such as how water molecules combine with Ti or O atoms and how hydration structures on the surface. In particular, SFG results [7] showed a 3200 $cm^{-1}$ peak at $TiO_2$/water interface with a marked increase at pH 2.0, in which the peak comes mostly from water molecules in subsequent layer, and it may show the oxygen end of water molecules points downward. On the other hand, microscopy can enable visualization of the structures on surface and hydration structures. Serrano et al. [8] used STM to investigate the solid-liquid interface of water-$TiO_2$(110) in bulk water. The results showed the 2×1 overlayer on $TiO_2$(110) surface. In addition, Serrano et al. also used DFT-MD simulations to interpret and verify how the water molecules combine with 5-fold Ti on (110) surface with ×2 periodicity along the [001] direction.

Since 2005, frequency modulation atomic force microscope (FM-AFM) can get the atomic resolution image in liquid [9], and it could develop the understanding of reactions on $TiO_2$ surface. At solid-liquid interfaces, atoms constituting the solid surface interact with liquid, leading to uneven distribution of liquid molecules. Water would participate in the reaction of $TiO_2$ surface such as decomposition of water by photocatalytic reaction. FM-AFM employs a cantilever with a tip to detect the force between the tip and the samples or liquid molecules as a shift of the cantilever resonance frequency [10]. The high spatial and force resolutions of FM-AFM enabled the visualization of two-dimensional images of hydration layers at solid-liquid interfaces [11]. In the present study, $TiO_2$(110) surface was observed in water by using FM-AFM. Hiasa et al. reported a study of the $TiO_2$(110) surface which was annealed in air and observed in KCl solution [12]. They observed domains, but not atomic structures on $TiO_2$ surface. Sasahara et al. reported another study of the $TiO_2$(110) surface which was cleaned in UHV by $Ar^+$ sputtering observed in pure water [13]. The sputter-annealed $TiO_2$ (110) surface showed bright rows along the [001] direction aligned with

separation of 0.6 nm. But they could not observe any periodic structure along the $[1\bar{1}0]$ direction.

$TiO_2$ has different performance under different pH [14-15]. Different pH value can affect dye absorption onto $TiO_2$[15]. Photocatalytic activity of $TiO_2$ in water is also pH-dependent, since an increase in activity can be shown with the increasing pH from 4 to 7[15]. The different pH value would affect hydration structure at water-$TiO_2$ interface. In order to study the reaction on $TiO_2$ surface, it would be beneficial to study the interface of water-$TiO_2$ at different pH. In this study, author report high-resolution AFM images of rutile $TiO_2$ (110) surface in liquid. We found that the observed surface structure with a step-terrace morphology maintains a stable structure in liquid. Interestingly, ordered hydration layers are observed by FM-AFM only at pH 6 which is near the isoelectronic point of the $TiO_2$(110) surface.

## 2.2 EXPERIMENT

### 2.2.1 preparation

Mirror-polished, (110)-oriented wafers of rutile $TiO_2$ (Shinkosha, STEP type) were annealed in a two-step procedure using a tube furnace, in accordance with earlier report [16]. Isolating the wafer from $SiO_2$-containing devices heated at 1000 ℃ or higher temperatures was essential to avoid silicon contamination on the annealed surface. The wafers were first maintained at 1000 ℃ for 12 hours in a sapphire tube open to laboratory air. Annealing at the elevated temperature was efficient for developing wide (110) terraces. In the second step, the wafer was further annealed at 500 ℃ in a quartz tube filled with dry air, a mixture of $O_2$ and $N_2$ with a pressure ratio of 1:4. The absence of water vapor in the annealing environment was the key to finish a well-ordered $TiO_2$(110) truncation [16]. It was difficult to make the heated sapphire tube airtight and hence the quartz tube was used in the second step. We checked and confirmed that the wafer surface was free from Si contamination annealed in the quartz tube maintained at 500 ℃. Making the heated sapphire tube airtight was difficult, therefore a quartz tube was used for the second step. X-ray photoelectron spectroscopy was used to confirm that the wafer surface finished in the quartz tube was almost free from Si contamination, as shown in Figure S1 in the supplementary material.

The annealed $TiO_2$ wafer, 10 mm square and 0.5 mm thick, was fixed on a fluorocarbon polymer disk. A droplet of imaging liquid, aqueous KCl solution (0.1 mol $l^{-1}$), was placed on the wafer, not to be in contact with the disk. Contamination on the disk surface, if any, could not be transferred to the wafers surface through the liquid. The cantilever assembly was placed on top covered with a glass slip (Matsunami Glass). The slip was irradiated with a Hg–Xe lamp (San-ei Electric, UVS-204S) for 90 min to remove possible organic contamination from its surface prior to assembling.

The imaging solution of pH 6 was prepared with KCl (Nacalai tesque, 99.9%) and Milli-Q water under air. Solutions of pH 3 or 11 were prepared by adding $H_2SO_4$ (Wako, 95.0%) or KOH (Wako, 96.0%) to the original solution, respectively. $H_2SO_4$ was used instead of HCl since the latter compound is volatile and possibly corrosive to metal components of the microscope enclosed with a temperature-regulated container (Mitsubishi Electric Engineering, CN-40A) maintained at 27 ℃.

### 2.2.2 Characterization

Frequency-modulation detection of force on the probing tip was enabled with a SPM-8100FM microscope in development (Shimadzu). In topographic imaging of the wafer, the resonance oscillation of a silicon cantilever (Nanoworld, PPP-NCHAuD) was mechanically excited with a piezo-actuator. The nominal spring constant of the cantilevers was 40 N $m^{-1}$. The resonance frequency in the imaging solutions was 130–150 kHz with the quality factor of resonance ($Q$) around 10. A typical spectrum of thermally excited cantilever oscillation is shown in Figure 2. The oscillation amplitude was regulated at a preset peak-to-peak amplitude ($A$), typically 1 nm. When a conservative force was loaded on the tip, the resonance frequency of cantilever oscillation ($\Delta f$) shifted accordingly. The topography of the wafer was traced with regulation of the tip–surface distance by keeping the frequency shift ($\Delta f$) at a prefixed setpoint. Observed images were analyzed and depicted with WSxM software [17], LabVIEW (National Instruments) and a home-made routine on python.

In addition to topographic imaging, the mechanical response of the solution was probed and mapped on the planes that are perpendicular to the solution–wafer interface. The oscillating cantilever was scanned vertically from the bulk solution to the wafer. The frequency shift as a function of the vertical coordinate was recorded to obtain one $\Delta f$–distance curve. The vertical scan aborted when $\Delta f$ reached a predetermined threshold to prevent extensive tip-to-wafer contact. The cantilever was then retracted into the solution by 3 nm. We repeatedly acquired 256 vertical scans along a 5 nm long lateral coordinate. One $\Delta f$ map was constructed with acquisition time of 20–30 s.

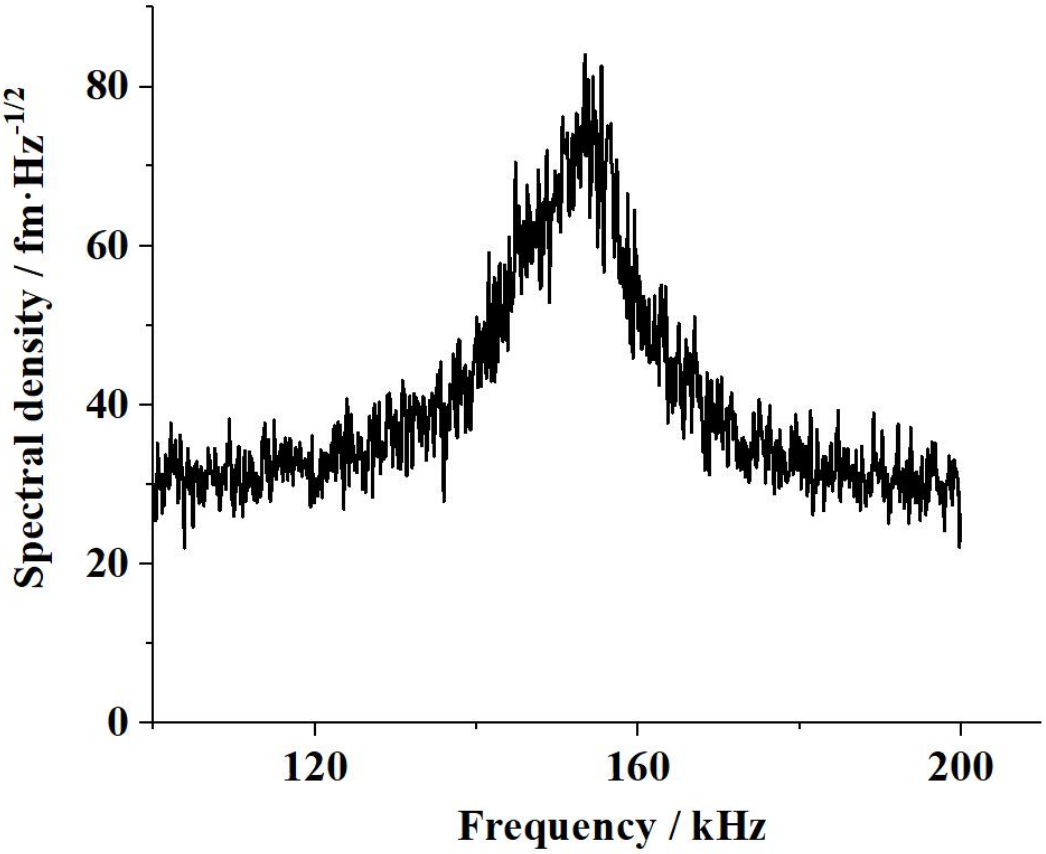


Fig. 2. A typical spectrum of thermally excited cantilever oscillation in the KCl solution.

## 2.3 RESULTS AND DISCUSSION

### 2.3.1 Terraces and steps

The annealed $TiO_2$(110) wafers presented terraces and steps in the KCl solutions of different pH. Figure 3 shows topographic images observed with positive $\Delta f$ setpoints, *i.e.* repulsive tip–surface force in the feedback regulation for tracing the topography. Terraces of 100 nm or larger in width were terminated with regular-height steps. The step height was 0.34-0.36 nm as depicted in the cross sections. The observed heights are consistent with the minimum step height predicted in the (110) truncation of rutile as illustrated in Figure 1. The steps observed in the three solutions of pH 3, 6, and 11 were nearly straight with no signs of etching. Previously, Hiasa et al. used FM-AFM to observe the $TiO_2$(110) surface and found that pollution from unknown source was spread on the $TiO_2$(110) surface [13]. However, in the present study, no pollution could be observed on the $TiO_2$ surface at different pH since two methods were used to protect the wafer from pollution from sample holder and coverglass. On the other hand, Uetsuka et al. [18] found 10-nm scale inlet-shaped steps on rutile (110) wafers immersed in neutral water or aqueous ammonia as signs of etching. Their rutile wafers were argon-ion sputtered and vacuum-annealed, while the wafers used in the present study were prepared in the oxidative atmospheres. The difference in annealing environments led to different degrees of reduction. Indeed, the annealed wafers of the present study were colorless, while vacuum-annealed $TiO_2$ wafers are blue-colored according to the temperature and time of annealing [19]. The different sensitivities to water-induced etching may be attributed to the different degrees of reduction.

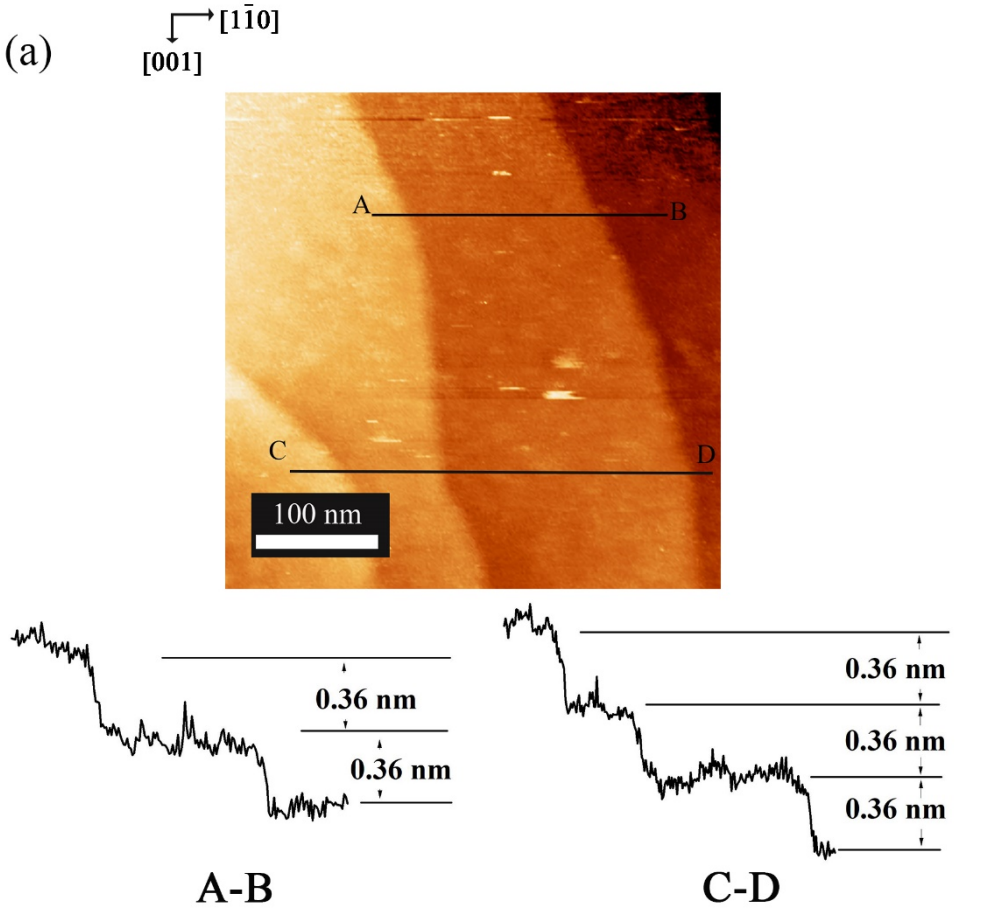
(a)
[1$\bar{1}$0]
[001]
A
B
C
D
100 nm
0.36 nm
0.36 nm
0.36 nm
0.36 nm
A-B
C-D

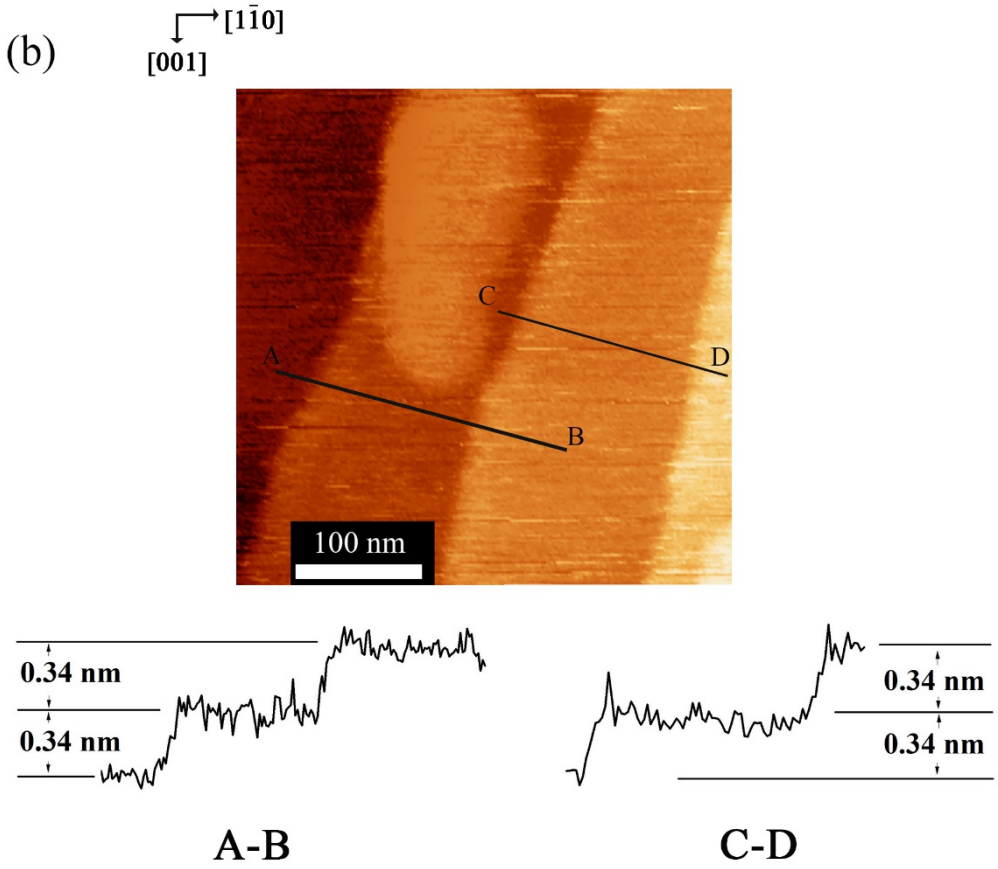
(b)
[1$\bar{1}$0]
[001]
C
A
D
B
100 nm
0.34 nm
0.34 nm
0.34 nm
0.34 nm
A-B
C-D

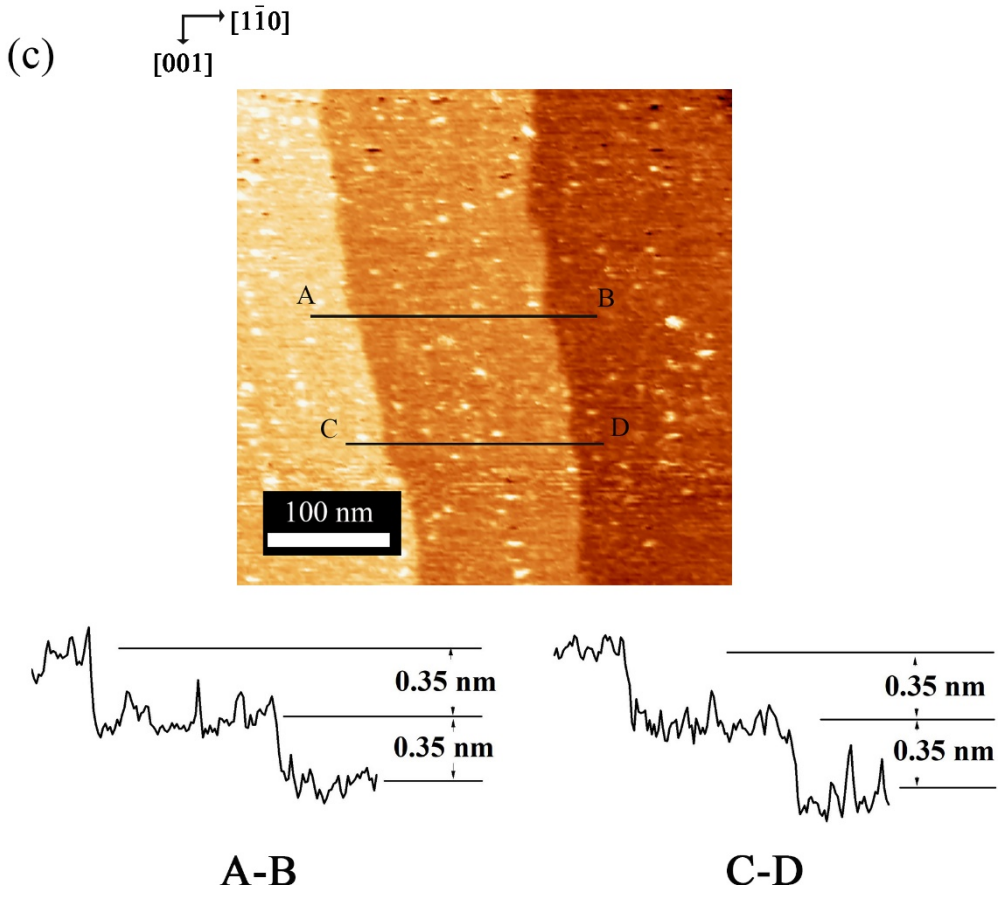


Fig. 3. (a) Terraces and single-height steps on the rutile (110) wafers. Images (a), (b), and (c) were obtained in the KCl solutions of pH 3, 6, and 11, respectively. Cross sections along A–B lines and C-D lines are shown in the right panels. Cantilever oscillation amplitude (A): 1.0 nm. Frequency-shift ($\Delta f$) setpoint: (a) +176, (b) +147, and (c) +100 Hz. Acquisition time: 320 s per frame

## 2.3.2 Atom-scale features

The stoichiometric (110) truncation of rutile involves four atomic species when prepared in a vacuum [20]. Five-fold coordinated and six-fold coordinated $Ti^{4+}$ cations are placed on a plane perpendicular to the $[1\bar{1}0]$ direction together with three-fold coordinated $O^{2-}$ anions. Two-fold coordinated $O^{2-}$ anions protrude from the plane by bridging the two neighboring six-fold coordinated Ti cations, as illustrated in Figure 1. When a probing tip simply traces the physical topography of the truncation, which was experienced in FM-AFM imaging in the vacuum [21], the bridging oxygen anions should present ridges parallel to the [001] axis separated by trenches with the five-fold coordinated Ti cations at the bottom.

The chemical composition of the (110) truncation can be complicated when buried in aqueous solutions. The major component of the solution, water, is ready to modify the composition. The five-fold coordinated Ti cations provide surface sites for molecular adsorption of water with its oxygen end down. The resultant $Ti\text{-}OH_2$ species are capable of deprotonation in a basic environment to be transformed to $Ti\text{-}OH^-$. A molecular dynamics simulation based on density functional theory predicted the pKa of the $Ti\text{-}OH_2$ species to be 9 [22]. The bridging oxygen anions can be protonated in an acidic solution. The composition is therefore sensitive to the acid-base property of the solution complicates matters in one hand. On the other hand, AFM topography when responding to the acid-base property helps us to know what species our tip has traced.

Starting with the topographic images determined in the most acidic solution examined in the present study, Figure 4(a) and Figure S2(a) presents the 8-nm square image smoothed with moving average of 3 by 3 pixels of a rutile wafer immersed in the solution of pH 3. Bright rows parallel to the [001] axis appeared on the wafer surface. The A–B cross section was determined perpendicular to the row axis and shown left below the topography. The row-to-row distance was regulated to be 0.61 nm. The C–D cross section, which is shown right below the topography, exhibited periodic corrugations along the row axis with a repetition length of 0.30 nm(Figure 4) and 0.38 nm (Figure S2).

Period in [001] direction and $[1\bar{1}0]$ direction is very important to explain the $TiO_2$(110) property in water. Fourier transformation is an active and convenient method

to detect the period order in the imaged objects. But in this case, unfortunately, the topographic image of $TiO_2$(110) in liquid was affected by drifts. The author calculated the autocorrelation of the raw image by home-made routine on Python. On $TiO_2$(110) wafers placed in the vacuum, the short-range order of Cl atoms [23], formate anions [24], and N3 dye molecules [25] were quantitatively analyzed with autocorrelation.

Autocorrelation $F(x, y)$ was calculated as a function of correlation vector $(x, y)$ as,

$$F(x,y) = \sum_{X,Y} \{H(X,Y) \cdot H(X+x, Y+y)\}$$

where $H(X, Y)$ presents the topographic height in the raw image at the lateral coordinate of $(X, Y)$. In the summation, $(X, Y)$ runs over the pixels in the raw image [26]. The autocorrelation reflects the relative location of two atom-scale protrusions. $F(x, y)$ has its maximum at the origin and normalized to be unity representing the position of the first protrusion. The correlation increases at $(x, y)$ where the occupation probability of a second protrusion is large.

The 3-nm square autocorrelation (Fig.4(b)) was thereby calculated and depicted from the raw image in (a). In autocorrelation, the bright grids parallel to the [001] direction could be recognized in the raw image. The bright dots along the ridges were missing by visual inspection. The autocorrelation was further investigated by making cross sections along lines involving the origin, as shown below the Fig 4(b). The cross-section perpendicular to the ridge axis yielded a ridge-to-ridge distance of 0.60 nm. The other cross section, which was parallel to the ridge axis, exhibited small but finite corrugations superposed on a feature monotonously decaying with the lateral distance from the origin. The corrugations were periodic with a repetition length of 0.30 nm. The corrugations in A–B and C–D cross sections fitted well with the repetition lengths deduced from the autocorrelation. The autocorrelation provided a correct average of period on $TiO_2$(110) surface. The period of [001] direction was 0.30 nm, and the period of $[1\bar{1}0]$ direction was 0.60 nm. Another image observed on the same wafer with a different cantilever was similarly analyzed to check reproducibility. Compatible meshes of 0.54 nm by 0.29 nm were yielded as shown in Figure. S2 in the supporting information.

Hence, the protruding particles were assigned to the bridging oxygen anions. Since the isoelectric point of the $TiO_2$(110) surface is pH 4.8-5.5 [27], the bridging oxygen anions accommodate protons fully or partially in the acidic solution. The topographic height of a bridging anion should, in principle, be sensitive to the presence or absence of the adsorbed proton. However, the proton-induced difference in topography may be insufficient to be recognized in our precision of topographic imaging. There was no sign of $HSO_4^-$ or $SO_4^{2-}$ anions adsorbed on the $TiO_2$ surface. The topographic amplitudes in the cross sections fluctuated by 0.05 nm.

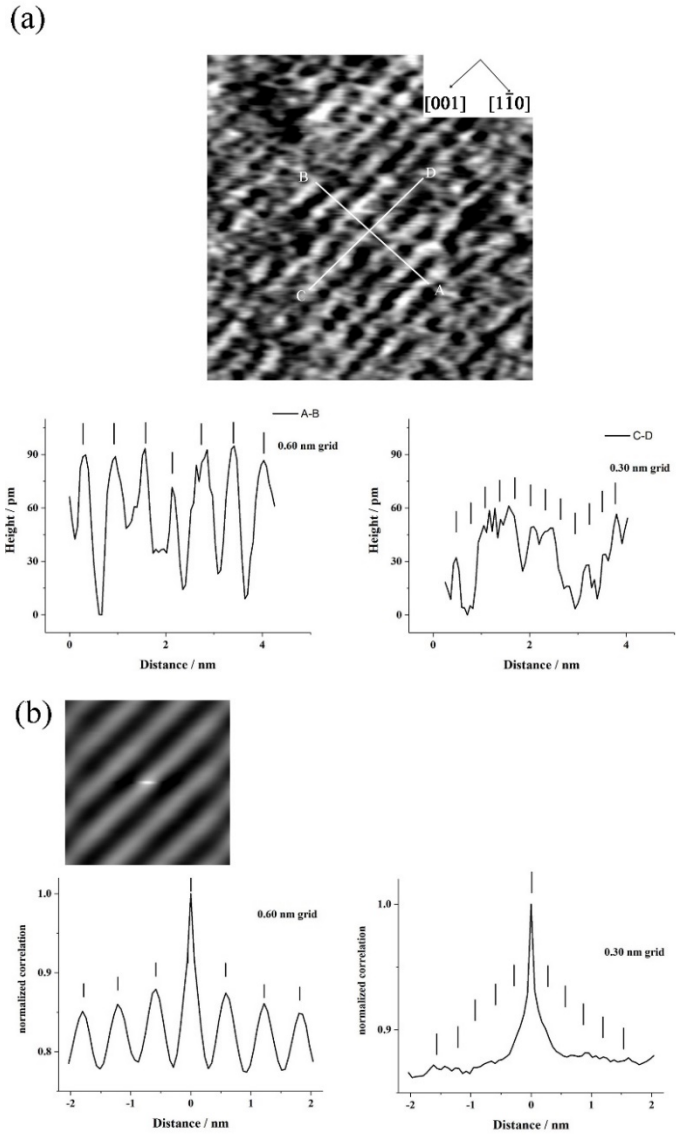


Fig. 4. Atom-scale topography of the rutile (110) wafers in the KCl solution of pH 3. A raw topographic image of 8 × 8 $nm^2$ was average-filtered shown in (a). Cross sections along A–B and C–D are shown in the lower panels. Frequency-shift setpoint: +321 Hz. Acquisition time: 10 s per frame. A self-correlation of the topography was determined

in a 3 × 3 $nm^2$ and inserted in the topography shown in (b). The correlation curves involving the origin and parallel to the [$1\bar{1}0$] and [001] directions are presented on the lower panels.

The second image, Figure 5(a), was observed on a nearly isoelectric interface in a solution of pH 6. The imaged wafer was prepared just thorough annealing at 1000°C in the sapphire tube by skipping second-stage annealing in the quartz tube. Bright particles ordered in a (1×1) symmetry were again observed. As depicted in the A–B and C–D cross sections, the repetition lengths perpendicular and parallel to the [001] axis were 0.73 and 0.28 nm, respectively. The amplitude of the topographic corrugations in the A–B cross section was 0.1 nm. Compatible meshes of 0.73 nm by 0.28 nm were yielded as shown in Fig. S3 in the supporting information. These repetition lengths as well as the corrugation amplitude were comparable to those observed in the acidic solution. Hence, the (1×1)-ordered particles were also assigned to the bridging oxygen anions.

The present results were compared with the results from earlier reports. Sasahra et al. observed the vacuum-prepared $TiO_2$(110) wafer in pure water by FM-AFM [14]. A 0.6 nm period along the [$1\bar{1}0$] direction could be observed while no period was observed along the [001] direction. In contrast, the present study observed the period along the [001] direction. Although both studies used FM-AFM to observe a cleaned $TiO_2$(110) wafer in water, the difference in result may be due to the improvement of FM-AFM performance in the past 10 years. Serrano et al. conducted topographic imaging of a vacuum-prepared $TiO_2$(110) wafer in pure water by scanning tunneling microscope (STM) [8]. The result presented a 0.70 nm period distance of ridge-to-ridge parallel to the [001] direction, which is consistent with the finding of the present study. However, Serrano et al. found a two-fold periodicity distance along the [001] direction, which is caused by the hydrogen-bonded water dimers trapped on the five-fold coordinated Ti actions. In contrast, one-fold period was observed along the [001] direction in the present study, as compared to two-fold periodicity shown in Serrano et al. One possible explanation is that we used a different method to scan the $TiO_2$(110) surface, that is, AFM versus STM. The hydrogen-bonded water dimers which is trapped on the five-fold coordinated Ti actions may be thrusted by AFM tip. The mechanical

force on the AFM tip was in the order of 0.1 nN, while the force on the STM tip was unknown.

Many STM studies [8,28-29] reported two-fold period along the [001] direction on vacuum-prepared $TiO_2$(110) wafers exposed to liquid water or water and scanned in the vacuum. In particular, Balajka et al. [29] pointed out that the two-fold periodicity was the acetate anions which was chemisorbed on the five-fold coordinated Ti actions on the $TiO_2$(110) wafer after exposure to water. They found that acetate anions came from atmosphere. The $TiO_2$(110) wafer exposed to the specially purified water exhibited one-fold periodicity. In the present study, the $TiO_2$(110) wafer also exhibited one-fold periodicity along the [001] direction, since the acetate anions could be dissolved in liquid water, which is a good solvent, and not chemisorbed on the wafer.

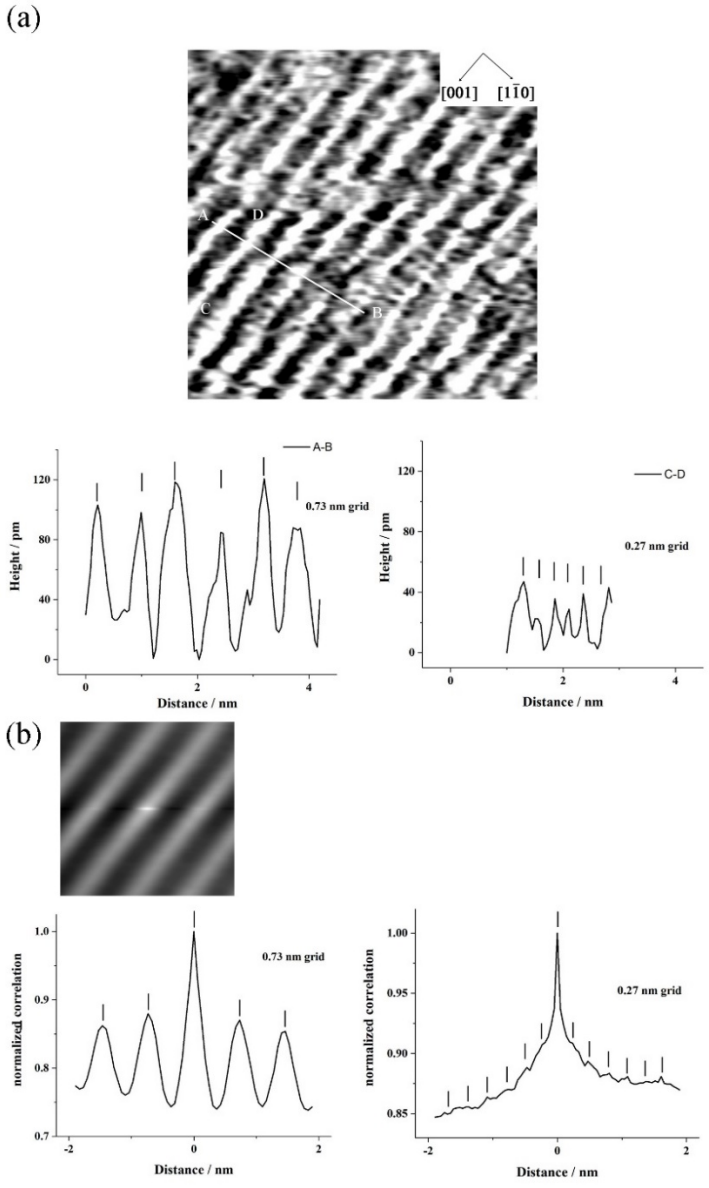

Fig. 5. Atom-scale topography of the rutile (110) wafers in the KCl solution of pH 6. A raw topographic image of 8 × 8 $nm^2$ was average-filtered shown in (a). Cross sections along A–B and C–D are shown in the lower panels. Frequency-shift setpoint: +288 Hz. Acquisition time: 10 s per frame. A self-correlation of the topography was determined in a 3 × 3 $nm^2$ and inserted in the topography shown in (b). The correlation curves involving the origin and parallel to the $[1\bar{1}0]$ and [001] directions are presented in the lower panels.

In figure 6(a), the FM-AFM image of $TiO_2$(110) surface at pH 11 has shown. As depicted in the A-B cross sections, the repetition length perpendicular to the [001] axis was 0.68 nm. It is ×1 order on the $[1\bar{1}0]$ direction. However, as depicted in the C-D cross sections, the repetition length parallel to the [001] axis is difficult to identify periodicity by visual inspection as compared to that in a solution of pH 6. The autocorrelation image was show in (b). Corrugations in the A–B cross section was accordingly less periodic, while they fitted 0.68-nm grids. The length in the autocorrelation represented the short-range order averaged over the raw image. Figure S4 presented a repetition length of 0.75 nm in its autocorrelation on the same wafer with the same cantilever. The repetition length on the $[1\bar{1}0]$ direction ranges from 0.63 to 0.75 nm, which is an indication of one-fold periodicity along the $[1\bar{1}0]$ direction.

Along the [001] direction, the repetition length of 0.45 nm can be observed in C-D cross section. The amplitude of the corrugations was 0.05 nm. In Figure S4, the repetition length was 0.60 nm along the [001] direction. The author recognized the repetition length of 0.45-0.60 nm to be twice of the unit cell length along the [001] direction. The $TiO_2$(110) surface showed a (2 × 1) structure at pH 11 by the autocorrelation of Figure 5 and Figure S4.

At pH 11, the equilibrated deprotonation of Ti-$OH_2$ shifts to produce Ti-OH- on the five-fold coordinated Ti cations. Direct adsorption of OH- species from the solution is also possible. The AFM cantilever detected the OH groups as raised dots on the topography. An X-ray crystal truncation rod study [30] presented that Ti-OH bond was perpendicular to the surface with the length of 0.20 nm. The bridging oxygen anions were 0.14 nm higher than the plane of Ti cations. Hence, the OH groups adsorbed on

the five-fold coordinated Ti cations is 0.06 nm higher than the plane of bridging oxygen anions. When the OH groups were 50% relative to the five-fold coordinated Ti cations, the two-fold periodicity was observed as shown in Figures 6 and S4. The negatively charged species should be evenly distributed in each trench to reduce electrostatic repulsion. The acetic acid is miscible in the water, and its concentration does not differ between pH 6 and pH 11. At pH 6, acetic acid was not adsorbed on the $TiO_2$(110) surface. At pH 11, the two-fold periodicity was not caused by the acetic acid. The author therefore hypothesizes that the OH groups chemisorbed on the five-fold coordinated Ti cations produced the swellings visualized in Figures 6 and S4.

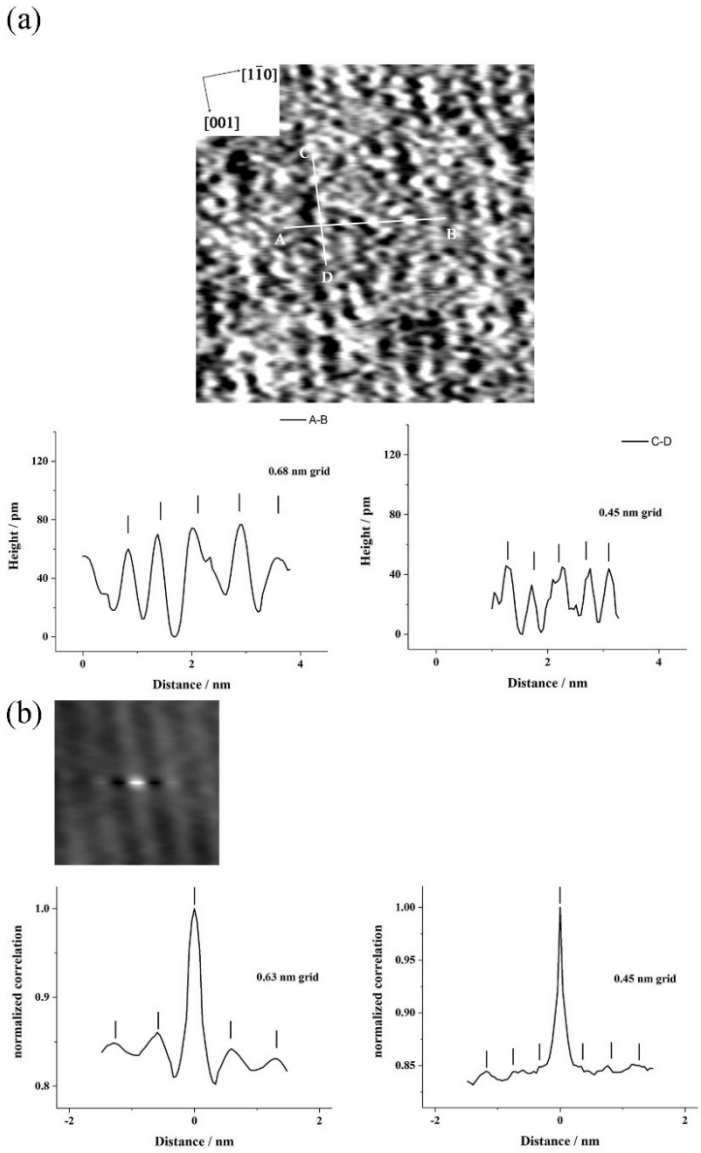


Fig. 6. Atom-scale topography of the rutile (110) wafers in the KCl solution of pH 11. A raw topographic image of 8 × 8 $nm^2$ was average-filtered shown in (a). Cross sections along A–B and C–D are shown in the lower panels. Frequency-shift setpoint:

+167 Hz. Acquisition time: 10 s per frame. A self-correlation of the topography was determined in a 3 × 3 $nm^2$ and inserted in the topography shown in (b). The correlation curves involving the origin and parallel to the [1$\bar{1}$0] and [001] directions are presented on the lower panels.

## 2.3.3 Water structured at interfaces

The relationship between microscopic hydration structure and solution pH value is of great interest. $TiO_2$ shows different performance under different pH. Although it is well known that pH can affect the photocatalytic activity [15], it is unclear how change of pH can affect the activity. It is hypothesized that change of pH may change the water structure on $TiO_2$, therefore research on water structure on $TiO_2$ could enhance our understanding of the actions on $TiO_2$ surface. Here, the hydration structure of $TiO_2$(110) surface was investigated by FM-AFM. Frequency shift of cantilever($\Delta f$) observed at solid-liquid interfaces can reflect the local density distribution of the solvent molecules [31].

Figure 7(a),(c),and (e) show $\Delta f$ maps obtained by measuring the variation of the frequency shift of cantilever, as a function of distance from the surface and lateral distance on the surface. Images show 2D frequency shift variation, with black indicating negative frequency shift and white indicating positive frequency shift. Only at pH6, at least two $\Delta f$ oscillations (layer 1 and layer 2) can be seen on the $TiO_2$ substrate in the form of lighter and darker area. The frequency shift oscillations correspond to the local water density variations. As shown in Figure 7(a), (c), and (e), $\Delta f$ distribution observed above the $TiO_2$(110) surface. The probe apexes with closely bound water molecules are not invasive and come closest to directly measuring the unperturbed water density above a surface. Tip apexes with closest to directly measuring the unperturbed water density above a surface. This experiment satisfies the conditions of solvent-tip approximation (STA) [32]. So, the part with high water density appears on the side of the force peak that faces the surface.

At pH 6 (Figure 7(c)), there are at least two layers of regular water molecules that are hydrations layers on the $TiO_2$(110) surface. At pH 3 and pH 11, no frequency shift oscillations can be observed, indicating no hydration layers on the surface. Figure 7(b),

(d), and (f) show the force-distance curve after averaging over the white arrow from 5 lines and calculated from $\Delta f$ curve using the Sader equation [33]. The same was shown in $\Delta f$ maps at pH 6, only at pH 6 the force oscillations were observed above the $TiO_2$(110) surface, as shown by force curve located at ~0.5 nm and ~0.8 nm from the $TiO_2$(110) surface. The distance between the two force oscillations is about 0.3nm, which is consistent with the expected thickness of a water molecule layer [34]. As shown in red dotted circle, some dark blob features just above the interface. Those dark blob features are locked above the surface depression portion. That is the position of 5-fold coordinated Ti atom. The highest density of $H_2O$ molecules is slightly under the dark blob features [32]. It is possible that the layer is $H_2O$ molecules adsorbed on 5-fold coordinated Ti atoms. Only at pH 6, $TiO_2$(110) surface showed a clearly visible hydration structure as shown in Figure 7(c). Asakawa at al. [35] uses DFT MD simulation to analysis the interface between brookite (210) and water, and also shows two hydration layers on the surface and the same distance between the two hydration structures.

In Figures 7(a) and (e), At pH 3 and pH 11, the hydration structure was weak to invisible. At pH 3, proton in water combine with the bridging oxygen on $TiO_2$(110) surface, then the bridging oxygen changed from $O^{2-}$ to $OH^-$. In this situation, there are two types of ions on $TiO_2$(110) surface, $Ti^{4+}$ and $OH^-$. The ion charge difference between the two ions is 5. At pH 11, hydroxide in water combine with $Ti^{4+}$ on $TiO_2$(110) surface. In this situation, only combined $OH^-$ and bridging oxygen $O^{2-}$ are on $TiO_2$(110) surface. The ion charge difference between the two ions is 1. At pH 6, $Ti^{4+}$ and bridging oxygen $O^{2-}$ are on $TiO_2$(110) surface. In this situation, the ion charge between two ions is 6, which is the maximum. The top atoms can affect the hydration structure on the atoms [36]. If the atoms charge is close, affected hydration structure will also be close. The hydration structure in AFM images shows the weakly contrast between on surface. At pH 6, the large ionic charge between $Ti^{4+}$ and $O^{2-}$ makes it easier to distinguish the hydration structure. At pH 3 and pH 11, the ionic charge on $TiO_2$(110) surface is not strong enough, therefore the hydration structure is weak or invisible. In view of the above, the charging of the entire $TiO_2$(110) surface do not enhance the hydration structure of water.

The present results are compared with earlier reports. Zhang et al. presented two layers of water on the $TiO_2$(110) surface by X-ray crystal truncation rod [30]. In pure water, the five-fold coordinated Ti cations absorbed with a mixture of water molecules and hydroxyl groups. An additional hydration layer is observed above this mixture layer. That is consistent with the present study in near isoelectric point situation. The two layers observed on the $TiO_2$(110) surface correspond to the mixture layer and hydration layer. Under alkaline condition, Zhang et al. presented the hydroxyl groups absorbed on the five-fold coordinated cations. On the hydroxyl groups, an additional hydration layer could be observed. Since hydration bond is weaker than the bond between five-fold coordinated Ti cations and hydroxyl groups, which may explain why no hydration layer can be observed at pH 11 in the present study.

Schlegel et al. conducted a sum-frequency-generation (SFG) study on the water-$TiO_2$ interface [37]. Different from the previous paper [7], Schlegel et al. chose $D_2O$ instead of $H_2O$ since the water from the $TiO_2$ crystal affected experimental results. Schlegel et al. reported that the water molecules were facing the opposite directions on different sides of isoelectric point: when the pD is below the isoelectric point, water molecules' deuterium atoms point away from $TiO_2$ surface; when pD is higher than the isoelectric point, water molecules' deuterium atoms point toward $TiO_2$ surface. This could also be the reason why hydration layer could not be observed at pH 3 and pH 11. At pH 3 and pH 11, water molecules all point toward the same direction near the surface. The contrast in AFM images was not high enough without forming a distinctive layer. Near the isoelectric point, water molecules direction was messy from a wide area. But in a local area, there may be a law of positive and negative alignment. This could be reason why hydration layer can be observed at pH 6 in the present study.

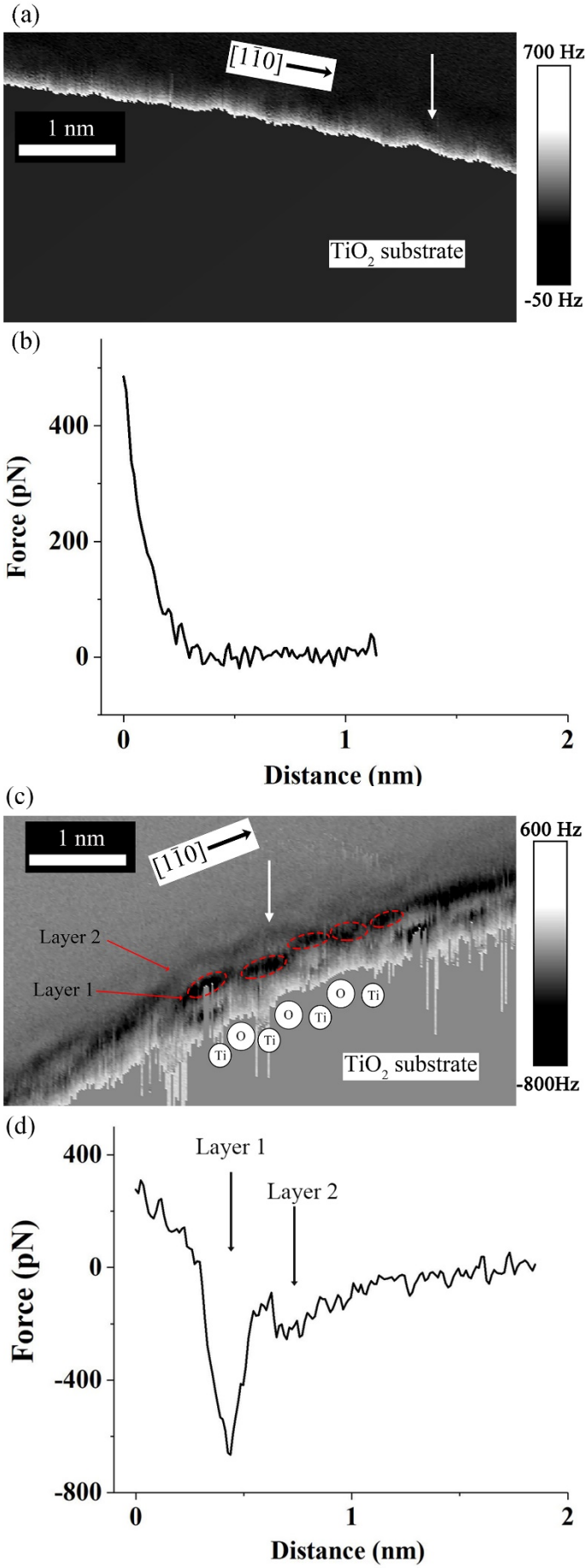
(a)
[1$\bar{1}$0]
1 nm
TiO2 substrate
700 Hz
-50 Hz
(b)
Force (pN)
400
200
0
0
1
2
Distance (nm)
(c)
1 nm
[1$\bar{1}$0]
Layer 2
Layer 1
O
Ti
TiO2 substrate
600 Hz
-800Hz
(d)
Layer 1
Layer 2
Force (pN)
400
0
-400
-800
0
1
2
Distance (nm)

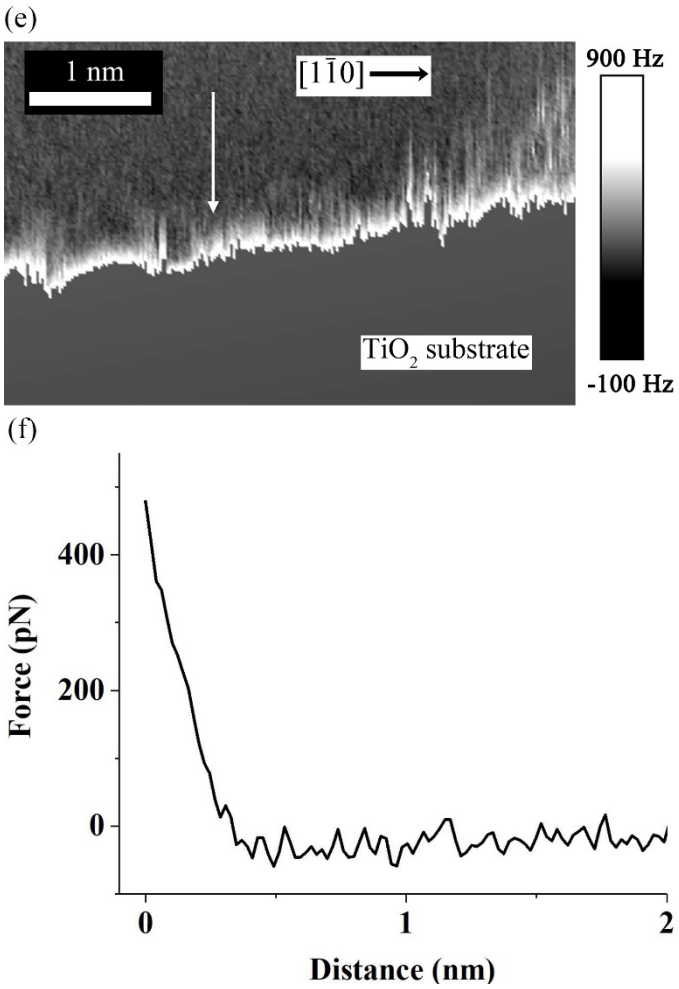


Fig. 7. (a) FM-AFM $\Delta f$ distribution observed above the $TiO_2$ (110) surface in 0.1M KCl aqueous solution at pH3. (b) A force-distance curve of marked line in (a). (c) FM-AFM $\Delta f$ distribution observed above the $TiO_2$ (110) surface in 0.1M KCl aqueous solution at pH6. (d) A force-distance curve of marked line in (c). (e) FM-AFM $\Delta f$ distribution observed above the $TiO_2$ (110) surface in 0.1M KCl aqueous solution at pH11. (f) A force-distance curve of marked line in (e).

## 2.4 CONCLUSION

(1) The air-annealed $TiO_2$(110) surface was observed in aqueous solution at different pH values. At pH 3,6 and 11, the $TiO_2$(110) all showed step and terrace structures as a clean surface.

(2) On the $TiO_2$(110) surface, the atomic surface structures were observed at pH 3,6 and 11. At pH 3 and 6, (1×1) pattern can be first observed. At pH 11, only the ×1 pattern along the [$1\bar{1}0$] can be observed. At pH 11, the $OH^-$ combined with 5-fold Ti atoms, which make surface flatter.

(3) The $\Delta f$ maps obtained by measuring the variation of the cantilever frequency shift show the hydration structure on the $TiO_2$(110) surface at pH 3, 6 and 11. Only at pH 6, the hydration structure can be observed clearly since there are different electric charges at different pH values, which reveals the effect of different pH values on the hydration structure on $TiO_2$(110) surface.

## 2.5 REFERENCE


1. Capwell R J, Spagnolo F, DeSesa M A. A rapid determination of low concentrations of anatase in rutile $TiO_2$ pigments by Raman spectroscopy. *Applied Spectroscopy*, 1972, 26, 537-539.

2. Auffan M, Pedeutour M, Rose J, Masion A, Ziarelli F, Borschneck D, Chaneac C, Botta C, Chaurand P, Labille J, Bottero J. Structural degradation at the surface of a $TiO_2$-based nanomaterial used in cosmetics. *Environmental science & technology*, 2010, 44, 2689-2694.

3. Tang H, Prasad K, Sanjines R, Levy F. $TiO_2$ anatase thin films as gas sensors. *Sensors and Actuators B: Chemical*, 1995, 26, 71-75.

4. Fujishima A, Zhang X, Tryk D A. $TiO_2$ photocatalysis and related surface phenomena. *Surface Science Reports*, 2008, 63, 515-582.

5. Onishi H, Iwasawa Y. Reconstruction of $TiO_2$ (110) surface: STM study with atomic-scale resolution. *Surface Science*, 1994, 313 ,L783-L789.

6. Zhang Z, Fenter P, Cheng L, Cheng L, Sturchio N.C, Bedzyk M.J, Predota M, Bandura A, Kubicki J.D., Lvov S.N., Cummings P.T., Chialvo A.A. Ridley M.K., Benezeth P, Anovitz L, Palmer D.A., Machesky M.L., Wesolowski D.J. Ion adsorption at the rutile− water interface: Linking molecular and macroscopic properties. *Langmuir*, 2004, 20, 4954-4969.

7. Kataoka S, Gurau M C, Albertorio F, Holden M.A., Lim S.M., Yang R.D., Cremer P.S., Investigation of water structure at the $TiO_2$/aqueous interface. *Langmuir*, 2004, 20, 1662-1666.

8. Serrano G, Bonanni B, Di Giovannantonio M, Kosmala T, Schmid M, Diebold U, Carlo A.D., Cheng J., VandeVondele J., Wandelt K., Goletti C. Molecular ordering at the interface between liquid water and rutile $TiO_2$ (110). *Advanced Materials Interfaces*, 2015, 2, 1500246.

9. Fukuma T, Kobayashi K, Matsushige K, Yamada H, True atomic resolution in liquid by frequency-modulation atomic force microscopy. *Applied Physics Letters*, 2005, 87, 034101.

10. Sader J E, Jarvis S P. Accurate formulas for interaction force and energy in frequency modulation force spectroscopy. *Applied Physics Letters*, 2004, 84, 1801-1803.

11. Fukuma T, Higgins M J, Jarvis S P. Direct imaging of individual intrinsic hydration layers on lipid bilayers at Ångstrom resolution. *Biophysical Journal*, 2007, 92, 3603-3609.

12. Hiasa T, Kimura K, Onishi H,Ohta M, Watanabe K, Kokawa R, Oyabu N, Kobayashi K, Yamada H. Solution–$TiO_2$ Interface Probed by Frequency-Modulation Atomic Force Microscopy. *Japanese Journal of Applied Physics*, 2009, 48, 08JB19.

13. Sasahara A, Tomitori M. Frequency modulation atomic force microscope observation of $TiO_2$ (110) surfaces in water. *Journal of Vacuum Science & Technology B*, 2010, 28, C4C5-C4C10.

14. Zaban A, Ferrere S, Sprague J, Gregg B.A., pH-dependent redox potential induced in a sensitizing dye by adsorption onto $TiO_2$. *The Journal of Physical Chemistry B*, 1997, 101, 55-57.

15. Ohtani B, Okugawa Y, Nishimoto S, Kagiya T. Photocatalytic activity of titania powders suspended in aqueous silver nitrate solution: correlation with pH-dependent surface structures. *Journal of Physical Chemistry*, 1987, 91, 3550-3555.

16. Sasahara A, Murakami T, Tomitori M. Nanoscale characterisation of $TiO_2$ (110) annealed in air. *Applied Surface Science*, 2018, 428, 1000-1005.

17. Horcas I, Fernández R, Gomez-Rodriguez J M, Colchero J, Gomez-Herrero J, Baro A.M. WSXM: a software for scanning probe microscopy and a tool for nanotechnology. *Review of Scientific Instruments*, 2007, 78, 013705.

18. Uetsuka H, Sasahara A, Onishi H. Topography of the rutile $TiO_2$ (110) surface exposed to water and organic solvents. *Langmuir*, 2004, 20, 4782-4783.

19. Li M, Hebenstreit W, Diebold U, Tyryshkin A.M, Bowman M.K, Dunham G.G, Henderson M.A. The influence of the bulk reduction state on the surface structure and morphology of rutile $TiO_2$(110) single crystals. *The Journal of Physical Chemistry B*, 2000, 104: 4944-4950.

20. Diebold U. The surface science of titanium dioxide. *Surface Science Reports*, 2003, 48: 53-229.

21. Fukui K, Onishi H, Iwasawa Y. Atom-resolved image of the $TiO_2$ (110) surface by noncontact atomic force microscopy. *Physical Review Letters*, 1997, 79: 4202.

22. Cheng J, Sprik M. Acidity of the aqueous rutile $TiO_2$ (110) surface from density functional theory based molecular dynamics. *Journal of Chemical Theory and Computation*, 2010, 6: 880-889.

23. Diebold U, Hebenstreit W, Leonardelli G, Schmid M, Varga P. High Transient Mobility of Chlorine on $TiO_2$(110): Evidence for``Cannon-Ball"Trajectories of Hot Adsorbates. *Physical Review Letters*, 1998, 81, 405.

24. Onishi H, Fukui K, Iwasawa Y. Space-correlation analysis of formate ions adsorbed on $TiO_2$(110). *Japanese Journal of Applied Physics*, 1999, 38, 3830.

25. Ikeda M, Koide N, Han L, Pang C L, Sasahara A, Onishi H. Lateral distribution of N3 dye molecules on $TiO_2$(110) surface. *Journal of Photochemistry and Photobiology A: Chemistry*, 2009, 202, 185-190.

26. $F(x, y)$ should be symmetric with respect to the origin by definition. The authors practically restricted the summation range of $(X, Y)$ not to place $(X+x, Y+y)$ out of the raw image. The autocorrelation summed under the restriction slightly deviated from the inversion symmetry.

27. Bullard J W, Cima M J. Orientation dependence of the isoelectric point of $TiO_2$ (rutile) surfaces. *Langmuir*, 2006, 22: 10264-10271.

28. Hussain H, Tocci G, Woolcot T, Torrelles X, Pang C L, Humphrey D.S, Yim C.M, Grinter D.C, Cabailh G, Bikondoa O, Lindsay R, Zegenhagen J, Michaelides A, Thornton G. Structure of a model $TiO_2$ photocatalytic interface. *Nature materials*, 2017, 16, 461.

29. Balajka J, Hines M A, DeBenedetti W J I, Komora M, Pavelec J, Schmid M, Diebold U. High-affinity adsorption leads to molecularly ordered interfaces on $TiO_2$ in air and solution. *Science*, 2018, 361, 786-789.

30. Zhang Z, Fenter P, Sturchio N C, Bedzyk M J, Machesky M L, Wesolowski D.J. Structure of rutile $TiO_2$(110) in water and 1 molal Rb+ at pH 12: Inter-relationship among surface charge, interfacial hydration structure, and substrate structural displacements. *Surface Science*, 2007, 601, 1129-1143.

31. Amano K, Suzuki K, Fukuma T, Takahashi Ohgi, Onishi H. The relationship between local liquid density and force applied on a tip of atomic force microscope: A theoretical analysis for simple liquids. *The Journal of Chemical Physics*, 2013, 139, 224710.

32. Watkins M, Reischl B. A simple approximation for forces exerted on an AFM tip in liquid. *The Journal of Chemical Physics*, 2013, 138, 154703.

33. Sader J E, Jarvis S P. Accurate formulas for interaction force and energy in frequency modulation force spectroscopy. *Applied Physics Letters*, 2004, 84, 1801-1803.

34. Fukuma T, Reischl B, Kobayashi N, Spijker P, Canova F.F, Miyazawa K, Foster A.S. Mechanism of atomic force microscopy imaging of three-dimensional hydration structures at a solid-liquid interface. *Physical Review B*, 2015, 92, 155412.

35. Asakawa H, Holmström E, Foster A S, Kamimura S, Ohno T, Fukuma T. Direct Imaging of Atomic-Scale Surface Structures of Brookite $TiO_2$ Nanoparticles by Frequency Modulation Atomic Force Microscopy in Liquid. *The Journal of Physical Chemistry C*, 2018, 122, 24085-24093.

36. Ito F, Kobayashi K, Spijker P, Spijker P, Zivanovic L, Umeda K, Nurmi T, Holmberg N, Laasonen K, Foster A.S, Yamda H. Molecular resolution of the water interface at an alkali halide with terraces and steps. *The Journal of Physical Chemistry C*, 2016, 120: 19714-19722.

37. Schlegel S J, Hosseinpour S, Gebhard M, Devi A, Bonn M, Backus E H.G. How water flips at charged titanium dioxide: an SFG-study on the water–$TiO_2$ interface. *Physical Chemistry Chemical Physics*, 2019, 21, 8956-8964.

## 2.6 SUPPORTING INFORMATION

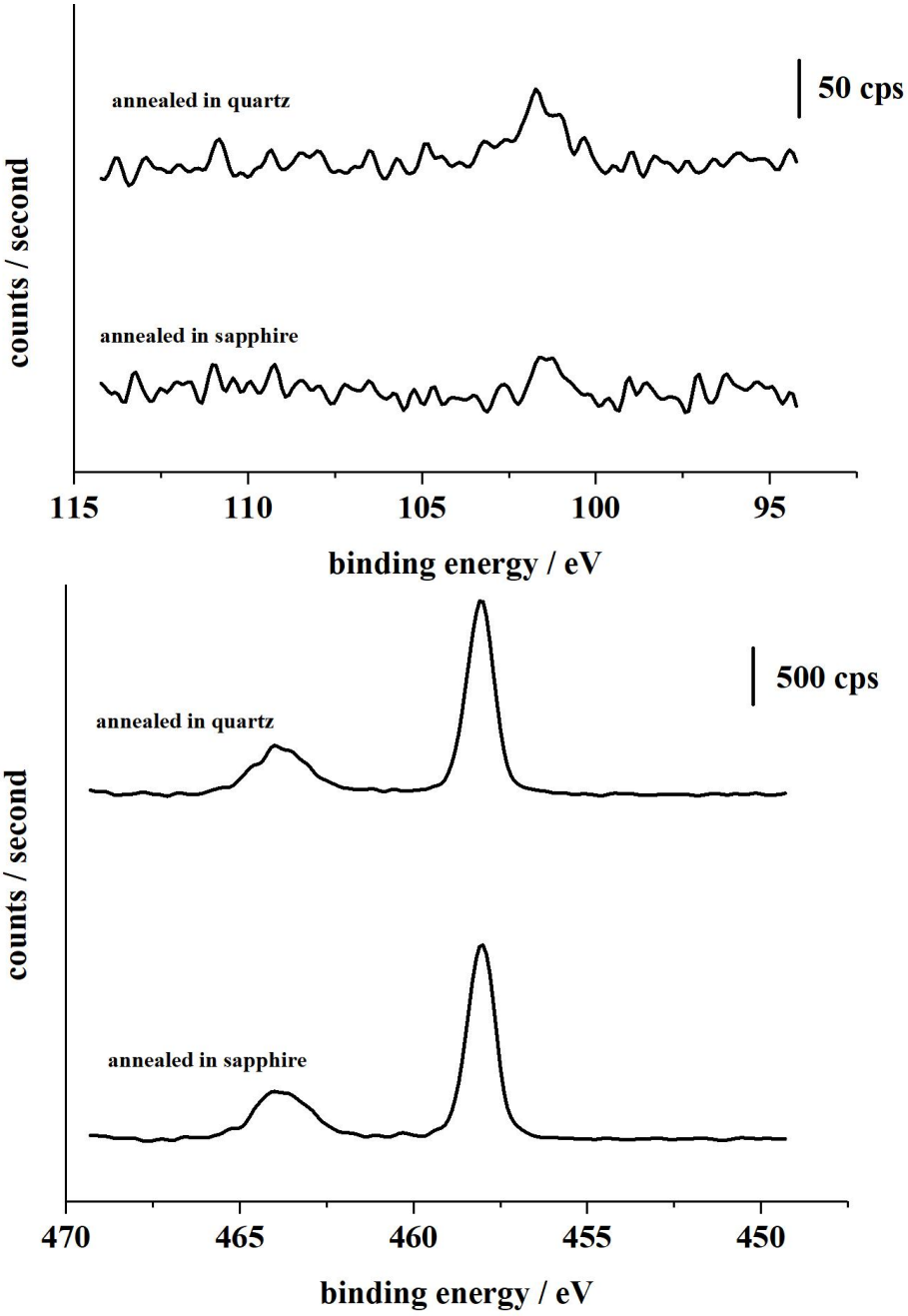


Fig. S1. X-ray photoelectron spectra of two rutile (110) wafers annealed in a quartz crucible or a sapphire tube at 1000°C. One wafer was annealed four times for 12 h each in the quartz crucible, while the other was heated in the sapphire tube once for 12 h. Peaks at a binding energy of 102 eV in the left panel are assigned to Si 2p emission. Peaks at 458 and 464 eV in the right panel are ascribed to Ti 2p3/2 and 2p1/2 emissions, respectively. The spectra were observed with a spectrometer (Ulvac-Phi, PHI X-tool) with an Al Kα excitation source. The accumulation time per spectrum and the electron pass energy in the analyzer were fixed in recording the four spectra.

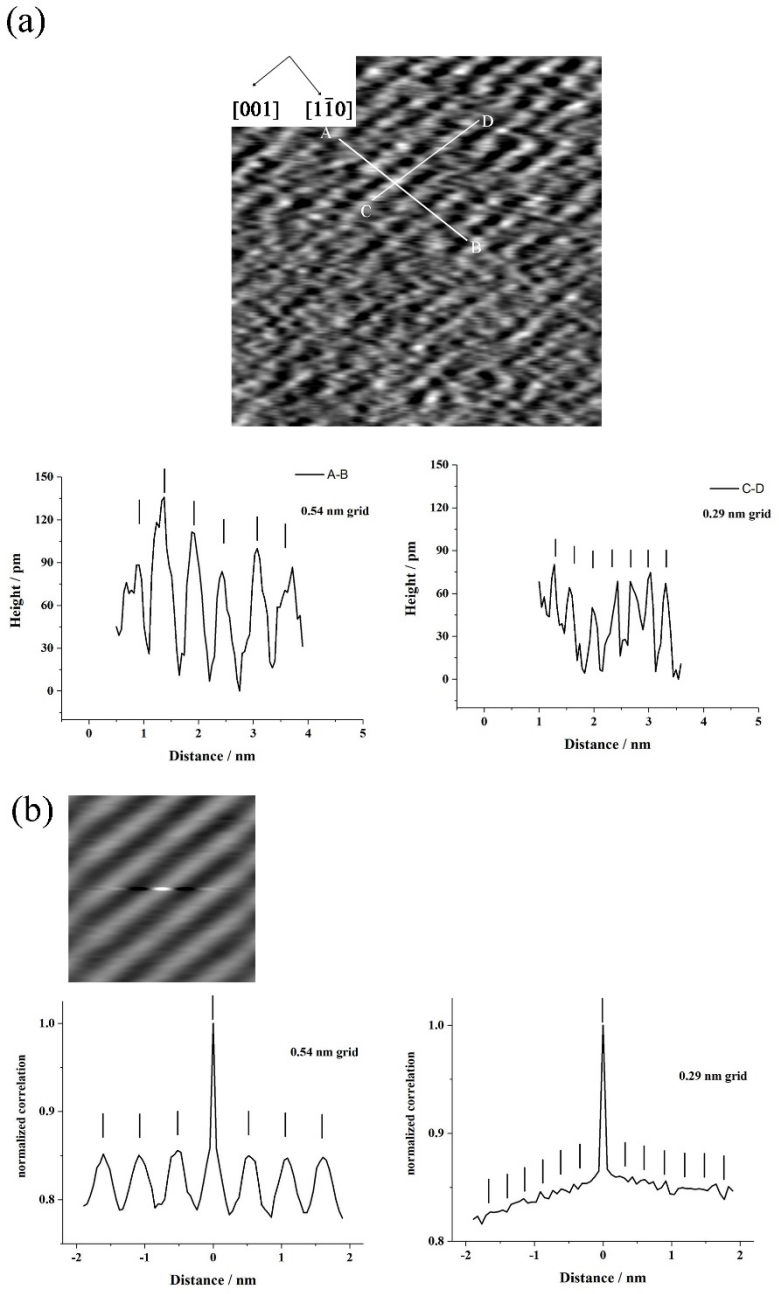


Fig. S2. Atom-scale topography of the rutile (110) wafers in the KCl solution of pH 3. A raw topographic image of 8 × 8 nm$^2$ was average-filtered as shown in (a). Cross sections along A–B and C–D are shown in the lower panels. Frequency-shift setpoint: +278 Hz. Acquisition time: 10 s per frame. A self-correlation of the topography was determined in a 3 × 3 nm$^2$ and inserted in the topography shown in (b). The correlation curves involving the origin and parallel to the [1$\bar{1}$0] and [001] directions are presented on the lower panels.

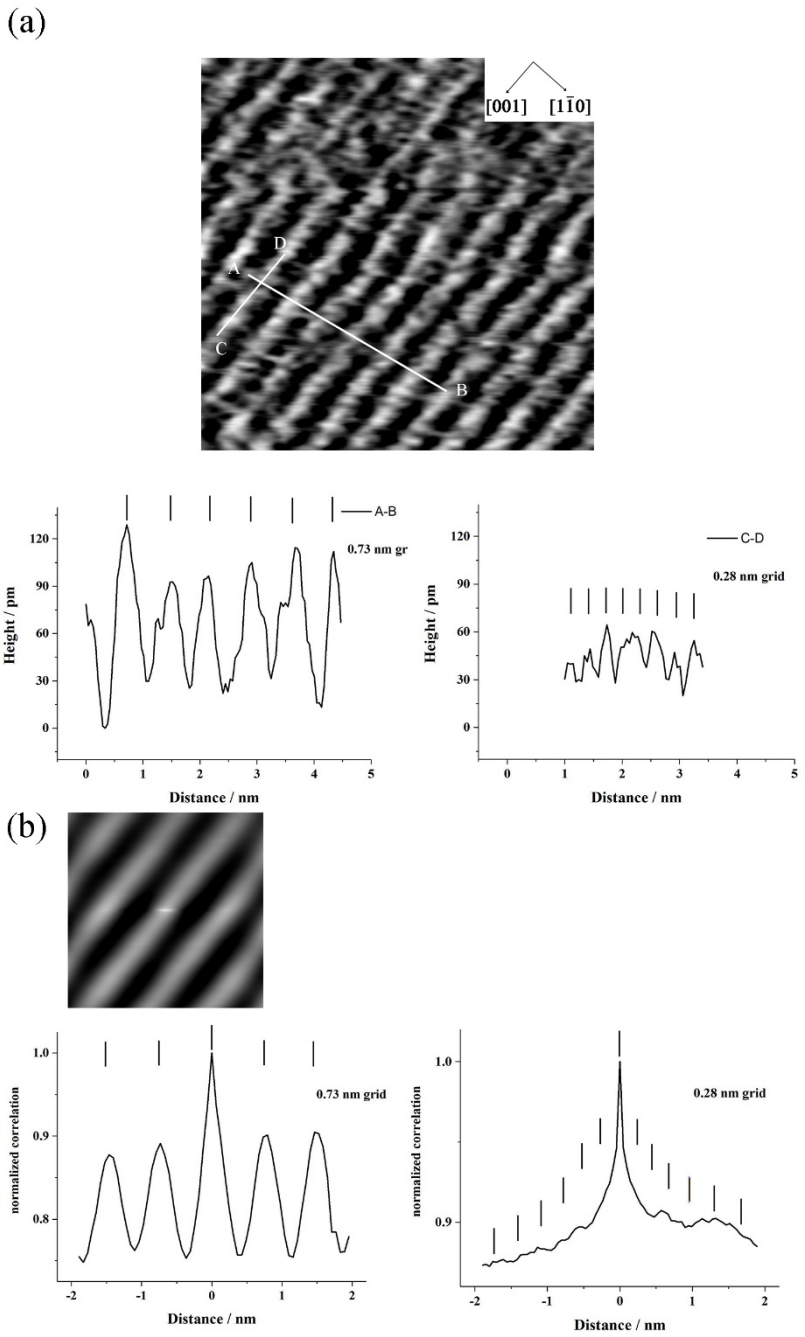


Fig. S3. Atom-scale topography of the rutile (110) wafers in the KCl solution of pH 6. A raw topographic image of 8 × 8 nm$^2$ was average-filtered as shown in (a). Cross sections along A–B and C–D are shown in the lower panels. Frequency-shift setpoint: +348 Hz. Acquisition time: 10 s per frame. A self-correlation of the topography was determined in a 3 × 3 nm$^2$ and inserted in the topography shown in (b). The correlation curves involving the origin and parallel to the [1$\bar{1}$0] and [001] directions are presented on the lower panels.

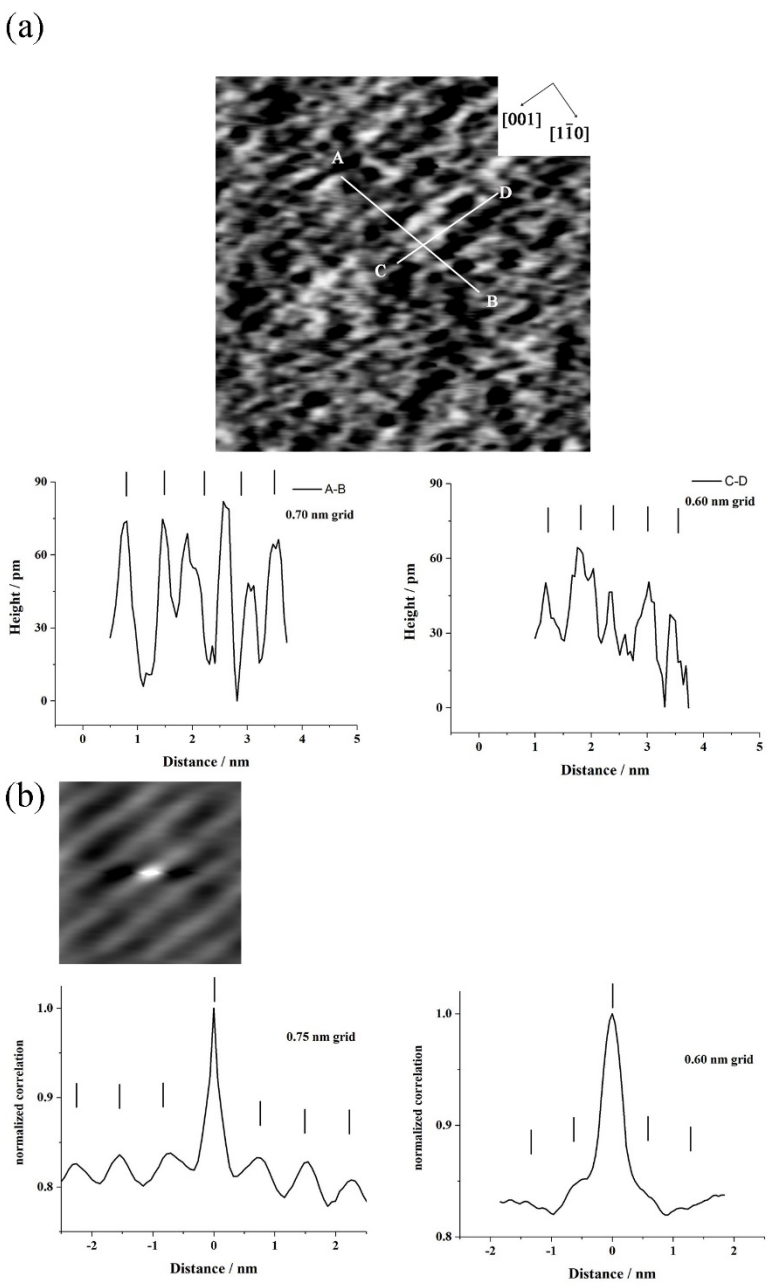


Fig. S4. Atom-scale topography of the rutile (110) wafers in the KCl solution of pH 11. A raw topographic image of 8 × 8 nm$^2$ was average-filtered as shown in (a). Cross sections along A–B and C–D are shown in the lower panels. Frequency-shift setpoint: +137 Hz. Acquisition time: 10 s per frame. A self-correlation of the topography was determined in a 3 × 3 nm$^2$ and inserted in the topography shown in (b). The correlation curves involving the origin and parallel to the [1$\bar{1}$0] and [001] directions are presented on the lower panels.

# Chapter 3

# Nb doped $TiO_2$(110) surface probed in water by FM-AFM

# 3.1 INTRODUCTION

In order to solve the energy problem, the photodegradation reaction of semiconductor photocatalysis has received great attention in the recent years. Doping metals in the host photocatalyst materials is an effective measure to increase the quantum efficiency [1-2]. Quantum efficiency of the lanthanide doped $NaTaO_3$ is about 50% at 270 nm [3]. A Rh-doped $SrTiO_3$ showed incident-photon-to-current efficiency of 0.18% at 420 nm. These researches showed dopants plays a key role in the improvement of photocatalyst performance.

However, the mechanism of metal doping is still not fully clear. For instance, it is not clear how the dopants are distributed around the surface, and how the dopants influence the interface of water and photocatalytic in the environment of photocatalytic decomposition of water. Solving these problems would help improve our understanding of doping and photocatalyst.

Niobium doping titanium dioxide showed improved photocatalyst [4-7] and gas sensors [8-13] performance. Nb can improve the photocatalytic activity because it can enhance the upward band bending thus promote the electron-hole division [6].

In Chapter 2, the author observed the $TiO_2$(110) surface in the water by FM-AFM. The interface structure of the water/$TiO_2$ has be unriddled. In Chapter 3, Nb doped $TiO_2$(110) was observed in air and water. Although the Nb doped $TiO_2$(110) surface changed after multiple annealing, but the step and terrace structure still be observed. The atomic resolution images showed atomic column on this surface. In addition, water-Nb doped $TiO_2$ interface was also imaged by FM-AFM.

## 3.2 EXPERIMENTAL SECTION

### 3.2.1 preparation

Mirror-polished, 0.86 at% Nb doped (110)-oriented wafer of rutile $TiO_2$ (Shinkosha) were annealed in a two-step procedure using a tube furnace. The wafers were first maintained at 1000 ℃ for 12 hours in a sapphire tube open to laboratory air. Annealing at the elevated temperature was efficient for developing wide (110) terraces. In the second step, the wafer was further annealed at 500 ℃ in a quartz tube filled with dry air, a mixture of $O_2$ and $N_2$ with a pressure ratio of 1:4. To recycle the wafer before each annealing step, the wafer was supersonic cleaned in Milli-Q water and acetone for 30 minutes each.

### 3.2.2 characterization

The AFM images which are observed in air are obtained by Amplitude-modulation atomic force microscope (SPM-9600, Shimadzu). The AFM images which are observed in the water are obtained by Frequency-modulation atomic force microscope in development (SPM-8100FM, Shimadzu). Images which are observed in water were analyzed with WSxM software [14].

Concentrations of doped Niobium on the surface were quantified relative to the number of Ti atoms by XPS (Ulvac-phi, PHI X-tool). X-ray source is Al Kα. The spectra were collected with the pass energy of 26 eV and the energy step of 0.1 eV. The spectra was calibrated by O 1s became 530.3 eV [15]. Element mapping was operated by SEM-eds (JSM-7100F, JED-2300, JEOL).

## 3.3 RESULTS AND DISSCUSSION

### 3.3.1 Nb doped $TiO_2$(110) after annealing

The 0.86 at% doped $TiO_2$(110) wafer without any treatment observed in air by AM-AFM was shown in Figures 1(a) and (b). In the larger scan range (Figure 1(a)), there are no particularly large ups and downs on this surface, while there are some dot like structure on this surface. The cross-section of A-B is shown in Figure 1(c). These dot like structures are 1 nm in height and 50 nm in diameter, which are traces left after surface grinding.

Figures 1(d) and (f) are the same wafer as Figures 1(a) and (b) after 1-time annealing observed in air by AM-AFM. In Figure 1(d), the wafer after annealing overall became flatter, but some new gaps appeared on the surface. The cross-section of A-B is shown in Figure 1(e). Between the flat terrace, these gaps are about 20 nm in depth and 1 nm in width. This surface is different from the non-doped $TiO_2$(110) surface as shown in Chapter 2. The non-doped $TiO_2$(110) surface after annealing only have step and terrace structure with no gap structure. Figure 1(f) showed the partially enlarged view of terrace structure. On the flat part, step and terrace structures can be observed in the same manner as the non-doped $TiO_2$(110) surface after annealing in Chapter 2.

Many of the atom doped $TiO_2$ surface showed spherical structure after annealing, such as Eu doped [16], gold doped [17], and Fe doped [18]. However, in the present experiment, the Nb doped $TiO_2$(110) surface showed a flat terrace after annealing. There are two reasons for the observation: first is that the Nb doped $TiO_2$(110) wafer is a polished wafer and the observed surface showed very high flatness in the initial state, second is that the author chose high temperature to anneal the wafer since Eu doped $TiO_2$ wafer showed flatter surface after annealing at higher temperature as reported by Prociow et al. [16]. In the present experiment, the Nb doped $TiO_2$ wafer annealed at 1273 K, and such temperature made the surface even smoother.

Figure 1(g) shows the same wafer as Figures 1(a) and (b) after 3-times annealing observed in air by AM-AFM. The same gap structure can be observed in this surface. On this surface, the number of gaps is significantly more than the surface of 1-time annealing. In Figure 1(h), the cross-section of A-B shows gaps that have about 10 nm depth and 0.5 nm width. It is also smaller than the gaps in the surface of 1-time

annealing. On the flat part, the step and terrace structures can be observed in Figure 1(i).

The difference between the surface of Nb doped $TiO_2$(110) and non-doped $TiO_2$(110) from the AFM images in air is the gaps. In Nb doped $TiO_2$(110) surface, as the number of annealing times increases, the number of gaps is also increase, and the reason behind the difference may be related to the Nb doping.

(a)

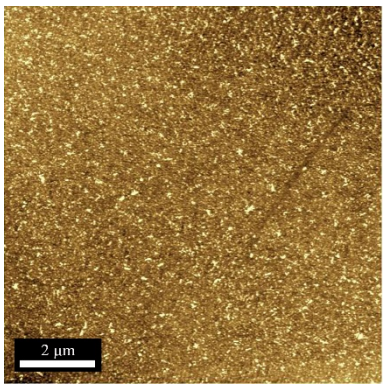


(b)

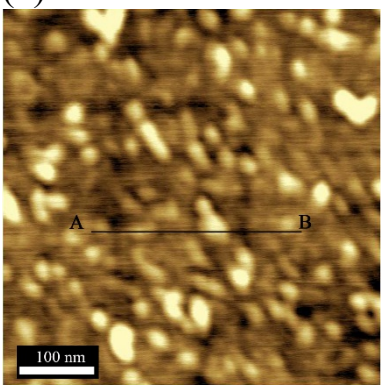


(c)

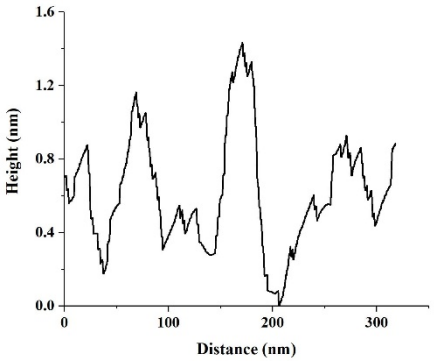


(d)

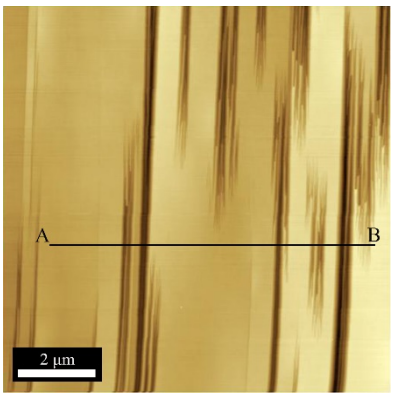


(e)

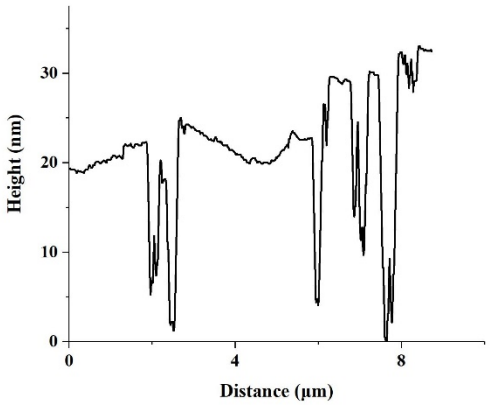

(f)

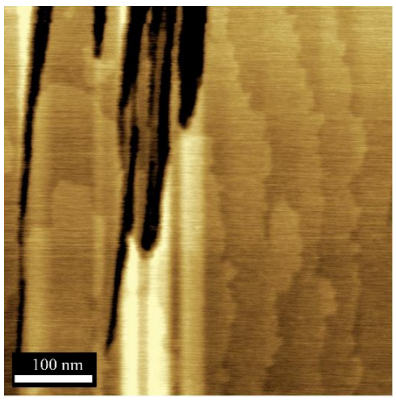


(g)

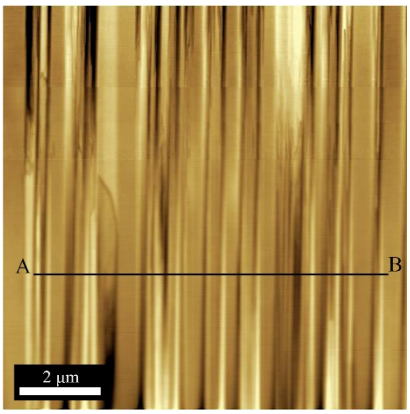


(h)

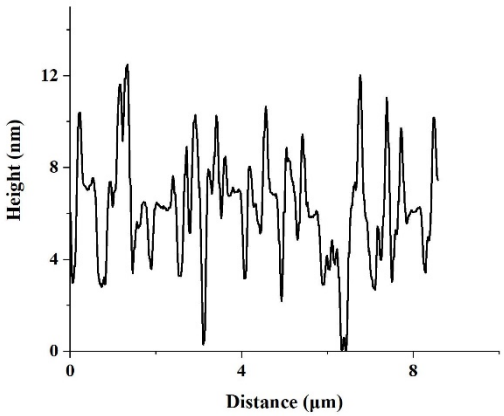


(i)

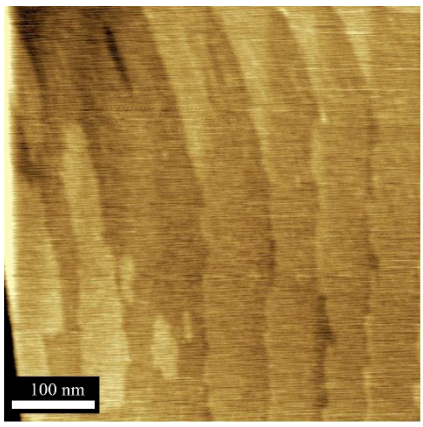


Fig. 1. (a) the AFM image of Nb 0.86 at% $TiO_2$(110) surface as received in air.(b) partially enlarged view of (a). (c) the cross-section along the line A-B in image(b). (d) the AFM image of Nb 0.86 at% $TiO_2$(110) surface after 1 time annealing in air.(e) the cross-section along the line A-B in image(b). (f) partially enlarged view of (d). (g) the

AFM image of Nb 0.86 at% $TiO_2$(110) surface after 3 times annealing in air.(h) the cross-section along the line AB in image (g). (i) partially enlarged view of (g).

Figure 2(a) shows the Nb 3b X-ray photoelectron spectroscopy of Nb-doped $TiO_2$(110) surface as-received and after 3-times annealing. The two Nb-doped surface both have two peaks at 210.1 eV and 207.5 eV. The two peaks are assigned to 3d3/2 and 3d5/2 states of Nb[19]. No peak shift between the as-received surface and 3-times annealing surface. Nb chemical price has not changed after annealing. After annealing, the peak intensity of Nb-doped $TiO_2$(110) is greatly improved.

Figure 2(b) shows the Ti 2p X-ray photoelectron spectroscopy of Nb-doped $TiO_2$(110) surface as received and after 3-times annealing. The as-received surface has peaks at 464.9 eV and 459.1 eV. The two peaks are assigned to 2p1/2 and 2p3/2 states of Ti [19]. In the as-received near-surface region, the atom ratios of the Nb /Ti is 1.2% calculation by Ti2p and Nb 3d peak intensity. In the 3-times annealing, the atom ratios of Nb /Ti is 13.3%. After 3-times annealing, the ratio of Nb is greatly increased in the near-surface region.

The SEM images are shown in Figure 3. In Figure 3(a), as-received surface showed a flat plane. A lot of dot like structures can be observed on the same surface by AFM. These dot like structures are only 1 nm in height and they are smaller than the ultimate resolution of SEM. Therefore, in the SEM image, no dot like structure can be observed. In Figures 3(b), (c) and (d), Nb, O, Ti mappings are shown. In Figure 3(e), the same gaps can be observed as the Figure 1(g) on 3-times annealing $TiO_2$(110) surface. But in the mapping of each element, the Nb, O, Ti still have their own distribution on the surface. There is no phenomenon of agglomeration due to the appearance of gaps. This showed that Nb atoms are evenly distributed on the top or bottom of the gaps.

(a)

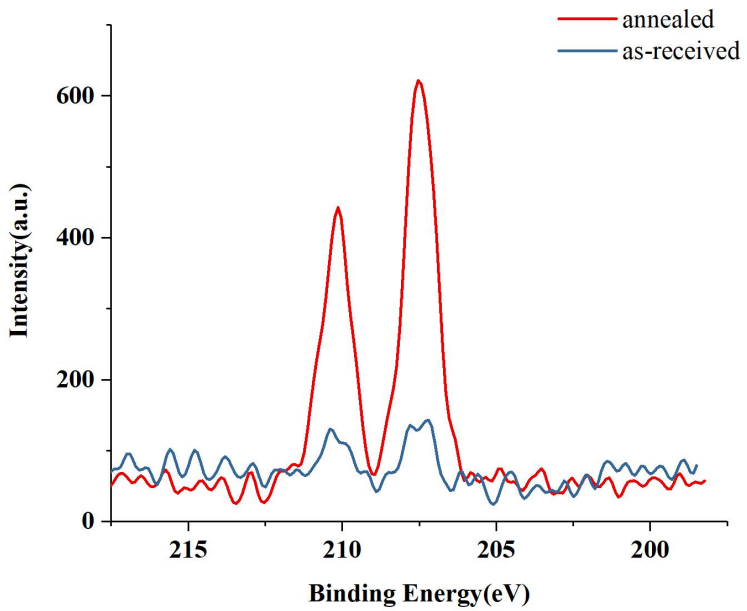


(b)

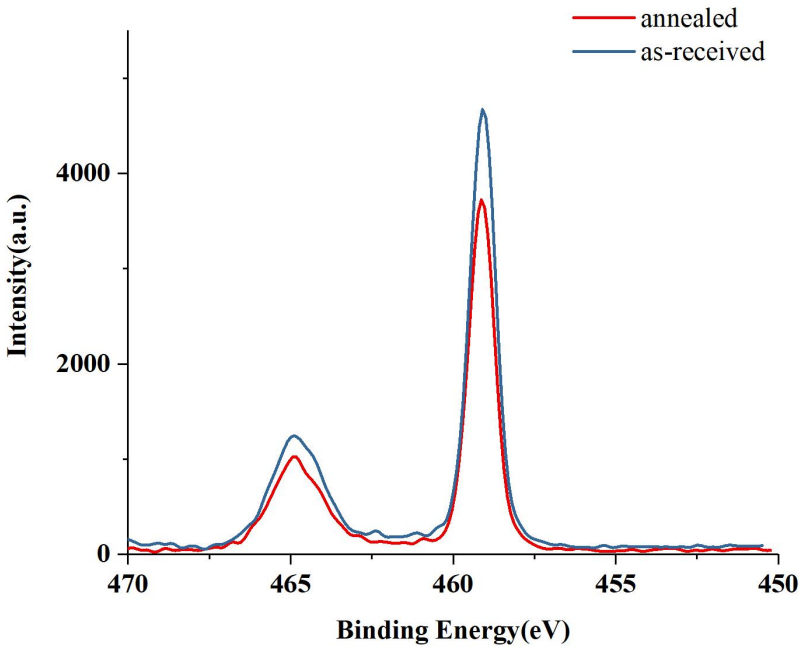


Fig. 2. (a) X-ray photoelectron spectra of 0.86 at% doped $TiO_2$(110) surface, red: as-received, blue: after 3 times annealing. (a) Nb-3d emission. (b) Ti-2p emission.

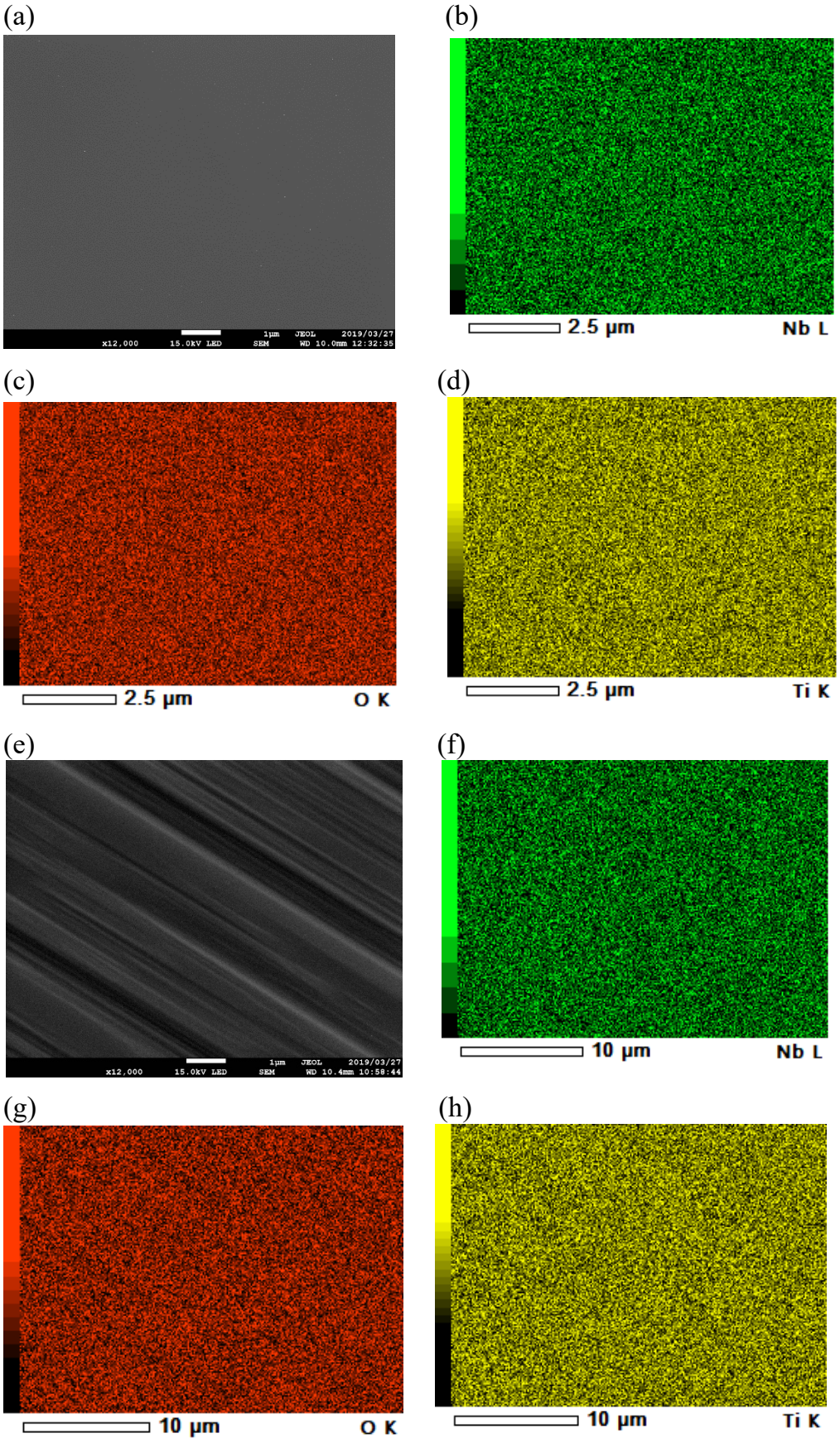


Fig. 3. (a) The scanning electron microscope image of as-received Nb doped

$TiO_2$(110) surface. EDS mapping of Nb (b), O (c),Ti (d) in as-received surface. (e) the scanning electron microscope image of 3 times annealing Nb doped $TiO_2$(110) surface. Eds mapping of Nb (f), O (g), Ti (h) in 3 times annealing surface.

Figure 4 showed a simple model of Nb doped $TiO_2$ (110) from as-received to 3 times annealing. The surface showed a relatively flat surface at as-received stage. After 1-time annealing, the deep and wide gaps can be observed on this surface. After 3 times annealing, the number of gaps increased substantially. The depth of the gap is also shallower.

An et al. [20] presented SEM images of Sr doped $NaTaO_3$ at different molar concentration. As the molarity of Sr increased, more folds appeared on the surface of $NaTaO_3$. The article explained that when Sr is doped into the bulk of $NaTaO_3$, the lattice mismatch was too strong to reserve in the shape of cubs. As a result, the folds grew on the surface of the particles to release mismatch energy. In the present experiment, as the molarity of Nb increased near the surface, the surface of $TiO_2$(110) showed more gaps. It is possible that the gaps are formed for the same reason as folds on Sr doped $NaTaO_3$. The increased of Nb molarity increased the lattice mismatch, leading to the appearance of gaps.

For the process of the formation of the gap, the author proposed two hypotheses as shown in Figure 5. The first hypothesis is that the bulk Nb come to near-surface region due to annealing, causing the unevenness on the surface. As shown in Figure 5 (a), although the first hypothesis can explain the status from as-received to 1-time annealing, the hypothesis cannot be used to explain the status from 1-time annealing to 3-times annealing, since it would be expected that the gap would become deeper and wider, and the number of gaps would be reduced. However, as shown in Figure 1(g), the Nb doped $TiO_2$(110) surface after 3-times annealing has many more gaps than the surface after 1-time annealing, and the gaps are also shallower and narrower. Therefore, the first hypothesis contradicts the actual result. The second hypothesis is that some Nb which

are in near-surface region gather together to create the gaps on the surface. As shown in Figure 5 (b), similar to the first hypothesis, although the second hypothesis can explain the status from as-received to 1-time annealing, but the hypothesis cannot be used to explain the status from 1-time annealing to 3-times annealing, since the gaps become shallower and narrower. To this end, both of the hypotheses cannot be used to explain the process of gaps appearance.

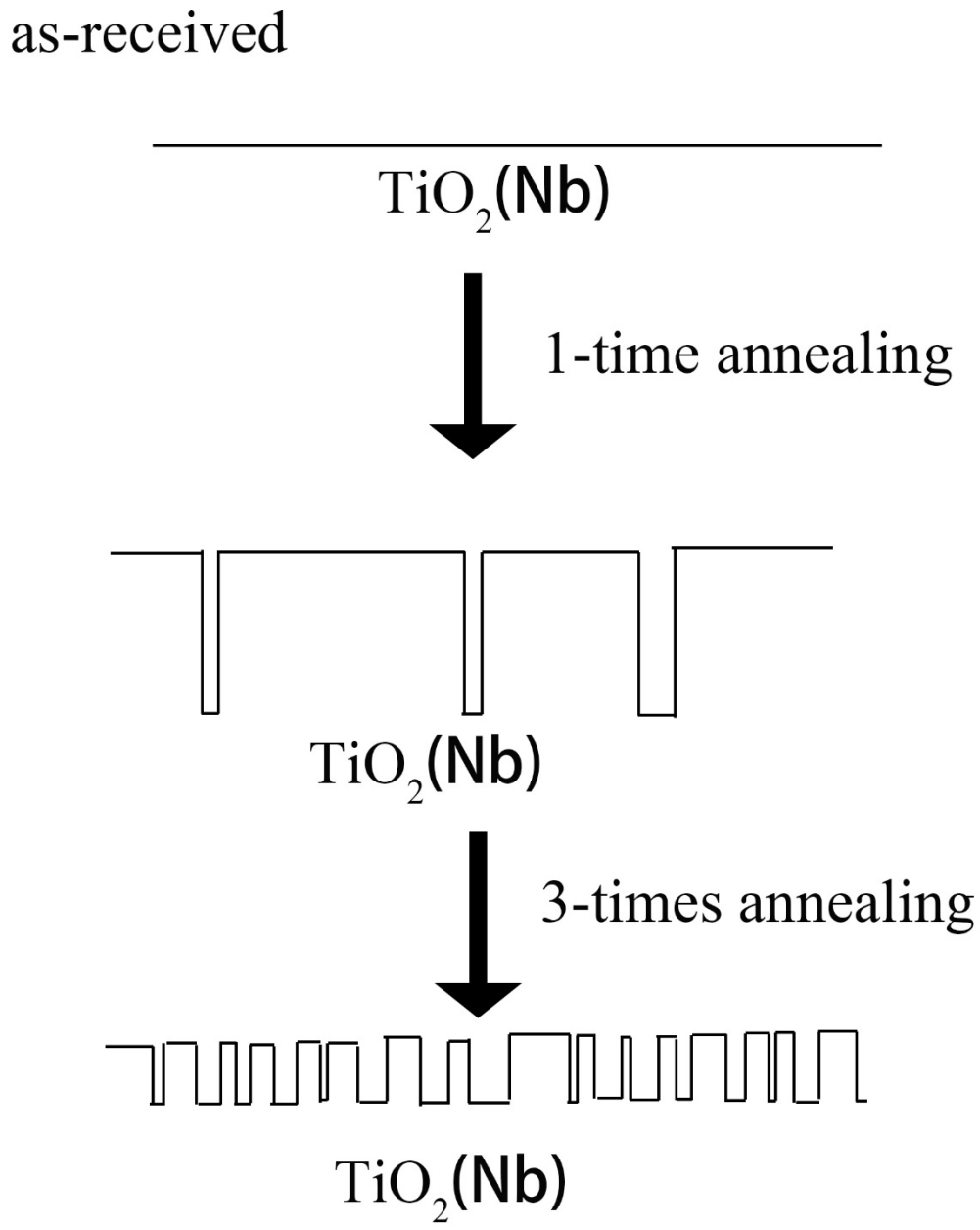


Fig. 4. The model of Nb doped $TiO_2$ from as-received to 3 times annealing.

(a)

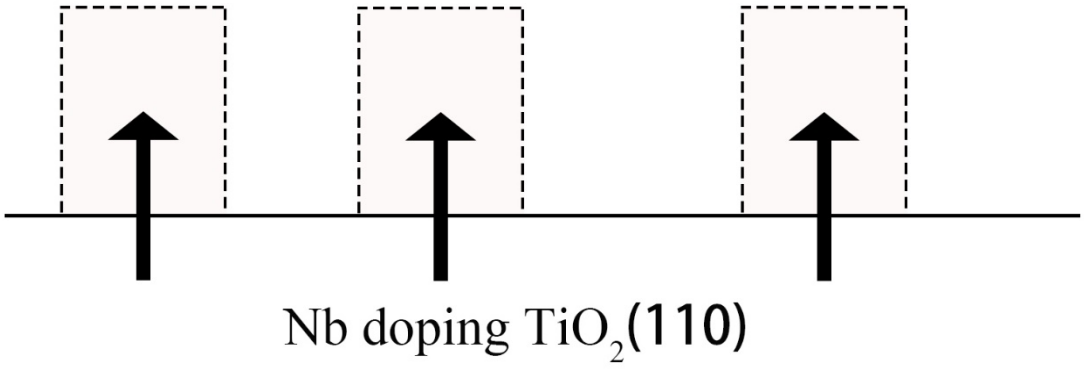


(b)

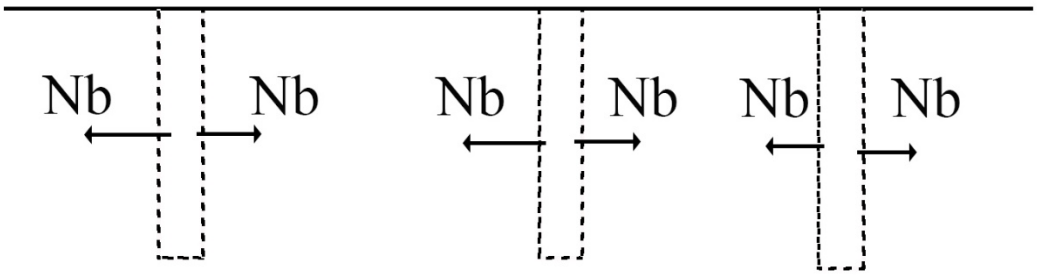


Fig. 5. two possibility of gaps appearance.

### 3.3.2 Nb doped $TiO_2$(110) surface observed in liquid

The Nb doped $TiO_2$(110) surface after 3-times annealing was observed in 0.1M KCl solution by FM-AFM. Figure 6(a) shows topographic images of positive $\Delta f$ setpoints, *i.e.* repulsive tip–surface force in the feedback regulation for tracing the topography. This surface showed sharp step and flat terrace structure in water. The step height was about 0.35 nm as depicted in the cross sections. The observed height corresponds to the single step of $TiO_2$(110) truncation of rutile as shown in Chapter 1. The shape of terrace is different from the surface of no doping surface annealing in air, while it is similar to the surface of no doping surface annealing in Ultra-high vacuum (UHV) [21]. After annealing, the Nb doped $TiO_2$(110) wafer maintains the black color as when initially received.

Atomic-resolution AFM image of the flat terrace in Figure 6 (a) is shown in Figure 6 (c). Along the [001] direction, bright rows are arranged on the terrace. The distance between the row columns was 0.65 nm as shown in the A-B cross-section. It is consistent with ×1 truncation of $TiO_2$(110) surface along the $[1\bar{1}0]$ direction. However, along the [001] direction, the distance between the rows on the columns was erratic, and the regularity of rows cannot be identified. In the present study, the AFM image of Nb doped $TiO_2$(110) surface was compared with the non-doped $TiO_2$(110) surface as shown in Chapter 2, wherein both surfaces showed bright rows representing bridge oxygen arranged on the terrace along the [001] direction.

Sasahara et al. annealed the 0.86 at% Nb doped $TiO_2$(110) in UHV and sputtered by $Ar^+$ [22], with the surface observed in UHV by STM. They observed the Nb atoms on the Ti columns. These Nb atoms were occasionally found in a concentrated manner. Some Nb atoms are adatom on the Ti columns, and some are substitutes for Ti cation. The Nb atoms which are substitutes for Ti cation are difficult to detect. The atomic radius of Ti and Nb are 140pm and 135 pm, respectively [23]. Since the two element's

atomic radius are very close, the height of Ti columns would not be dramatically changed even if Nb atoms are substituted with Ti atoms.

The height difference between the bridge oxygen and 5-fold Ti atom on non-doped $TiO_2$(110) surface is about 120 pm as shown in Chapter 2. Sasahara's research showed the Nb of adatoms is about 30 pm higher than substitute Nb atoms [22]. In Figure 6(e), the cross-section of C-D showed height difference between crest and trough is 80 pm, which is much higher than the height difference between Nb of adatoms and substitute Nb atoms, but less than the height difference between the bridge oxygen and 5-fold Ti atoms.

Furthermore, the Nb of adatoms may hidden between the bridge oxygen columns. This makes it difficult for AFM to detect them. It is the reason for why the AFM image of Nb doped $TiO_2$(110) surface cannot show any Nb atoms on the surface.

Nb atoms cannot be observed by the topography, since there is no obvious height difference. The Nb atom may also affect the distribution of water molecules on itself. Analyzing the hydration structure of Nb doped $TiO_2$(110) surface is one possible method to find the Nb atoms on the $TiO_2$(110) surface.

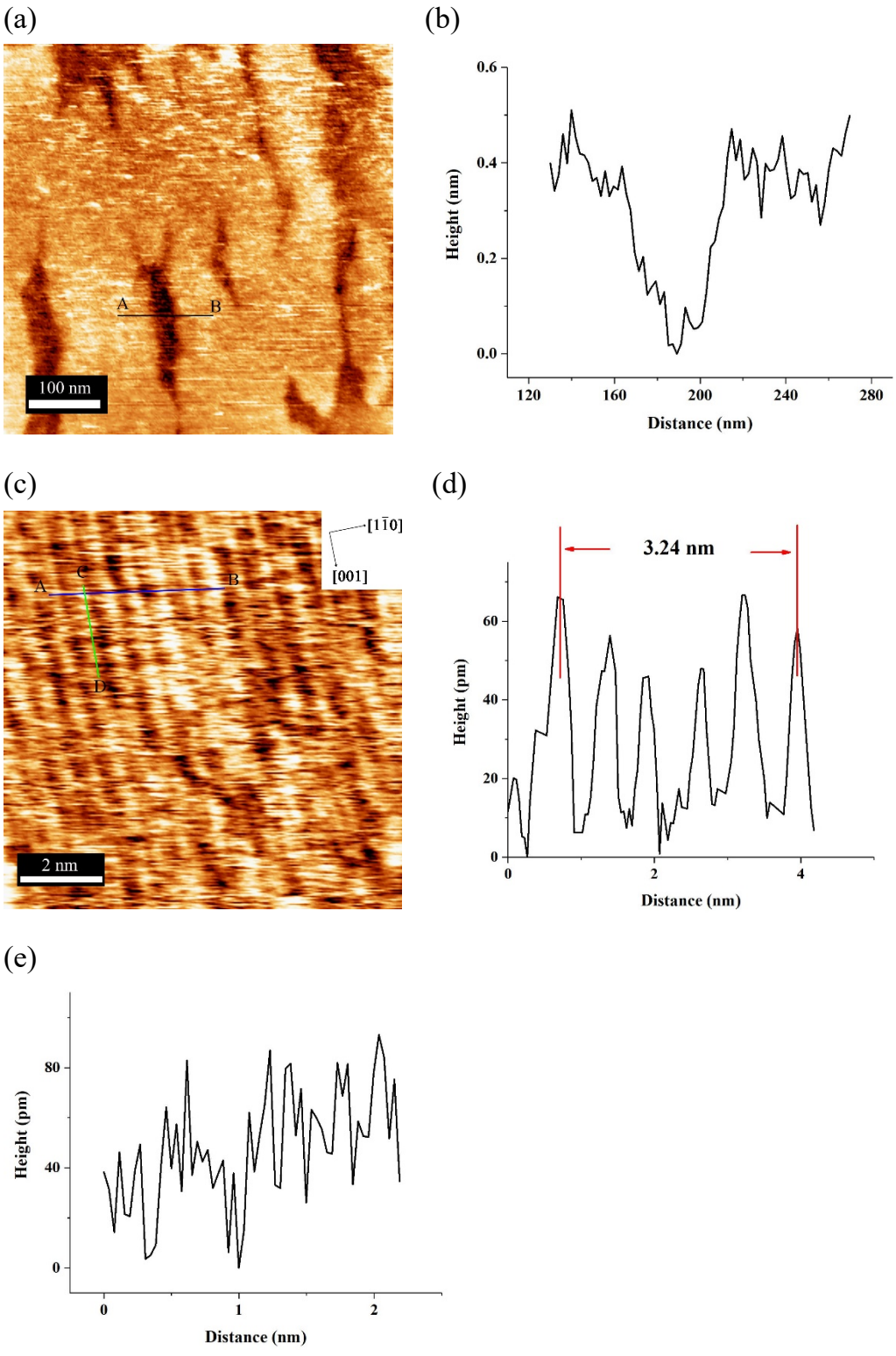


Fig. 6. (a) Terraces and single-height steps on the Nb doped rutile (110) surface. Frequency-shift ($\Delta f$) :+215 Hz (b) Cross sections along A–B in (a) , (c) the image of Nb doped $TiO_2$(110) measured in 0.1M KCl aqueous solution with FM-AFM. Frequency-shift ($\Delta f$)= +126 Hz.(d) Cross sections along A–B in (c), (d) Cross sections along C-D

in (c).

Figure 7 (a) showed $\Delta f$ maps obtained by measuring the variation of the frequency shift of cantilever, as a function of distance from the surface and lateral distance on the surface. The image shows 2D frequency shift variation, with black showing negative frequency shift and white showing positive frequency shift. On the Nb doped $TiO_2$(110) surface, at least 2 layers can be observed.

The force-distance curve after averaging between the red dotted line from 10 lines and calculated from $\Delta f$ curve using the Sader equation [24] is shown in Figure 7(b). Near the surface, force oscillations can be located at ~0.4 nm and ~0.7 nm from the surface. The distance between the two force oscillations is about 0.3 nm, which is consistent with the expected thickness of a water molecule layer [25-26], and is similar to the hydration structure of non-doped $TiO_2$(110) surface shown in Chapter 2. On the non-doped and doped surface, one water molecule layer can also be observed. In Chapter 2, the author explained that the hydration structure of layer 1 is the water molecule in the groove between the bridge oxygen. On the Nb doped structure, it is also possible that the water molecule was present in the groove between the bridge oxygen.

The hydration structures on different elements are different [27]. But in Figure 7(a), the hydration structure is similar to the non-doped $TiO_2$(110) surface shown in Chapter 2. The author cannot locate the Nb atoms based on the hydration structure, since there are two types of Nb atoms on the surface. The one is as the adatom in the 5-fold Ti columns. The other one is substitute for Ti cation. In both cases, the fluctuations on Ti columns cannot be observed. In Chapter 2, the author showed that the difference in surface atomic charge can lead to stronger hydration structure on $TiO_2$(110) surface. However, in this case, Nb is pentavalent and Ti is tetravalent. The difference in charge between the two elements is also small.

(a)

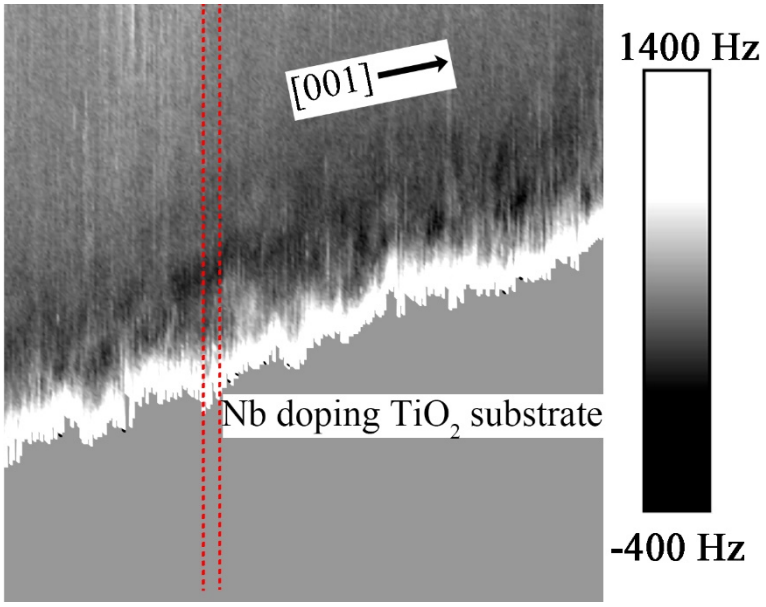


(b)

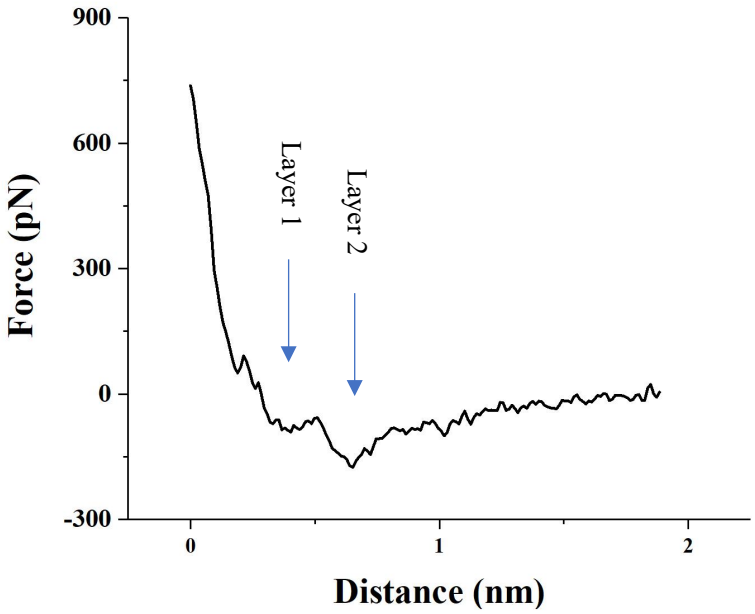


Fig. 7. (a) FM-AFM $\Delta f$ distribution observed above the Nb doped $TiO_2$ (110) surface after 3-times annealing in 0.1M KCl aqueous solution . (b) A force-distance curve of marked line in (a).

## 3.4 CONCLUSION

(1) The Nb doped $TiO_2$(110) wafer was annealed in air to obtain a relatively flat surface. Different from the non-doped $TiO_2$(110) after annealing, a gap structure appeared on the Nb doped $TiO_2$(110) surface. This structure increased with the number of annealing times as confirmed by SEM.

(2) The XPS data shows the amount of doping increases as the number of annealing increases near the surface. However, the distribution of Nb on the surface is still uniform as the as-received wafer.

(3) The author made two hypotheses about the phenomenon of gaps on Nb doped $TiO_2$(110) surface, but both of these hypotheses have their own flaws.

(4) The topography and hydration structure of the Nb doped $TiO_2$(110) surface observed in 0.1M KCl solution showed images similar to non-doped surface, and the location of Nb atoms on the $TiO_2$(110) surface is not identified through these two methods.

## 3.5 REFERENCE


1. Ishihara T, Nishiguchi H, Fukamachi K,Tkkita Y. Effects of acceptor doping to KTaO3 on photocatalytic decomposition of pure $H_2O$. *The Journal of Physical Chemistry B*, 1999, 103, 1-3.

2. Mitsui C, Nishiguchi H, Fukamachi K, Ishihara T, Takita Y. Photocatalytic decomposition of pure water over NiO supported on KTa (M) $O_3$ (M= Ti4+, Hf4+, Zr4+) perovskite oxide. *Chemistry Letters*, 1999, 28, 1327-1328.

3. Kudo A, Kato H. Effect of lanthanide-doping into $NaTaO_3$ photocatalysts for efficient water splitting. *Chemical Physics Letters*, 2000, 331, 373-377.

4. Trenczek-Zając A, Radecka M, Rekas M. Photoelectrochemical properties of Nb-doped titanium dioxide. *Physica B: Condensed Matter*, 2007, 399, 55-59.

5. Castro A L, Nunes M R, Carvalho M D, Ferreira L P, Jumas J -C, Costa F M, Florencio M H. Doped titanium dioxide nanocrystalline powders with high photocatalytic activity. *Journal of Solid State Chemistry*, 2009, 182, 1838-1845.

6. Karakitsou K E, Verykios X E. Effects of altervalent cation doping of titania on its performance as a photocatalyst for water cleavage. *The Journal of Physical Chemistry*, 1993, 97, 1184-1189.

7. Michalow K A, Flak D, Heel A, Parlinska-Wojtan M, Rekas M, Graule T. Effect of Nb doping on structural, optical and photocatalytic properties of flame-made $TiO_2$ nanopowder. *Environmental Science and Pollution Research*, 2012, 19, 3696-3708.

8. Teleki A, Bjelobrk N, Pratsinis S E. Flame-made Nb-and Cu-doped $TiO_2$ sensors for CO and ethanol. *Sensors and Actuators B*: Chemical, 2008, 130, 449-457.

9. Ruiz A, Dezanneau G, Arbiol J, Cornet A, Morant J.R. Study of the influence of Nb content and sintering temperature on $TiO_2$ sensing films. *Thin Solid Films*, 2003, 436, 90-94.

10. Nechita V, Schoonman J, Musat V. Ethanol and methanol sensing characteristics of

Nb-doped TiO2 porous thin films. *Physica Status Solidi (a)*, 2012, 209, 153-159.

11. Anukunprasert T, Saiwan C, Traversa E. The development of gas sensor for carbon monoxide monitoring using nanostructure of Nb–$TiO_2$. *Science and Technology of Advanced Materials*, 2005, 6, 359-363.

12. Sharma R K, Bhatnagar M C. Improvement of the oxygen gas sensitivity in doped $TiO_2$ thick films. *Sensors and Actuators B*: *Chemical*, 1999, 56, 215-219.

13. Bonini N, Carotta M C, Chiorino A, Guidi V, Malagu C, Martinelli G, Paglialonga L, Sacerdoti M. Doping of a nanostructured titania thick film: structural and electrical investigations. *Sensors and Actuators B*: *Chemical*, 2000, 68, 274-280.

14. Horcas I, Fernández R, Gomez-Rodriguez J M, Colchero J, Gomez-Herrero J, Baro A.M. WSXM: a software for scanning probe microscopy and a tool for nanotechnology. *Review of Scientific Instruments*, 2007, 78, 013705.

15. McCafferty E, Wightman J P. An X-ray photoelectron spectroscopy sputter profile study of the native air-formed oxide film on titanium. *Applied Surface Science*, 1999, 143, 92-100.

16. Prociow E L, Domaradzki J, Podhorodecki A, Borkowaska A, Kaczmarek D, Misiewicz J. Photoluminescence of Eu-doped $TiO_2$ thin films prepared by low pressure hot target magnetron sputtering. *Thin Solid Films*, 2007, 515, 6344-6346.

17. Buso D, Pacifico J, Martucci A, Mulvaney P. Gold-nanoparticle-doped $TiO_2$ semiconductor thin films: optical characterization. *Advanced Functional Materials*, 2007, 17, 347-354.

18. Bally A R, Korobeinikova E N, Schmid P E, Levy F, Bussy F. Structural and electrical properties of Fe-doped thin films. *Journal of Physics D: Applied Physics*, 1998, 31, 1149.

19. Moulder J F. Handbook of X-ray photoelectron spectroscopy. *Physical Electronics*, 1995, 230-232.

20. An L, Park Y, Sohn Y, Onishi H. Effect of Etching on Electron–Hole Recombination in Sr-Doped NaTaO3 Photocatalysts. *The Journal of Physical Chemistry C*, 2015, 119, 28440-28447.

21. Li M, Hebenstreit W, Gross L, Diebold U, Henderson M.A, Jennison D.R, Schultz P.A, Sears M.P. Oxygen-induced restructuring of the $TiO_2$ (110) surface: a comprehensive study. *Surface Science*, 1999, 437, 173-190.

22. Sasahara A, Tomitori M. XPS and STM study of Nb-doped $TiO_2$ (110)-(1× 1) surfaces. *The Journal of Physical Chemistry C*, 2013, 117, 17680-17686.

23. Slater J C. Atomic radii in crystals. *The Journal of Chemical Physics*, 1964, 41, 3199-3204.

24. Sader J E, Jarvis S P. Accurate formulas for interaction force and energy in frequency modulation force spectroscopy. *Applied Physics Letters*, 2004, 84, 1801-1803.

25. Fukuma T. Water distribution at solid/liquid interfaces visualized by frequency modulation atomic force microscopy. *Science and Technology of Advanced Materials*, 2010, 11, 033003.

26. Fukuma T, Reischl B, Kobayashi N, Spijker P, Canova F.F, Miyazawa K, Foster A.D. Mechanism of atomic force microscopy imaging of three-dimensional hydration structures at a solid-liquid interface. *Physical Review B*, 2015, 92, 155412.

27. Ito F, Kobayashi K, Spijker P, Zivanovic L, Umeda K, Nurmi T, Holmberg N, Laasonen K, Foster A.S, Yamada H. Molecular resolution of the water interface at an alkali halide with terraces and steps. *The Journal of Physical Chemistry C*, 2016, 120, 19714-19722.

# Chapter 4

# $TiO_2$(110) surface probed in 1-hexanol by FM-AFM

# 4.1 INTRODUCTION

Titanium dioxide ($TiO_2$) is widely used as various types of catalysts, such as photocatalyst [1-3] or general catalyst [4]. When titanium dioxide is used as a catalyst, the target is generally organic solvent. Titanium dioxide based photocatalyst has been used for degradation of organic matter [5-8], and this type of photocatalyst can disintegrate common organic solvents such as ketones [5], alcohols [6], halogenated hydrocarbons [7] and aromatic compounds [8]. In view of its uses, titanium dioxide based photocatalyst is considered as an effective means to remove air and water pollution.

Traditional amine production method uses toxic substances such as nitrile, carboxylic acid and carbonyl compounds, which produce salt residues [9]. A new method for amine production involves the use of titanium dioxide based catalysts to react aliphatic alcohol with ammonia to form amines [10]. This method has advantages over the traditional method as it is more environmental friendly since the by-product is only water, and is more accessible due to the use of aliphatic alcohol reactants.

To study the catalytic reactions on the titanium dioxide, the information at the solid-liquid interface is very important, since the information can help to better understand the reactions at the interface. For titanium dioxide, the interface between water and titanium dioxide was explained in Chapter 2, and there are also further studies using SFG [11] and X-ray diffraction [12] at this interface. However, there are only a few studies on the interface between organic solution and titanium dioxide. A new method named Frequency modulation atomic force microscope (FM-AFM) is used to study the liquid-solid interface [13].

In Chapter 2, the author used FM-AFM to capture the high-resolution images in organic solution on the titanium dioxide (110) surface. The author found that the observed surface with a step-terrace morphology maintains a stable structure in organic solution. The high spatial and force resolutions of FM-AFM have enabled the visualization of the two-dimensional images of hydration layers at the interface of organic solution and titanium dioxide. A structure similar to lipid bilayer could be observed at this interface.

# 4.2 EXPERIMENT

## 4.2.1 preparation

Mirror-polished, (110)-oriented wafers of rutile $TiO_2$ (Shinkosha, STEP type) were annealed in a two-step procedure using a tube furnace, in accordance with earlier report [14]. Isolating the wafer from $SiO_2$-containing devices heated at 1000 ℃ or higher was essential to avoid silicon contamination on the annealed surface, which was observed when using XPS. The wafers were first maintained at 1000 ℃ for 12 hours in a sapphire tube open to laboratory air. Annealing at the elevated temperature was efficient for developing wide (110) terraces. In the second step, the wafers were further annealed at 500 ℃ in a quartz tube filled with dry air, a mixture of $O_2$ and $N_2$ with a pressure ratio of 1:4. The absence of water vapor in the annealing environment was the key to finish a well-ordered $TiO_2$(110) truncation [14]. It was difficult to make the heated sapphire tube airtight and hence the quartz tube was used in the second step. We checked and confirmed that the wafer surface was free from Si contamination annealed in the quartz tube maintained at 500 ℃.

The annealed $TiO_2$ wafer, 10 mm square and 0.5 mm thick, was fixed on a fluorocarbon polymer disk. A droplet of imaging liquid, 1-hexanol solution (wako, >99%), was placed on the wafer, and it is not to be in contact with the disk. Contamination on the disk surface, if any, could not be transferred to the wafers surface through the liquid. The cantilever assembly was placed on top covered with a glass slip (Matsunami Glass). The slip was irradiated with a Hg–Xe lamp (San-ei Electric, UVS-204S) for 90 min to remove possible organic contamination from its surface prior to assembling. All the AFM experiments were performed at 27 ℃.

### 4.2.2 Characterization

Frequency-modulation detection of force on the probing tip was performed with a SPM-8100FM microscope in development (Shimadzu). For topographic imaging of the wafer, resonance oscillation of a silicon cantilever (Nanoworld, PPP-NCHAuD) was mechanically excited with a piezo-actuator. The nominal spring constant of the cantilevers was 40 N $m^{-1}$. The resonance frequency in the imaging solutions was 120–150 kHz with the quality factor of resonance ($Q$) around 4. A typical spectrum of thermally excited cantilever oscillation is shown in Figure 1. The oscillation amplitude was regulated at a preset peak-to-peak amplitude ($A$), typically of 1.5 nm. When a conservative force was loaded on the tip, the resonance frequency of cantilever oscillation ($\Delta f$) shifted accordingly. The topography of the wafer was traced with regulation of the tip–surface distance by keeping the frequency shift ($\Delta f$) at a prefixed setpoint. Observed images were analyzed with WSxM software [15].

In addition to topographic imaging, the mechanical response of the solution was probed and mapped on the planes that are perpendicular to the solution–wafer interface. The oscillating cantilever was scanned vertically from the bulk solution to the wafer. The frequency shift as a function of the vertical coordinate was recorded to obtain one $\Delta f$–distance curve. The vertical scan aborted when $\Delta f$ reached a predetermined threshold to prevent extensive tip-to-wafer contact. The cantilever was then retracted into the solution by 5.3 nm. We repeatedly acquired 256 vertical scans along a 5.3 nm long lateral coordinate. One $\Delta f$ map was constructed with acquisition time of 20–30 s.

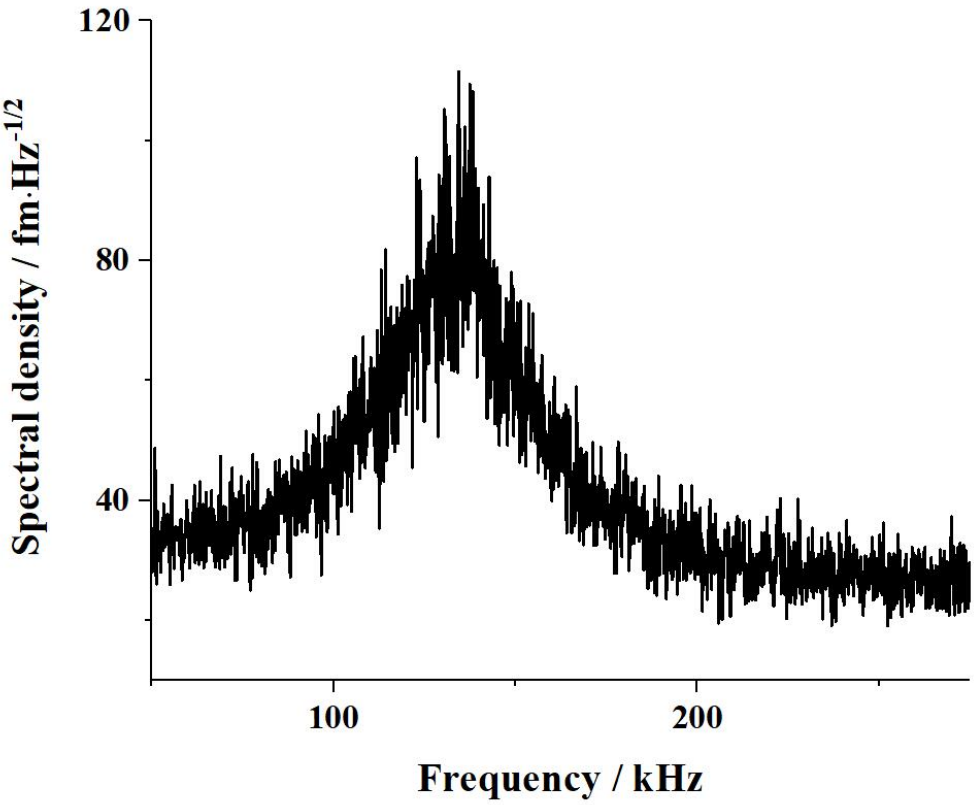


Fig. 1. A typical spectrum of thermally excited cantilever oscillation in the 1-hexanol.

## 4.3 RESULTS AND DISCUSSION

### 4.3.1 Topography

The annealed $TiO_2$(110) wafer presented terraces and steps in the 1-hexanol solution. Figure 2 showed topographic images observed with the positive $\Delta f$ setpoints. The terraces showed 100 nm or large in width, which is the same as the terraces of Chapter 2 observed in KCl solution. The step height was 0.35 nm as depicted in the cross sections (Figure 2(b)). The observed heights are consistent with the minimum step height predicted in the (110) truncation of rutile. This surface observed in the 1-hexanol is similar with the situation observed in the KCl solution. The annealed $TiO_2$(110) surface shows stabilized condition in KCl solution and 1-hexanol. Uetsuka et al. [16] found 10-nm scale inlet-shaped steps on rutile (110) wafers immersed in neutral water or aqueous ammonia as the sign of etching, but the same was not observed when wafer is immersed in methanol and benzene. In the present experiment, the wafer was observed in 1-hexanol, which is similar to methanol, and therefore no sign of etching is observed on the present wafer.

In Chapter 2, the (1×1) ordered particles were observed on the wafer made with the same method in KCl solution at pH 6. At this nearly isoelectric interface, the (1×1)-ordered particles are assumed to be the bridging oxygen anions. But in Figure 2(c), no atomic structure on the flat terrace can be observed on the wafer in 1-hexanol solution, and the surface only showed some undulations with a height of about 100 pm. One possible explanation is that the AFM resolution was not enough to detect the 0.65 × 0.32 nm distance in the 1-hexnaol solution. In Chapter 2, the same type of silicon cantilevers were resonantly oscillated at 130-150 kHz with quality factor(Q) of 10 in KCl solution. In the present experiment, the silicon cantilevers were oscillated at 120-150 kHz with Q of 4 in 1-hexanol solution. The quality factor in 1-hexanol solution was smaller than that in KCl solution, which may lead to higher resolution in KCl solution than in 1-hexanol solution, and this may be the reason why atomic resolution of wafer

could not be observed in 1-hexanol solution.

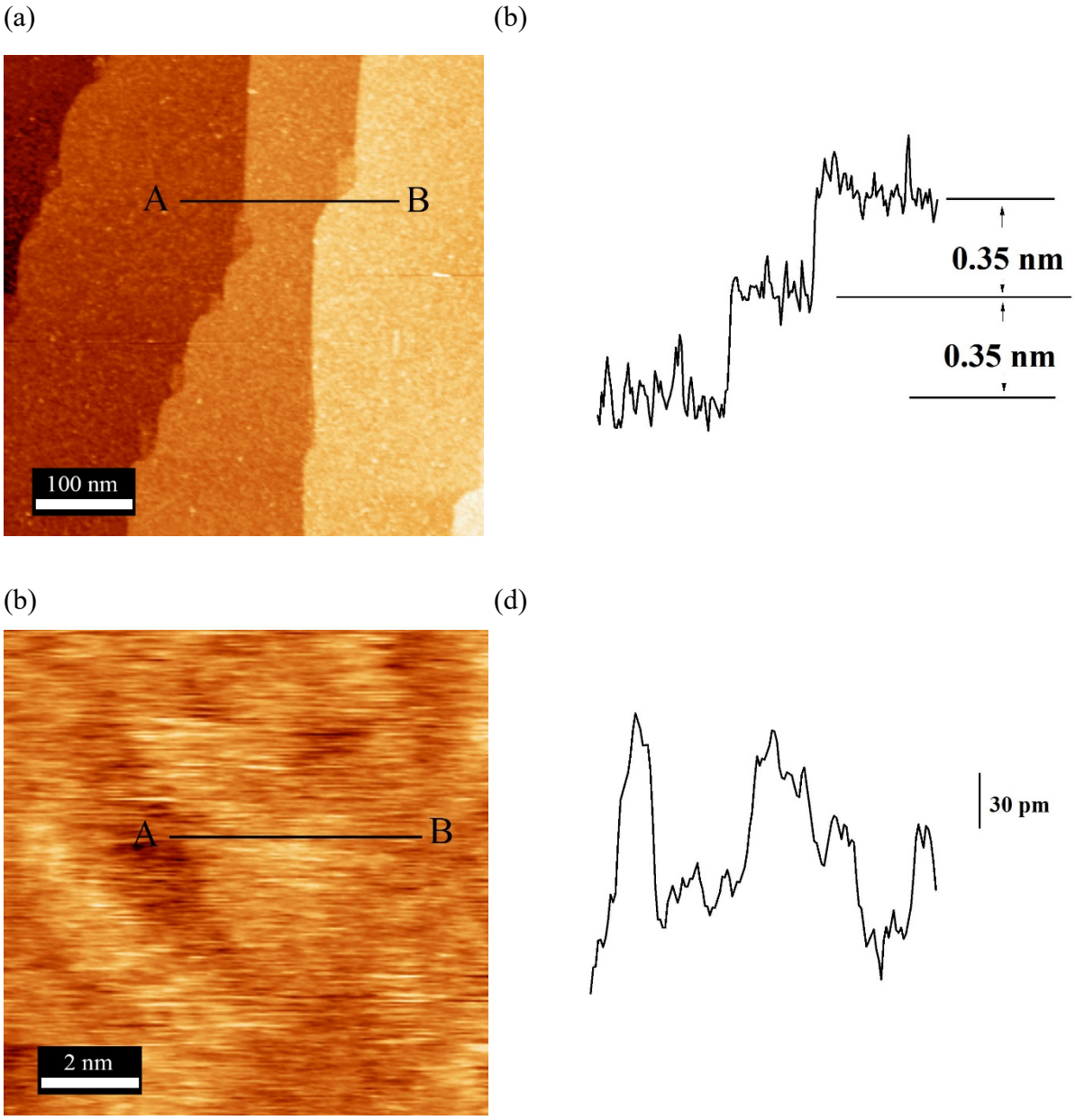


Fig. 2. (a) Terraces and single-height steps on the rutile (110) wafers in 1-hexanol.(b) Cross sections along A–B line is shown in the right panel (a). (c) topography on the terrace of $TiO_2$(110). (d) Cross sections along A–B line is shown in the right panel (c). Cantilever oscillation amplitude (A): (a)1.5 nm. (b)1.2 nm. Frequency-shift ($\Delta f$) setpoint: (a) +124, (b) +272 Hz.

## 4.3.2 Hydration structure

The 1-hexanol-$TiO_2$(110) interface was scanned by FM-AFM. Figure 3(a) showed a cross-sectional *Δf* distribution parallel to the [$1\bar{1}0$] direction. The envelope of the brightest region at the bottom showed the surface topography. Over the surface of $TiO_2$ finite *Δf* depressions appeared as two dark layers. The 5 lines average *Δf*-distance curve between two red line are shown in Figure 4(b). On this curve, two peaks can be observed, matching the two dark layers above the surface. The distance between the two peaks is about 1.8 nm. Figure 3 (c) shows the force-distance curve calculated from the *Δf* curve (Figure 3(b)) using the Sader equation [17]. The same wafer with different cantilever presented a repetition distance of 1.8 nm in its *Δf*-distance curve, as shown in FigureS1 and FigureS2.

(a)

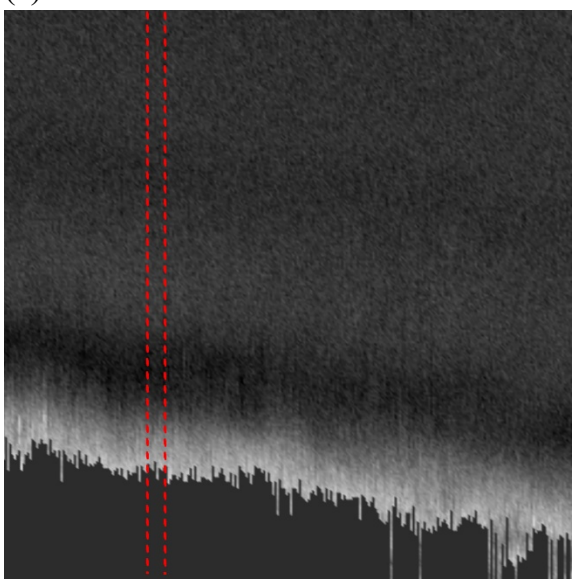

(b)

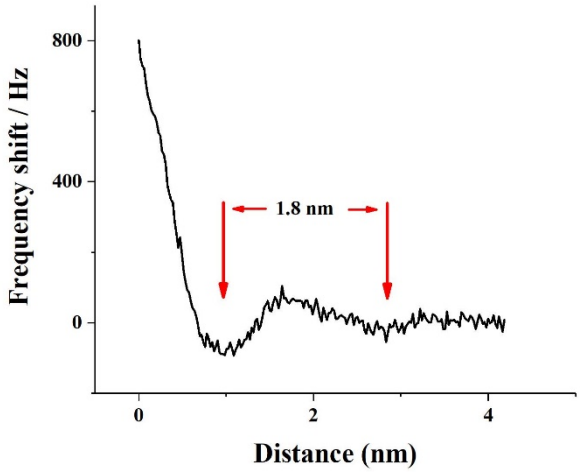

(c)

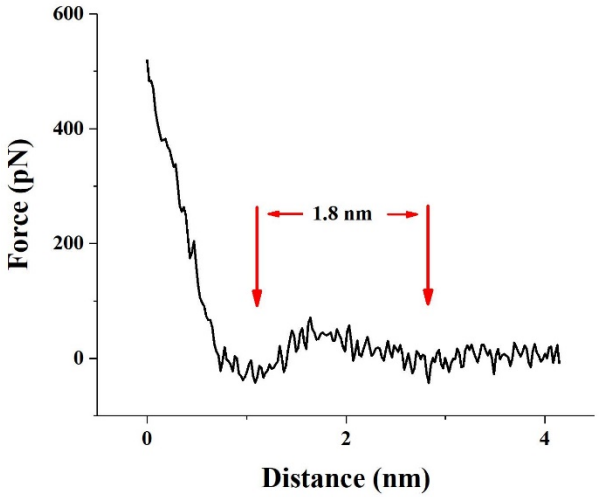


Fig. 3. (a) FM-AFM $\Delta f$ distribution observed above the $TiO_2$ (110) surface in 1-hexanol solution parallel to the [$1\bar{1}0$] direction. (b) A 5 lines average $\Delta f$ -distance curve of marked line in Fig(a). (c) A force-distance curve calculated from $\Delta f$ -distance curve.

The length of 1-hexanol could be calculated using the following data [18]. C-C bond distance is 150 pm, C-H bound distance is 110 pm, C-O bound distance is 1.43 pm, O-H bound distance is 0.97 pm. Bond angle between two C-C bond is 109.5°. Bound angle between C-C and C-H is 109.5°. Bound angle between C-C and C-O is 109.5°. Bound angle between C-O and C-H is 108.9°. The length of 1-hexanol calculated by the author is 913 pm. The model of 1-hexanol is shown in Figure 4.

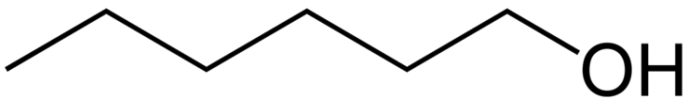


Fig. 4. The structure of 1-hexanol.

The interface between water and $TiO_2$(110) surface has already been discussed in Chapter 2. Near the isoelectric point, hydrogen-bonded water dimers are trapped on the five-fold coordinated Ti cations [19]. Among water trapped on the five-fold coordinated Ti cations, at least one water layer that is regularly arranged by hydrogen bonding was detected by SFG [20]. However, compared to water and $TiO_2$(110), the situation is different for the interface between organic solution and $TiO_2$ surface.

To the author's knowledge, no theoretical study of interface between 1-hexanol and $TiO_2$ surface has been published, but there have been a number of experimental investigations on the organic solution and $TiO_2$ surface system. A typical situation of organic molecule on the $TiO_2$(110) surface is that the organic molecule deprotonates to carboxylate, and the carboxylate could bond with the five-fold coordinated Ti cations. Trimethyl acetic acid is a typical example of the carboxylate, it deprotonates to form trimethyl acetate and hydroxide groups, and the two oxygen atoms of trimethyl acetate can bound with two five-fold coordinated Ti cations [21]. A simulation of methanol on $TiO_2$(110) was presented by S.P. Bates et al., which showed two types of methanol adsorption on $TiO_2$(110) surface [22]. One is the scission of the O-H bonds, in which O atoms are absorbed on five-fold coordinated Ti cations. The other one is the scission of the C-O bonds, in which the $CH_3^+$ are bonded with bridging oxygen, and the $OH^-$ is bonded with the five-fold coordinated Ti cations. For the latter situation, the molecules only adsorb on the $TiO_2$(110) surface when they are dissolved in the solvent or are gaseous, therefore the bond is easier to scissile so that the molecules are adsorbed on the $TiO_2$ surface. However, in the present experiment, 1-hexanol solution is in contact with $TiO_2$(110) surface in a pure liquid state. In this state, the self-ionization of 1-hexanol occurs rarely, therefore the concept of explaining the absorption of molecules on $TiO_2$ surface based on the methanol example as explained above is not applicable for the present experiment.

Another way of organic molecule absorption on metal oxide was presented by Pasarin et al. [23], in which a 2 nm thick film of liquid ethanol was deposited on calcite (104) surface and characterized with X-ray reflectivity. Low-density liquid layer of 0.09 nm thickness was detected at 0.6 nm above the surface. In this layer, the density of ethanol is half of the ordinary liquid ethanol. Pasarin et al. also presented an ordered monolayer of ethanol with the alkyl chain perpendicular to the surface by molecular dynamics simulations. The ethanol molecule is absorbed on the Ca cation, and the oxygen in

ethanol coordinate to the Ca cation. 2-propanol also showed the same structure on the Calcite (104) as evidenced by FM-AFM [24]. In addition, many liquid alcohols such as methanol, ethanol, hexanol were perpendicular to the mica as evidenced by the 1D force curves obtained by using AFM [25-27]. In the present experiment, 1-hexanol is also perpendicular to the $TiO_2$(110) in the same manner as hexanol on the mica. The hydroxy group coordinates the five-fold coordinated Ti cations on the $TiO_2$(110) surface. The thickness of 1-hexnol on $TiO_2$(110) as shown in Figure 3 (a) is about 1.8 nm, which is double the length of 1-hexanol molecule. First layer of 1-hexanol is adsorbed vertically on the $TiO_2$(110) surface through coordination of the five-fold coordinated Ti cations with the hydroxy group. At the second layer of 1-hexanol, the alkyl is facing the alkyl in the first layer of 1-hexanol. In addition, the hydroxy group is facing outward in the bilayer structure. In this situation, the 1-hexanol layer formed was most stable from the view of thermodynamics, in a similar manner as the phospholipid bilayer. The structure of 1-hexanol on the $TiO_2$(110) surface is shown in Figure5.

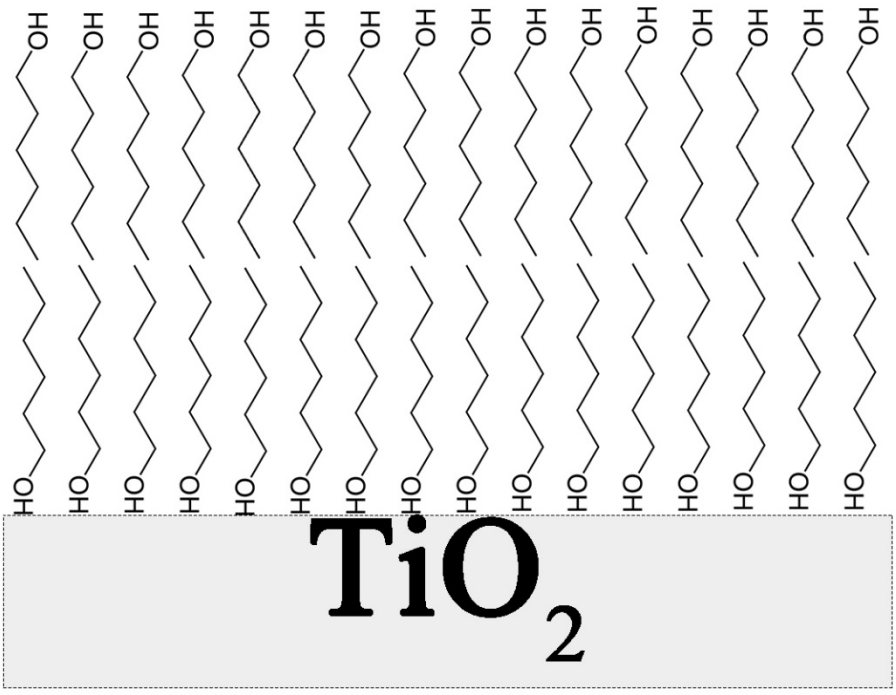


Fig. 5. The structure of 1-hexanol on the $TiO_2$(110) surface.

## 4.4 CONCLUSION

(1) In summary, frequency modulation atomic force microscope was applied to study the interface of 1-hexanol and $TiO_2$(110) surface. The $TiO_2$(110) surface showed sharp step and flat terrace structure in 1-hexanol. However, the cantilever's quality factor in 1-hexanol was only half of it when in water. The author could not get atomic resolution images in 1-hexanol.

(2) Above the $TiO_2$(110) surface, one layer of 1-hexanol could be observed. Two molecular layers are arranged vertically and formed as one layer on the $TiO_2$(110) surface. In the lower 1-hexanol molecule, hydroxy group coordinated with the five-fold coordinated Ti cations on the TiO2(110) surface. In the upper 1-hexanol molecule, hydroxy group was facing outward to the bulk 1-hexanol. The structure of the 1-hexanol layer was similar to that of the phospholipid bilayer.

(3) The information may improve our knowledge of the interface between organic solution and $TiO_2$ crystal, and could promote the development of $TiO_2$ catalyst.

## 4.5 REFERENCE


1. Ohno T, Mitsui T, Matsumura M. Photo catalytic activity of S-doped TiO2 photocatalyst under visible light. *Chemistry Letters*, 2003, 32, 364-365.

2. Iwasaki M, Hara M, Kawada H, Tada H, Ito S. Cobalt ion-doped $TiO_2$ photocatalyst response to visible light. *Journal of Colloid and Interface Science*, 2000, 224, 202-204.

3. Ohko Y, Ando I, Niwa C, Tatsuma T, Yamamura T, Nakashima T, Kubota Y, Fujishima K. Degradation of bisphenol A in water by $TiO_2$ photocatalyst. *Environmental Science & Technology*, 2001, 35, 2365-2368.

4. Ball M R, Wesley T S, Rivera-Dones K R, Huber G W, Dumesic J A. Amination of 1-hexanol on bimetallic AuPd/$TiO_2$ catalysts. *Green Chemistry*, 2018, 20, 4695-4709.

5. Coronado J M, Zorn M E, Tejedor-Tejedor I, Anderson M A. Photocatalytic oxidation of ketones in the gas phase over $TiO_2$ thin films: a kinetic study on the influence of water vapor. *Applied Catalysis B: Environmental*, 2003, 43, 329-344.

6. Wang M, Guo D, Li H. High activity of novel Pd/TiO2 nanotube catalysts for methanol electro-oxidation. *Journal of Solid State Chemistry*, 2005, 178, 1996-2000.

7. Bahnemann D, Bockelmann D, Goslich R. Mechanistic studies of water detoxification in illuminated $TiO_2$ suspensions. *Solar Energy Materials*, 1991, 24, 564-583.

8. Fujihira M, Satoh Y, Osa T. Heterogeneous photocatalytic oxidation of aromatic compounds on $TiO_2$. *Nature*, 1981, 293, 206.

9. Shimizu K, Kon K, Onodera W, Yamzaki Hiroshi, Kondo Junko N. Heterogeneous Ni catalyst for direct synthesis of primary amines from alcohols and ammonia. *ACS Catalysis*, 2012, 3, 112-117.

10. Shimizu K, Kanno S, Kon K, Siddiki S.M.A. Hakim, Tanaka H, Sakata Y. N-alkylation of ammonia and amines with alcohols catalyzed by Ni-loaded $CaSiO_3$. *Catalysis Today*, 2014, 232, 134-138.

11. Kataoka S, Gurau M C, Albertorio F, Holden M.A., Lim S.M., Yang R.D., Cremer P.S., Investigation of water structure at the $TiO_2$/aqueous interface. *Langmuir*, 2004, 20, 1662-1666.

12. Zhang Z, Fenter P, Cheng L, Cheng L, Sturchio N.C, Bedzyk M.J, Predota M, Bandura A, Kubicki J.D., Lvov S.N., Cummings P.T., Chialvo A.A. Ridley M.K., Benezeth P, Anovitz L, Palmer D.A., Machesky M.L., Wesolowski D.J. Ion adsorption at the rutile− water interface: Linking molecular and macroscopic properties. *Langmuir*, 2004, 20, 4954-4969.

13. Martin-Jimenez D, Chacon E, Tarazona P, Garcia R. Atomically Resolved Three-Dimensional Structures of Electrolyte Aqueous Solutions near a Solid Surface. *Nat. Commun.* 2016, 7,12164.

14. Sasahara A, Murakami T, Tomitori M. Nanoscale characterisation of $TiO_2$ (110) annealed in air. *Applied Surface Science*, 2018, 428, 1000-1005.

15. Horcas I, Fernández R, Gomez-Rodriguez J M, Colchero J, Gomez-Herrero J, Baro A.M. WSXM: a software for scanning probe microscopy and a tool for nanotechnology. *Review of Scientific Instruments*, 2007, 78, 013705.

16. Uetsuka H, Sasahara A, Onishi H. Topography of the rutile $TiO_2$ (110) surface exposed to water and organic solvents. *Langmuir*, 2004, 20, 4782-4783.

17. Sader J E, Jarvis S P. Accurate formulas for interaction force and energy in frequency modulation force spectroscopy. *Applied Physics Letters*, 2004, 84, 1801-1803.

18. 日本化学会. 基礎編. 化学便覧 改訂 4 版, 1993, 2.

19. Serrano G, Bonanni B, Di Giovannantonio M, Kosmala T, Schmid M, Diebold U, Carlo A.D., Cheng J., VandeVondele J., Wandelt K., Goletti C. Molecular ordering at the interface between liquid water and rutile $TiO_2$ (110). *Advanced Materials Interfaces*, 2015, 2, 1500246.

20. Schlegel S J, Hosseinpour S, Gebhard M, Devi A, Bonn M, Backus E H.G. How water flips at charged titanium dioxide: an SFG-study on the water–$TiO_2$ interface. *Physical Chemistry Chemical Physics*, 2019, 21, 8956-8964.

21. White J M, Henderson M A. Trimethyl acetate on $TiO_2$(110): preparation and anaerobic photolysis. *The Journal of Physical Chemistry B*, 2005, 109, 12417-12430.

22. Bates S P, Gillan M J, Kresse G. Adsorption of methanol on $TiO_2$(110): A first-principles investigation. *The Journal of Physical Chemistry B*, 1998, 102, 2017-2026.

23. Pasarín I S, Yang M, Bovet N, Glyvradal M, Nielsen M M, Bohr J, Feidenhans'l R, Stipp S.L.s. Molecular ordering of ethanol at the calcite surface. *Langmuir*, 2012, 28, 2545-2550.

24. Imada H, Kimura K, Onishi H. Water and 2-propanol structured on calcite (104) probed by frequency-modulation atomic force microscopy. *Langmuir*, 2013, 29, 10744-10751.

25. Wang L, Song Y, Zhang B, Wang E. Adsorption behaviors of methanol, ethanol, n-butanol, n-hexanol and n-octanol on mica surface studied by atomic force microscopy. *Thin Solid Films*, 2004, 458, 197-202.

26. Nakada T, Miyashita S, Sazaki G, Komatsu H, Chernov A A. Atomic force microscopic study of subsurface ordering and structural transforms in n-alcohol on mica and graphite. *Japanese Journal of Applied Physics*, 1996, 35, L52.

27. Kanda Y, Nakamura T, Higashitani K. AFM studies of interaction forces between surfaces in alcohol–water solutions. *Colloids and Surfaces A: Physicochemical and Engineering Aspects*, 1998, 139, 55-62.

# 4.6 SUPPORTING INFORMATION

(a)

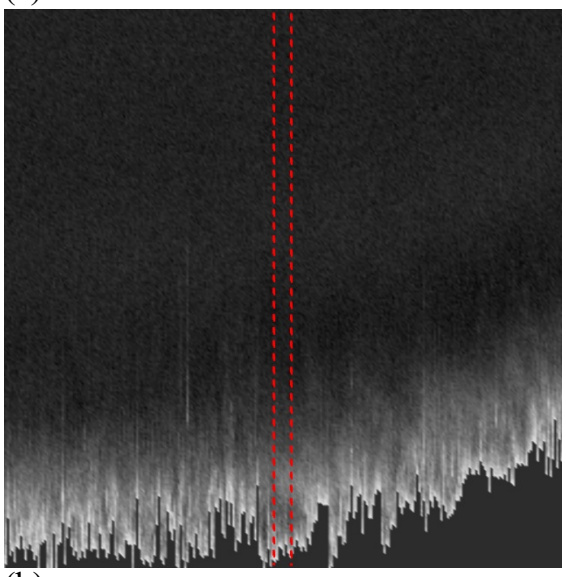

(b)

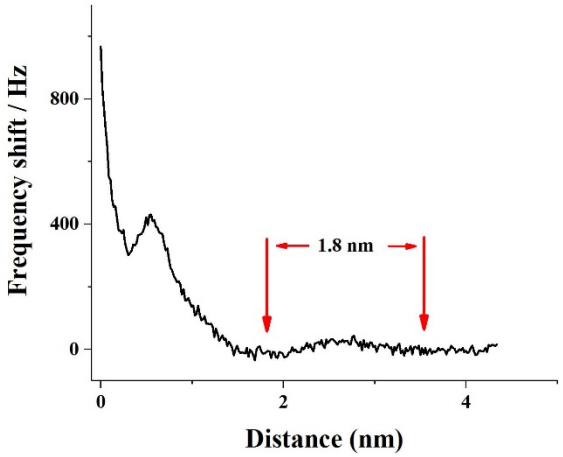


(c)

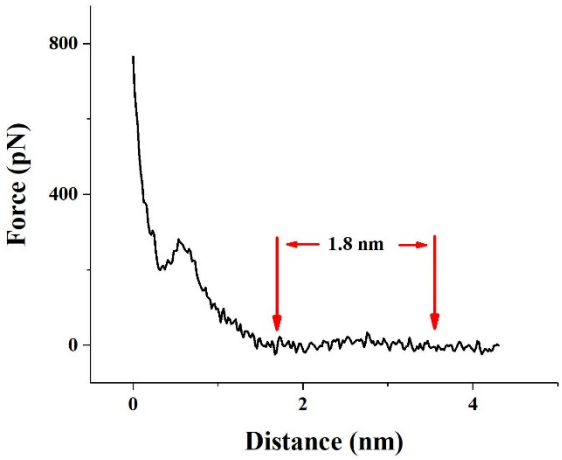


Fig. S1. (a) FM-AFM $\Delta f$ distribution observed above the $TiO_2$ (110) surface in 1-hexanol solution parallel to the $[1\bar{1}0]$ direction . (b) A five lines average $\Delta f$ -distance curve of marked line in Fig(a). (c) A force-distance curve calculated from $\Delta f$ -distance curve.

(a)

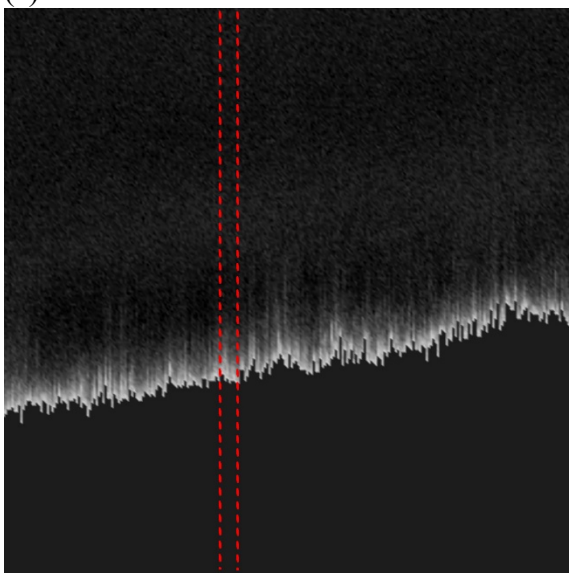

(b)

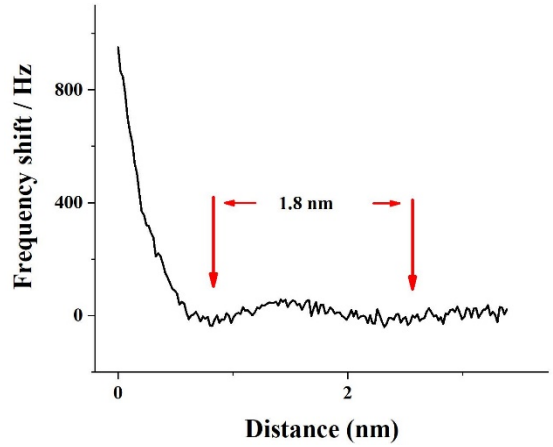


(c)

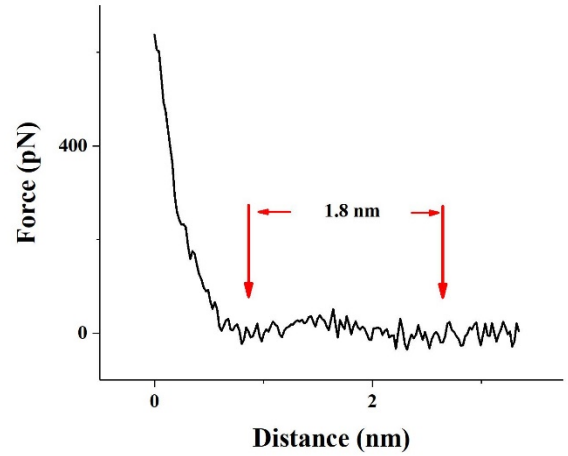


Fig. S2. (a) FM-AFM $\Delta f$ distribution observed above the $TiO_2$ (110) surface in 1-hexanol solution parallel to the $[1\bar{1}0]$ direction . (b) A five lines average $\Delta f$ -distance curve of marked line in Fig(a). (c) A force-distance curve calculated from $\Delta f$ -distance curve.

# Chapter 5

# Ru complexs on $TiO_2$(110) surface probed in water by FM-AFM

# 5.1 INTRODUCTION

Ru complexs are new photocatalysts for $CO_2$ reduction. These complexs can convert stable $CO_2$ molecules into energy-rich substances at normal pressure and temperature by using light energy [1]. Therefore, Ru complexs may be a solution to solve the greenhouse effect and are receiving attention worldwide. However, the Ru complexes photocatalyst's quantum efficiencies are not enough for industrialization.

Previously, Sekizawa et al. [2] demonstrated that the combined use of Ru and Re complexs exerts high performance for the photocatalytic reduction of $CO_2$. Wada et al. [3] combined $TiO_2$ nanoparticles with RuRe complexs to boost $CO_2$ reduction effect, in which the $TiO_2$ nanoparticles can increase the absolute amount of RuRe complexs without decrease the specific surface area of carbon nitride nanosheets. The $TiO_2$ nanoparticles also acted as a stronger adsorption site for RuRe photocatalyst by increase the mobile electrons.

The combination of RuRe complexs and $TiO_2$ could affect the photocatalyst performance. However, we still do not know how RuRe complexs are combined with $TiO_2$ surface. This chapter mainly depicts how RuRe complexs are combined with $TiO_2$ surface, and whether RuRe complexs change in working environment.

RuRe complexs are combined with $TiO_2$ surface through the phosphate group on Ru complexs. The present study used Ru complexs instead of RuRe complexs as a simple model. In the present study, a $TiO_2$(110) surface combined with the Ru complexs was examined in 0.1 M KCl aqueous solution using frequency modulation atomic force microscopy (FM-AFM) technique. Ru complexs can be distinguished from AFM image by comparing the images of $TiO_2$(110) surface with $TiO_2$(110) surface combined with Ru complexs. In particular, it was found that Ru complexs are uniformly distributed on the $TiO_2$(110) surface without agglomeration in aqueous solution.

## 5.2 EXPERIMENT

### 5.2.1 preparation

Ru complexs are prepared by following the protocols of ref [4] from Prof Ishitani's group.

Mirror-polished, (110)-oriented wafers of rutile $TiO_2$ (Shinkosha, STEP type) were annealed in a two-step procedure using a tube furnace, in accordance with earlier report [5]. Isolating the wafer from $SiO_2$-containing devices heated at 1000 ℃ or higher temperatures was essential to avoid silicon contamination on the annealed surface, which was recognized in XPS. The wafers were first maintained at 1000 ℃ for 12 hours in a sapphire tube open to laboratory air. Annealing at the elevated temperature was efficient for developing wide (110) terraces. In the second step, the wafers were further annealed at 500 ℃ in a quartz tube filled with dry air, a mixture of $O_2$ and $N_2$ with a pressure ratio of 1:4. The absence of water vapor in the annealing environment was the key to finish a well-ordered $TiO_2$(110) truncation [5].

Processed $TiO_2$ crystal was putted in acetonitrile dissolved by Ru complexs ($3\times10^{-8}$ M) for 300s. Ru complexs are then combined with $TiO_2$(110) surface.

### 5.2.2 Characterization

Frequency-modulation detection of force on the probing tip was performed with a SPM-8100FM microscope in development (Shimadzu). For topographic imaging of the wafer, resonance oscillation of a silicon cantilever (Nanoworld, PPP-NCHAuD) was mechanically excited with a piezo-actuator. The nominal spring constant of the cantilevers was 40 N $m^{-1}$. The resonance frequency in the imaging solutions was 130–150 kHz with the quality factor of resonance ($Q$) around 10. A typical spectrum of thermally excited cantilever oscillation is shown in Figure 2. The oscillation amplitude was regulated at a preset amplitude ($A$), peak-to-peak amplitude typically of 1 nm. When a conservative force was loaded on the tip, the resonance frequency of cantilever oscillation ($f$) shifted accordingly. The topography of the wafer was traced with regulation of the tip–surface distance by keeping the frequency shift ($f$) at a prefixed setpoint. Observed images were analyzed with WSxM software.

## 5.3 RESULTS AND DISCUSSION

A model of the $TiO_2$(110)-(1×1) surface is shown in Figure 1(a). Along the [001] direction, two 6-fold Ti atoms are bond to the topmost O. The 5-fold Ti atoms are exposed between bridge O atom rows. The Ru complexs are bound to the 5-fold Ti atoms as shown in Figure 1(b). The Ru complexs have $H_2PO_3$ groups, the groups can combine with the 5-fold Ti to make Ru complexs bound to $TiO_2$(110) surface.

There is currently no research on the size of the Ru complexs size, since it is difficult to determinate the size by precise method such as X-ray. The size of the Ru complexs was estimated by the size of the atom and the length of chemical bond. Ru atom's ionic radius is 63 pm [6]. Ru-N bond distance is 178 pm. C-N bond distance is 148 pm. C-H bound distance is about 107-111 pm. C-C bound distance is about 154 pm. P-O bond distance is 164 pm. C-P bond distance is 184 pm [7]. The Ru complex molecular size can be roughly calculated based on the above data. The vertical height as shown in Figure.1(b) is about 1-2 nm, and the vertical length is about 1.5-2 nm.

(a)

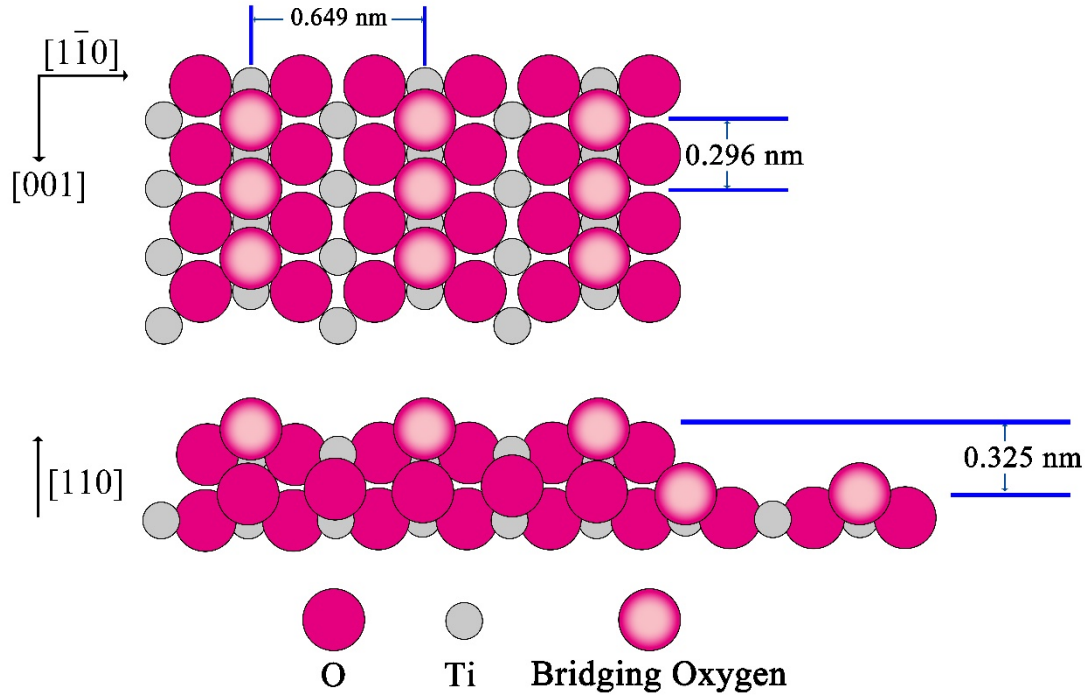


(b)

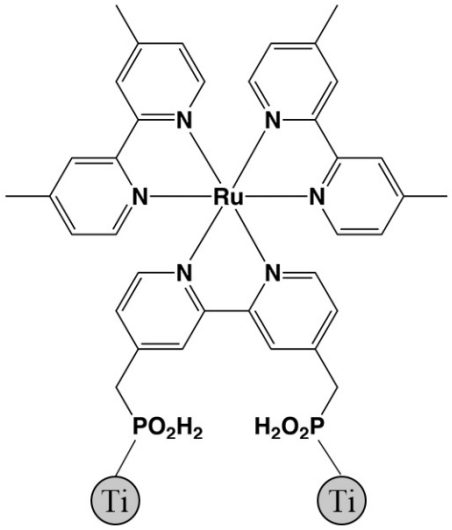


Fig. 1. (a) A model of the $TiO_2$(110) – (1×1) surface. (b) a model of Ru complex bond on $TiO_2$ surface.

The $TiO_2$(110) surface showed (1×1) period after the two-step annealing process in air and dry air according to the method described in Chapter 2. Figure 2(a) shows the $TiO_2$(110) surface after Ru complexs ($3\times10^{-8}$ M) are dissolved in acetonitrile for 300s, in which the step and terrace structures are maintained. However, some dot like substances can be observed on this surface. Cross sections along the black line (A-B) are shown in Figure 2(c). The monatomic step was 0.36 nm, corresponding to single step height of $TiO_2$(110). On the terrace, the dot like substances are about 1 nm in height.

For comparison, Figure 2(b) shows the surface after putting in pure acetonitrile for 300 s without the Ru complexes. The image is similar to that of the $TiO_2$(110) before putting in acetonitrile. The sharp step and flat terrace structures can be observed on this surface. However, there are also some dot like substances on the terrace. Figure 2(d) shows the cross section along the black line (A-B) in Figure 2(b). Single step can be confirmed by the cross section. On the terrace, some dot like substances are less than 0.5 nm in height. When comparing the surface with and without Ru complexs, the two surfaces both have sharp step and flat terrace structures, and both have some dot like substances on the terrace. However, the height of the dot like substances are different depending on the surface, indicating that those dot like substances may be substances of different origin.

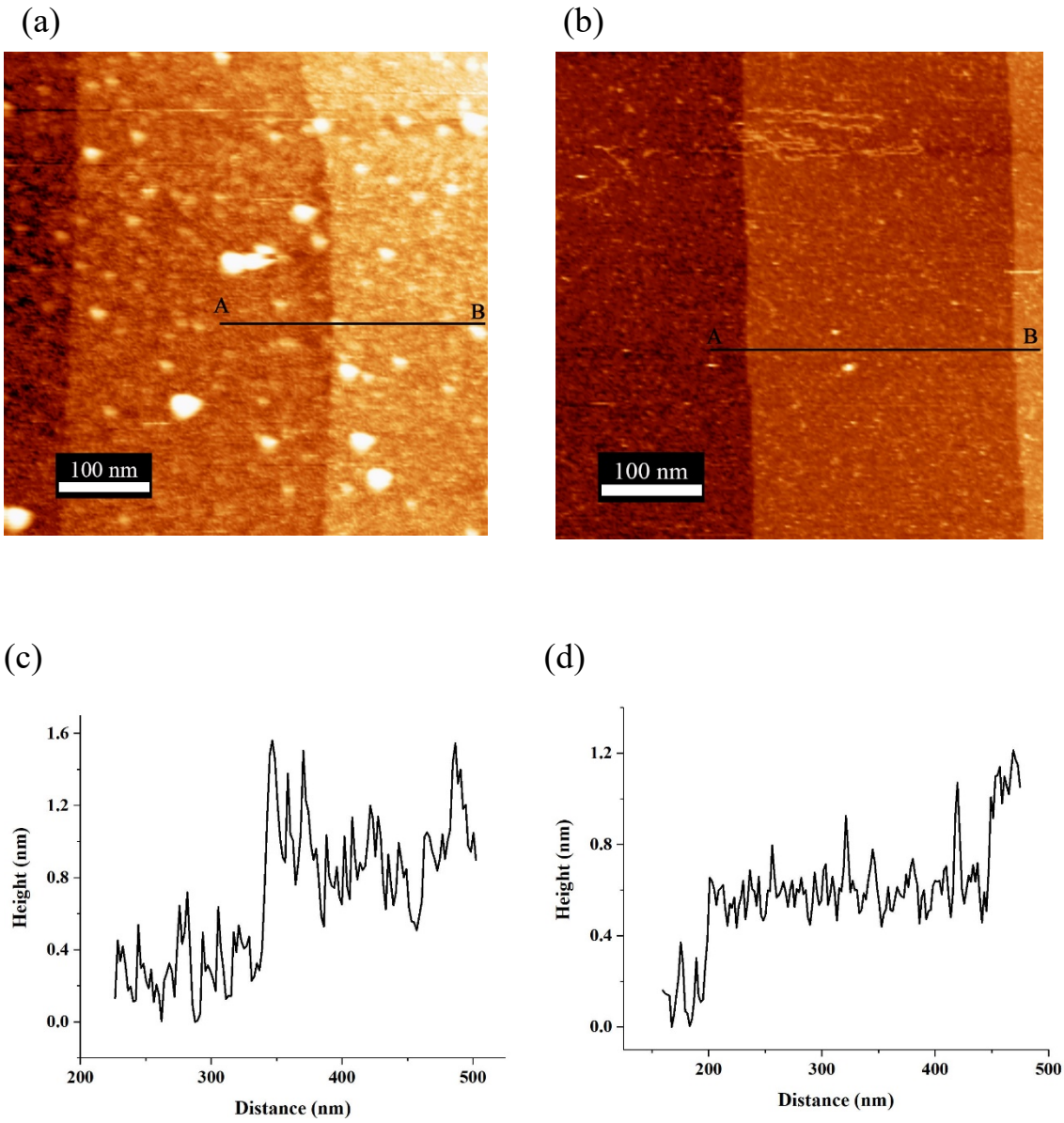


Fig. 2. (a) the AFM image of $TiO_2$(110) bond with Ru complexs. $\Delta f$ = +119 Hz, speed: 451 nm/s, (b) the Cross sections along the black line (A-B) is shown in (a). (c) the AFM image of $TiO_2$(110) after putting in acetonitrile. $\Delta f$ = +83 Hz, speed: 451 nm/s, (b) the Cross sections along the black line (A-B) is shown in (b).

In order to distinguish the substances in the different surfaces, the height and diameter of the dots are counted in two AFM images. The results of surface with Ru complexs are shown in Figures 3(a) and (b), and the results of surface without Ru complexs are shown in Figures 3(c) and (d). On the surface with Ru complexs, two types of dot like substances are observed, and the substances have heights of almost 0.6~1.2 nm and diameter of almost 3~18 nm. On the surface without Ru complexes, only one type of substances can be observed, and the substances are about 0.4 nm in height and 6 nm in diameter. Since this type of substances can also be observed on the surface with Ru complexs, it is possible that the substances are acetonitrile impurities. In this regard, it can be speculated that one of the dot like substances observed in Figures 3(a) and (b) is the acetonitrile impurities and another is the Ru complexs. Therefore, the Ru complexs are about 1 nm in height and 10 nm in diameter in $TiO_2$(110) surface.

As explained previously, the Ru complex's size has been speculated to be 1-2 nm in height and 1.5-2 nm in diameter. Although the height observed for the substances corresponds to the estimated height of Ru complexs, the diameter observed for the substances is much larger than the estimated diameter of the Ru complexs. One possible explanation may be the convolution of the AFM tip apex. Since the tip is much larger than the Ru complexs, it may have caused the Ru complexs to have a larger size when observed in topography. Similar to the present study, Honda et al. also observed a larger size of 5,10,15,20-tetraphenyl-21H,23H-porphyrin cobalt(CoTPP) on mica [8]. CoTPP lying flat on the surface have a length of ca.2 nm, while CoTPP was observed as 10 nm in length in topography.

(a)

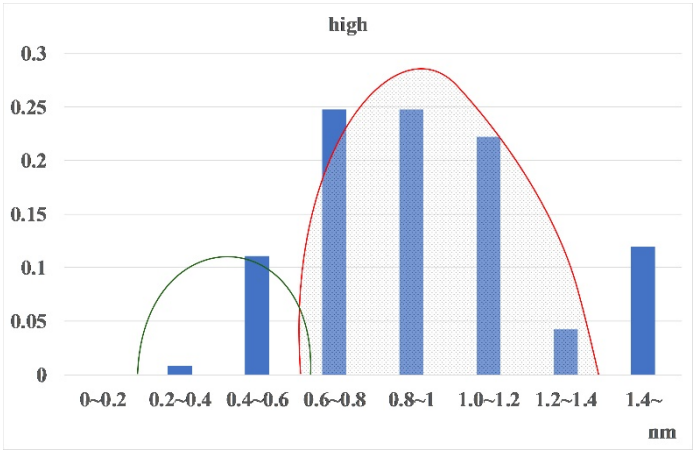


(b)

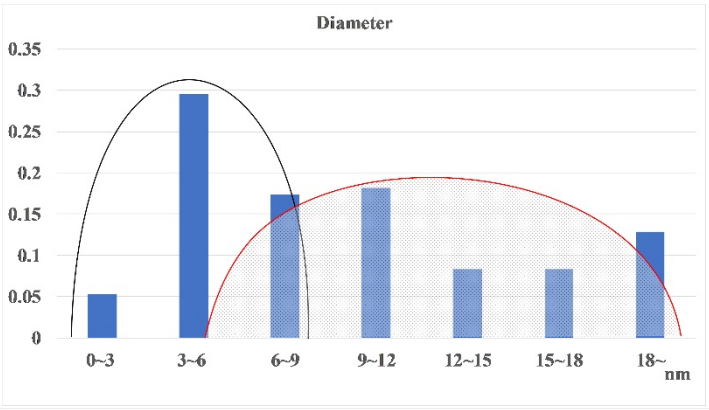


(c)

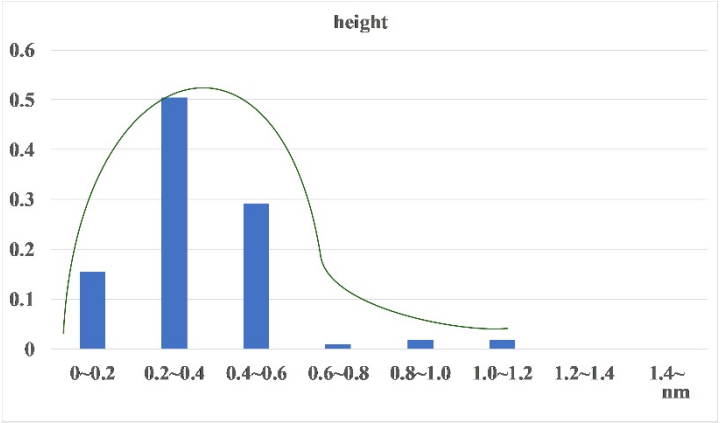


(d)

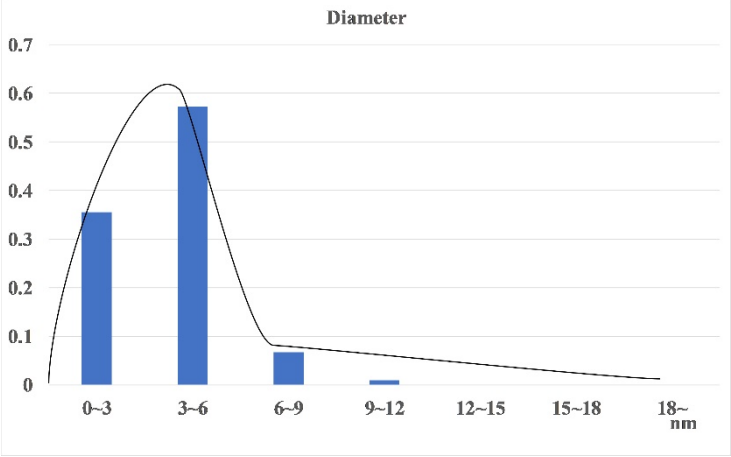


Fig. 3. (a) a height histogram of 100 protrusions in Fig. 2(a). (b) a diameter histogram of 100 protrusions in Fig. 2(a). (c) a height histogram of 100 protrusions in Fig. 2(b).

(d) a diameter histogram of 100 protrusions in Fig. 2(b).

As shown in Figure 2(a), the Ru complexs are distributed on the $TiO_2$(110) surface, and no aggregation of Ru complexes is observed on this surface. Past research has demonstrated that different molecules are adsorbed on the $TiO_2$ (110) surface under different situations. Some molecules were preferentially located at step edges, such as Cu coverages [9] and Ru(4,4'-dicarboxy-2,2'-bipyridine)$_2$(NCS)$_2$ [10]. Cocks et al. demonstrated that acetic acid was adsorbed on the $TiO_2$(110) surface with two O atoms bonded to the 5-fold Ti atoms. This surface showed a (2×1) overlayer which was confirmed by LEED and STM [11]. A dilute formate ion overlayer was observed on the $TiO_2$(110) surface by STM [12]. The formate ions showed a (4×2) order at 22% of the saturation coverage. That is the structure where electrostatic repulsion between formate ions is minimized. When coverage of formate ion increased, the (4×2) order did not develop on the surface, possibly due to the formation of formate-hydroxyl-formate chains on the surface. Schnadt et al. [13] demonstrated that isnicotinic acid was adsorbed on the $TiO_2$(110) surface as one layer, and STM images of isnicotinic acid on the $TiO_2$(110) surface showed stabilized dimer formation structure. The isnicotinic acid molecules are dimerized via ring interactions.

The Ru complexs are bonded with $TiO_2$(110) by 5-fold Ti atoms, which is consistent with the findings of past research. However, Ru complexs are bonded on the $TiO_2$(110) surface in a different mode as Cu [9], which is preferentially bond to step edges; as $Cl_2$ molecules[14], which has paired situation; and as acetic acid, which shows (2×1) overlayer. The Ru complexs are distributed relatively randomly on the $TiO_2$(110) surface with no aggregation on the surface. One possible reason is that the outermost functional groups of Ru complexs are methyl groups, which are very stable and difficult to react with other substances. This may leads to the scattered distribution of Ru complexs on $TiO_2$.

## 5.4 CONCLUSION

The author putted the $TiO_2$(110) air-annealed crystal into the Ru complexs acetonitrile solution for 300s, and Ru complexs bonded on 5-fold Ti atoms.

Upon comparison between the surface putted in Ru complexs solution and the surface putted in solution without Ru complexs, it was discovered that a same substance can be observed in both surfaces, and therefore the substances are speculated to be impurities of acetonitrile. Such comparison can distinguish Ru complexs on $TiO_2$ surface, which are 1 nm in height and 10 nm in diameter. The observed diameter is larger than the presumed value possibly due to tip convolution.

Ru complexs are not aggregated on the $TiO_2$(110) surface, but are rather randomly distributed on the surface.

This chapter is the first to observe Ru complexs in solution, which provided basic information for Ru complexs research.

## 5.5 REFERENCE


1. Kuriki R, Matsunaga H, Nakashima T, Wada K, Yamakata A, Ishitani O, Maeda K. Nature-inspired, highly durable $CO_2$ reduction system consisting of a binuclear ruthenium (II) complex and an organic semiconductor using visible light. *Journal of the American Chemical Society*, 2016, 138, 5159-5170.

2. Sekizawa K, Maeda K, Domen K, Koike K, Ishitani O. Artificial Z-scheme constructed with a supramolecular metal complex and semiconductor for the photocatalytic reduction of $CO_2$. *Journal of the American Chemical Society,* 2013, 135, 4596-4599.

3. Wada K, Ranasinghe C S K, Kuriki R, Yamakata A, Ishitani O, Maeda K. Interfacial manipulation by rutile $TiO_2$ nanoparticles to boost CO2 reduction into CO on a metal-complex/semiconductor hybrid photocatalyst. *ACS applied materials & Interfaces*, 2017, 9, 23869-23877.

4. Ueda Y, Takeda H, Yui T, Koike K, Goto Y, Inagaki S, Ishitani O. A Visible-Light Harvesting System for CO2 Reduction Using a RuII–ReI Photocatalyst Adsorbed in Mesoporous Organosilica. *ChemSusChem,* 2015, 8, 439-442.

5. Sasahara A, Murakami T, Tomitori M. Nanoscale characterisation of $TiO_2$ (110) annealed in air. *Applied Surface Science*, 2018, 428: 1000-1005.

6. Slater J C. Atomic radii in crystals. *The Journal of Chemical Physics*, 1964, 41, 3199-3204.

7. Lide, David R., ed. *CRC handbook of chemistry and physics*. Vol. 85. CRC press, 2004.

8. Honda H, Sasahara A, Onishi H. Porphyrins on mica: Atomic force microscopy imaging in organic solvents. *Colloids and Surfaces A: Physicochemical and Engineering Aspects*, 2019, 561, 194-200.

9. Chen D A, Bartelt M C, Hwang R Q, McCarty K.F. Self-limiting growth of copper

islands on $TiO_2$ (110) -(1× 1). *Surface science*, 2000, 450, 78-97.

10. Sasahara A, Pang C L, Onishi H. STM observation of a ruthenium dye adsorbed on a $TiO_2$ (110) surface. *The Journal of Physical Chemistry B*, 2006, 110, 4751-4755.

11. Cocks I D, Guo Q, Williams E M. ESDIAD studies of the structure of $TiO_2$ (110) (1× 1) and (1× 2) surfaces and interfaces in conjunction with LEED and STM. *Surface Science*, 1997, 390, 119-125.

12. Onishi H, Fukui K, Iwasawa Y. Space-correlation analysis of formate ions adsorbed on $TiO_2$(110). *Japanese Journal of Applied Physics*, 1999, 38, 3830.

13. Schnadt J, Schiessling J, O'shea J N, Gray S M, Patthey L, Johansson M.K-J, Shi M, Krempasky J, Ahlund J, Karlsson P G, person P, Martensson N, Bruhwiler P.A. Structural study of adsorption of isonicotinic acid and related molecules on rutile $TiO_2$(110) I: XAS and STM. *Surface Science*, 2003, 540, 39-54.

14. Diebold U, Hebenstreit W, Leonardelli G, Schmid M, Varga P. High Transient Mobility of Chlorine on $TiO_2$ (110): Evidence for``Cannon-Ball"Trajectories of Hot Adsorbates. *Physical Review Letters*, 1998, 81, 405.

# Chapter 6

# General conclusion

In Chapter 1, the background and purpose of the study were introduced.

In Chapter 2, the water-$TiO_2$ interface was observed by frequency modulation atomic force microscope (FM-AFM).

(1) Through two step annealing method, a cleaned wafer can be observed in aqueous solution. In an addition, coverglass cleaned by UV irradiation and a droplet of imaging liquid was placed on the wafer, not to be in contact with the disk. Two methods can keep no pollution in the liquid.

(2) On the $TiO_2$(110) surface the step and terrace structure can be observed at pH 3, 6 and 11. At pH 3 and 6, bridging oxygen can be first observed as the (1×1) pattern on the terrace. At pH 11, the $OH^-$ combined with five-fold coordinated Ti atoms showed the (2×1) pattern on the surface.

(3) The hydration structures were observed on the $TiO_2$(110) surface at pH 3,6 and 11. Only at pH 6, the hydration structure can be observed clearly since there are different electric charges at different pH values.

In Chapter 3. Nb doped $TiO_2$(110) wafer was observed in air and liquid after annealing.

(1) A gap structure appeared on the Nb doped $TiO_2$(110) after annealing. This structure increased with the amount of doping increases as the number of annealing increases.

(2) The atomic topography and hydration structure of the Nb doped $TiO_2$(110) surface observed in liquid showed images similar to non-doped surface. the location of Nb atoms on the $TiO_2$(110) surface is not identified through these two methods.

In Chapter 4, the $TiO_2$(110) surface was observed in 1-hexanol by FM-AFM.

(1) The $TiO_2$(110) surface showed sharp step and flat terrace in hexanol. The atomic resolution image was not observed on this surface due to the quality factor decreased in 1-hexanol.

(2) On the $TiO_2$(110) surface, one layer of 1-hexanol can be observed. Two molecular layers are arranged vertically and formed as one layer on the $TiO_2$(110) surface. In

the lower 1-hexanol molecule, hydroxy group coordinated with the five-fold coordinated Ti cations on the $TiO_2$(110) surface. In the upper 1-hexanol molecule, hydroxy group was facing outward to the bulk 1-hexanol. Above the $TiO_2$(110), a bilayer structure which is similar to the phospholipid bilayer can be observed.

In Chapter 5, Ru complexs combined with $TiO_2$(110) surface were observed in aqueous solution by FM-AFM.

(1) Ru complexs are observed on the $TiO_2$(110) as the dot like structure in liquid. Upon comparison between the $TiO_2$(110) surface which is putted in Ru complexs solution and putted in solution without Ru complexs, a same substance which is the impurity of acetonitrile can be observed in both surfaces.

(2) Ru complexs can be distinguish by comparison, which are 1 nm in height and 10 nm in diameter. The observed diameter is larger than the presumed value possibly due to the tip convolution.

In summary, the liquid-$TiO_2$ interface was observed by FM-AFM. With the image of AFM, the relationship between two sides of liquid-$TiO_2$ interface which are hydration structure and surface structure of $TiO_2$ was connected. The present study provided a new idea for solving the problem of liquid-$TiO_2$ interface from an overall aspect.

# ACKNOWLEDGEMENT

I would like to extend my deep gratitude to all those who have offered me a lot of help and support in the process of my thesis writing.

First and foremost, my sincere thanks go to my advisor Professor Onishi for the continuous support of my study. His numerous valuable comments and suggestion with incomparable patience help me in the research a lot. Without his painstaking teaching and insightful advice, the completion of this thesis would have been impossible.

Besides my advisor, I would like to express my sincere gratitude to Professor Sasahara for his insightful comments and knowledge. The profit that I gained from him will be of everlasting significance to my future research.

I would also like to thank Professor Ishitani for his support on providing Ru complexs. Without his help, I would not be possible to accomplish this research.

Special thanks should go to express my wife and parents for supporting me on writing this thesis.

Last but not the least, I am indebted to my parents for supporting me to do whatever I want to. I also need to express my gratitude to all my friends, my lambastes in Onishi group.

# List OF PUBLICATIONS

1. “Atom-Scale Topography of Rutile $TiO_2$(110) in Aqueous Solutions: A Frequency-Modulation Atomic Force Microscope Study”

   Shengkai Xue, Akira Sasahara, Hiroshi Onishi

   *The Journal of Chemical Physics*, **2020**, 152, 054703